3D Harmonic Echocardiography

Marco M. Voormolen

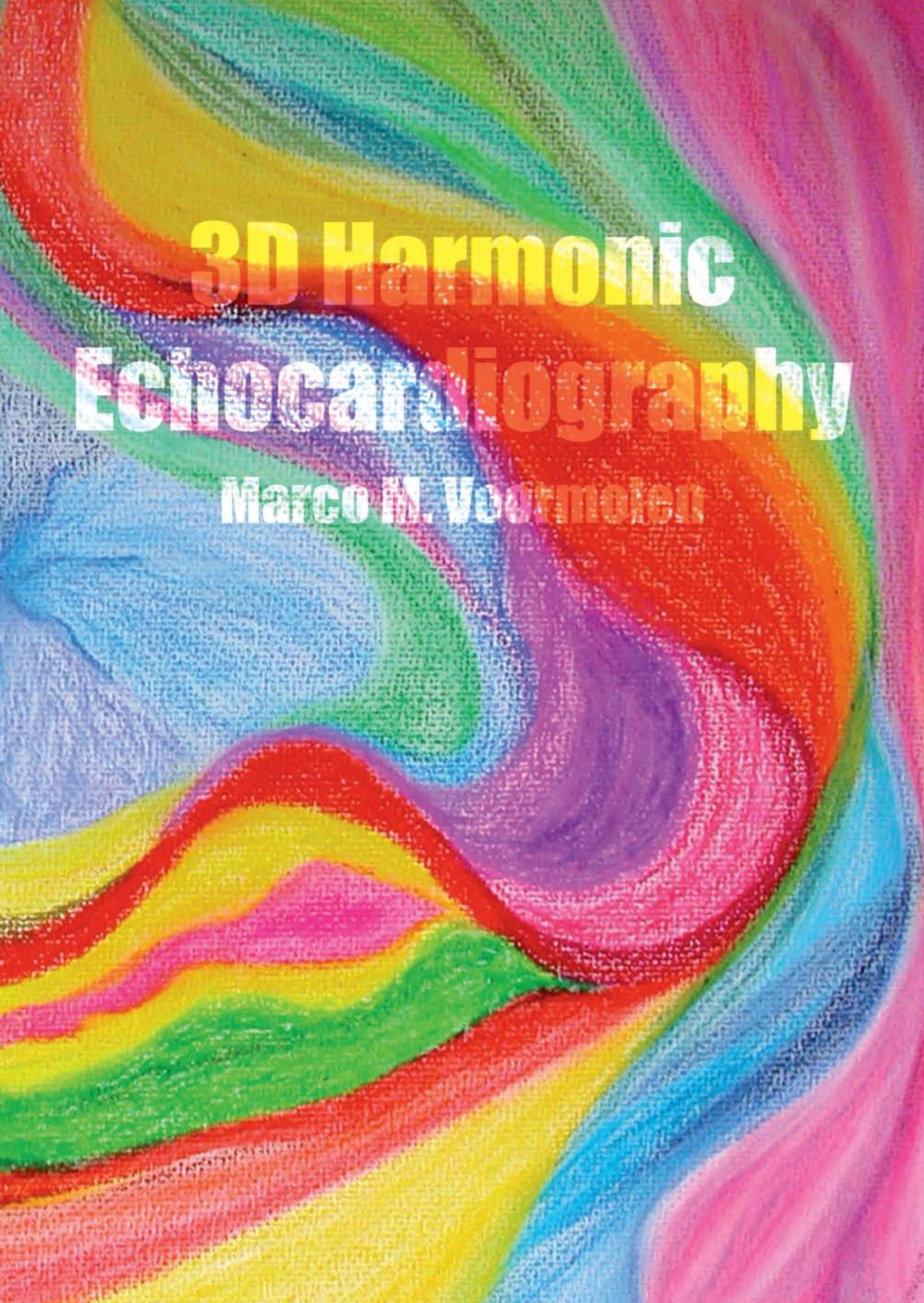

3D Harmonic Echocardiography

Marco M. Voormolen

ISBN 978-90-8559-163-4

Cover illustration 'Colores', by M.A. Gutiérrez González, 2004.

Typesetting in LaTeX 2_ε.

Printed by Optima Grafische Communicatie (Rotterdam, the Netherlands) on 90 g G-print paper.

© 2007 M.M. Voormolen. No part of this publication may be reproduced, stored in a retrieval system, or transmitted in any form or by any means without the prior written consent from the author (marco@voormolen.eu).

Three Dimensional Harmonic Echocardiography

Drie dimensionale harmonische echocardiografie

Proefschrift

ter verkrijging van de graad van doctor
aan de Erasmus Universiteit Rotterdam
op gezag van de rector magnificus

Prof.dr. S.W.J. Lamberts

en volgens besluit van het College voor Promoties.

De openbare verdediging zal plaatsvinden op

woensdag 17 oktober 2007 om 11.45 uur

door

Marco Marien Voormolen

geboren te Utrecht.

Promotiecommissie

Promotoren:	Prof.dr.ir. N. de Jong Prof.dr.ir. A.F.W. van der Steen
Overige leden:	Prof.dr. H. Torp Prof.dr. J.R.T.C. Roelandt Prof.dr.ir. J.H.C. Reiber
Copromotor:	Dr.ir. A. Bouakaz

Financial support for the publication of this dissertation by the following institutes and companies is gratefully acknowledged.

Lecoeur Electronique (Chuelles, France)

TomTec Imaging Systems (Unterschleißheim, Germany)

Interuniversity Cardiology Institute of The Netherlands (Utrecht)

Cardialysis (Rotterdam, The Netherlands)

GE Healthcare (Horten, Norway)

Oldelft Ultrasound (Delft, The Netherlands)

Philips Medical Systems (Böblingen, Germany)

Contents

Detailed Contents

General Introduction

Partly adapted from:

© 2003 Krenning *et al.*. Reprinted, with permission, from: **Krenning, B.J.**, M.M. Voormolen and J.R.T.C. Roelandt. Assessment of Left Ventricular Function by Three-Dimensional Echocardiography. *Cardiovascular Ultrasound*, 1(1):12, 2003.

i.1 From Echo to Harmonic Echocardiography

The principle of echography From an experiment performed in a mountainous environment or well, we all know that the sound of our voice is reflected from a hard surface and returned to us as an echo. The same principle is exploited by echography or ultrasound imaging. Sound or pressure waves are transmitted into a medium and scattered by inhomogeneities or refracted and reflected at the interface of different acoustic media. By detecting these echoes the distance to a reflecting object can be deduced from their arrival times, when the propagation speed of the medium is known.

For echography an ultrasonic pulse is transmitted in a narrow beam resulting in echoes from a tubular region of the insonified medium. The received echoes, the so called *radio frequency* (RF) signal, represents the scatterers density in the region as function of depth. Plotting the RF signals of multiple transmissions as function of time gives us an impression of the dynamics in the region. By assigning a gray scale value to the envelope of the RF signals we obtain a so called *M-mode image*. In the same way a cross-sectional image of the scanned medium is obtained by steering the acoustic beam in different directions. The resulting two-dimensional gray scale image is also known as *B-mode image*.

Echocardiography Among others, like the abdominal organs and the brain, echography is very suitable for diagnostic imaging of the heart. Especially transthoracic echocardiography, which is the subject of this dissertation, has important advantages over alternative non-invasive techniques as *computed tomography* (CT) and *magnetic resonance imaging* (MRI). Echography does not make use of ionizing radiation which allows repetitive monitoring of a patient's progress in contrast with CT. Compared to MRI, echography is very cost effective, it does not exclude patients with magnetic prostheses and it can be performed at bedside (see chapter 7). The image resolution of all three techniques are of the same order. However, echocardiographic images often possess an inhomogeneous echo distribution or even drop-out. This makes the images less intuitive to interpret and can be seen as the biggest drawback of echocardiography. An very important general advantage of diagnostic ultrasound is its harmless nature. No negative biological effect has been reported from, as long as the current guidelines for the use of diagnostic ultrasound are respected [Barnett 2000].

The resolution of an echographic image is mainly determined by the frequency of the transmitted pulse. Increasing the frequency seems therefore

the ideal way to increase the resolution. Higher frequencies however, suffer from an increased attenuation of the ultrasonic wave. The attenuation limits the depth from which echoes can be detected and the imaging frequency is therefore a tradeoff between penetration depth and image resolution. Typical values for adult echocardiography are a transmit frequency of 2–4 MHz and a penetration depth of 10–15 cm.

Harmonic echocardiography An imaging modality that emerged in the late 90's is *tissue harmonic imaging*, or shortly *harmonic imaging* [Ward 1997, Spencer 1998, Tranquart 1999]. In a relatively short time this image modality has become the most frequently used imaging modality for diagnostic ultrasound. Harmonic imaging is based on the nonlinear relation between pressure and density in biological tissue and most other media. This nonlinear relation results in an increased propagation speed for the compressional part of the pressure wave and a decreased propagation speed for rarefactional part. As the sound wave propagates through the medium a progressive distortion is observed. The distortion manifests itself as harmonics of the fundamental (transmitted) signal. Standard harmonic imaging utilizes the second harmonic component in the received RF signals.

The popularity of harmonic imaging is the result of a number of advantages over fundamental imaging [Humphrey 2000, Duck 2002]:

a. *Narrower beam width* - The narrower width of the harmonic beam results in a higher lateral resolution (see chapter 1 and 2).

b. *Reduced side lobes* - Next to the main lobe, side lobes are present, which can give rise to image artifacts or additional clutter. A reduced side lobe level will therefore result in a clearer image (see chapter 1 and 2).

c. *Reduced reverberation* - Multiple reflections from the surface layers of the thorax result in secondary echoes. For fundamental imaging these echoes give rise to additional clutter in the first part of the image. Due to the low amplitude of these secondary echoes no significant harmonic generation is obtained. The secondary echoes are therefore not present in the harmonic B-mode image.

d. *Reduced grating lobes* - Grating lobes are generated by arrays and result in ghost images of structures at a different location than the region of interest. In harmonic imaging, the lower amplitude of these grating lobes will result in suppression of the artifacts (see chapter 2).

e. *Reduced aberration* - Inhomogeneities in the surface layers of the thorax may effect the integrity of the transmitted pressure field and the resulting acoustic beam. At lower frequencies the aberration of the transmitted field is usually smaller. For harmonic imaging, the transmit frequency is two times lower than the imaging frequency, which can be used to reduce aberration.

f. *Increased dynamic range* - The harmonic beam has a faster lateral decay. With sufficient signal-to-noise ratio in the received RF signals this results in a larger dynamic range of the harmonic B-mode image.

The harmonic component of the received RF signal has a lower amplitude than the fundamental component. The technological challenge of harmonic imaging is therefore the construction of transducers with high sensitivity that exhibit a sufficient signal-to-noise ratio. In addition, a large bandwidth is required, which includes the transmit and receive frequency bands.

i.2 Three Dimensional Echocardiography

Although the first clinical three dimensional (3D) echographic recordings were already made in the 50's, it took until the beginning of the twenty-first century before 3D echocardiographic systems were used for the daily clinical practice [Howry 1956]. Various techniques have been proposed for the acquisition of temporal and 3D positional image data: the use of positional locators (*freehand scanning*), stepwise displacement, continuous (uniform and oscillatory) motion and (*real-time*) volumetric imaging. Most of these methods require additional intervention for respiratory gating and off-line post-processing of the recorded data using specific software. This has been the main limitation for routine application in clinical practice. All methods need a stable cardiac rhythm and constant cardiac function during image acquisition.

Freehand scanning (random imaging) Different devices have been developed for locating the ultrasound transducer and the imaging planes through the heart [Gopal 1992, Handschumacher 1993]. These devices allow free movement of the transducer at one acoustic window or at different acoustic windows.

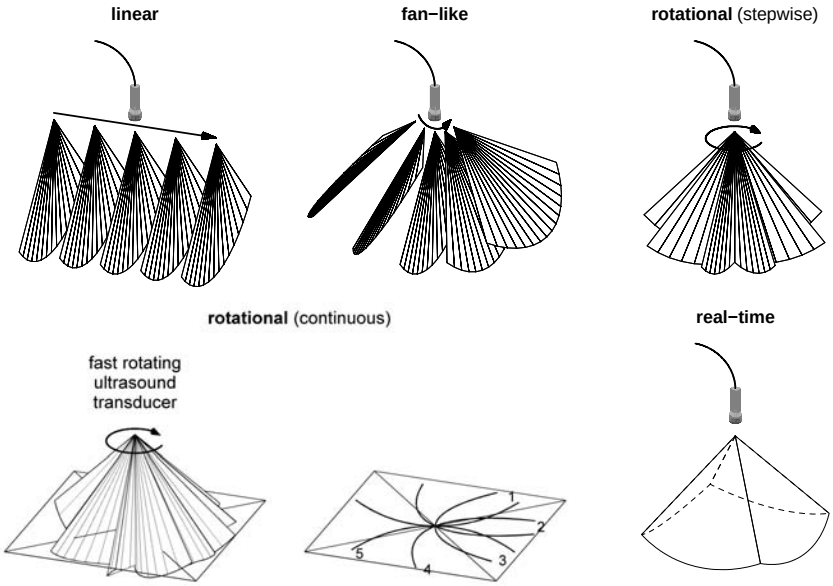

Figure i.1: *Different methods of data acquisition for transthoracic 3D-echocardiography. Continuous rotation results, unlike stepwise rotational scanning, in a curved shape of the original images. Real-time imaging provides a pyramidal dataset.*

Stepwise displacement and continuous motion techniques

a. *Linear acquisition* - Parallel imaging can be performed by computer-controlled movement of the ultrasound transducer in a linear direction (see figure i.1). Both a transthoracic and transoesophageal approach were evaluated for this mode of data acquisition.

b. *Fan-like scanning* - A pyramidal dataset can be obtained by moving the ultrasound transducer in a fan-like arc at prescribed angles (see figure i.1). This is accomplished by computer-controlled motors adapted to the transthoracic or transoesophageal transducer [Delabays 1995].

c. *Stepwise rotational scanning* - With this approach, the transducer is rotated around its central axis, resulting in a conical volume data set (see figure i.1). Different algorithms have been developed for computer controlled sequential image collection of the heart [Pandian 1994].

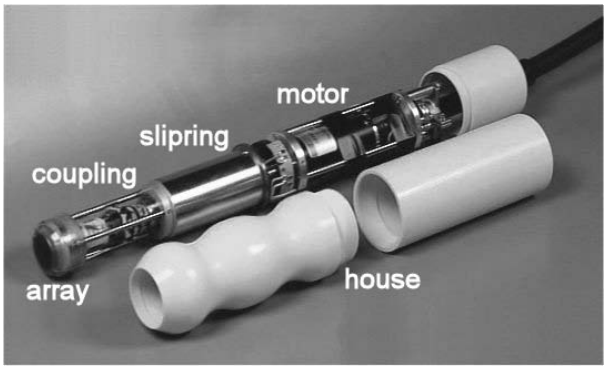

Figure i.2: *Construction of the fast rotating ultrasound transducer, second prototype.*

d. *Continuous rotational scanning* - Various acquisition methods based on continuous rotation with an internally rotating array are reported [Canals 1999, Belohlavek 2001]. Some models require periodic inversion of the rotation because of cable torsion, thereby making the acquisition less efficient and the reconstruction of data sets more complex. A continuous uniform motion approach is presented in this dissertation (see figure i.2). Initial experience indicates that this approach is an alternative to real-time volumetric systems for global volume and regional wall motion analysis of the left ventricle (see chapter 4 and 9).

Real-time imaging The first real-time 3D system has been developed at Duke University (Durham, North Carolina, USA) [Sheikh 1991]. This system makes use of a sparse matrix phased array transducer of 512 elements to scan a 60°×60° pyramidal tissue volume using parallel processing technology. More recently, Philips Medical Systems has introduced its live 3D system using a matrix array transducer with 3000 elements. In this transducer, multiple recordings are automatically performed to cover the full left ventricle in a so called *full volume scan* (see also chapter 3).

In general 3D echocardiography has a great potential for the assessment of LV function in various clinical scenarios including stress echocardiography and during interventional procedures.

i.3 Outline of this Dissertation

The aim of the project described in this dissertation is the development and clinical validation of a new concept for harmonic 3D echocardiography. Following the above introduction the remaining chapters of this dissertation can be divided in three parts:

I. *Harmonic transducer design and implementation* - Chapter 1 describes the development of an simulation tool for steered nonlinear acoustic beams from medical transducers, assisting their design. This simulation tool is then experimentally validated in chapter 2 after which our *fast rotating ultrasound* (FRU) transducer is introduced in chapter 3.

II. *Basic application: Left ventricular volume quantification* - In chapter 4 the suitability of the FRU-transducer for LV volume quantification is tested. An alternative approach to LV volume quantification with the FRU-transducer is validated in chapter 5 and a method to increase the efficiency of LV volume quantification is presented in chapter 6.

III. *Advanced applications* - Advanced applications of harmonic 3D echocardiography are presented in chapter 7 to 9. In an attempt to demonstrate the flexible application of 3D echocardiography, the possibilities of LV volume determination during hemodialysis treatment is investigated in chapter 7. The feasibility of 3D contrast harmonic imaging is explored in chapter 8. Ultimately, regional LV wall motion analysis is used to asses the efficiency of LV pacing in chapter 9.

Part I

Harmonic Transducer Design and Implementation

Chapter 1

Simulation of Steered Harmonic Acoustic Beams from Medical Transducers

Part I: Method and Benchmark

Rotterdam, June 4th, 2004: *Finalizing a Ph.D. project is one thing, the real trouble starts when your colleagues cannot stand the smell of your black currant tea.*

For an efficient development of new medical transducers it is desirable to simulate the propagation of nonlinear acoustic beams from apertures with arbitrary geometry. We developed a two-stage numerical solution to compute steered nonlinear pressure fields from such sources. For this purpose the KZK equation is numerically solved in time domain.

Limited off-axis validity of the parabolic approximation, used to derive the KZK equation, does not allow the simulation of steered beams without additional measures. To overcome this limitation, we propose a method where Field II is used to calculate the pressure distribution close to the transducer's surface, at a plane perpendicular to the direction of interest. The source plane is then propagated with our KZK solution.

To validate our method results are compared with linear and nonlinear algorithms that do not employ the parabolic approximation. The comparison shows the feasibility of simulated steered harmonic beams from phased array transducers using the KZK equation.

Based on:

Voormolen, M.M., N. de Jong and A. Bouakaz. Simulation of steered harmonic acoustic beams from medical transducers - Part I: Method and benchmark. *The Journal of the Acoustical Society of America*, submitted, 2007.

1.1 Introduction

The theory behind the nonlinear characteristics of intense sound beams in a thermoviscous fluid from an acoustic aperture of finite size has been investigated in a considerable number of publications. To this extent an analytical solutions to the lossless parabolic wave equation has been sought by Froysa *et al.* [1996] and Hamilton *et al.* [1997]. Froysa *et al.* developed a solution based on the renormalization of the quasilinear approximation for Gaussian sources, capable of describing the formation of shock waves and their early evolution. Hamilton *et al.* suggested a method based on analytical techniques used in nonlinear geometrical acoustics, leading to an axial solution for periodic signals from Gaussian sources in their pre-shock region.

An alternative analytical approach is quasilinear theory which determines the second harmonic component as a small correction to the linear solution [Lucas 1983, Saito 1987, Berntsen 1984]. Quasilinear theory is valid for cases involving weak nonlinear distortion. It does not describe the generation of higher harmonic components and shock formation.

The lack of analytic solutions of the nonlinear wave equation for transducers and conditions encountered in medical ultrasound has lead to the use of numerical approaches. Most of the numerical solutions are based on the popular Khokhlov-Zabolotskaya-Kuznetsov (KZK) equation [Zabolotskaya 1969, Kuznetsov 1971]. This nonlinear parabolic wave equation is known to describe consistently the propagation of a finite amplitude sound beam by accounting for the combined effects of diffraction, absorption, and nonlinearity. The equation was developed for confined acoustic beams and employs the parabolic approximation. Due to this approximation the validity of the equation close to the transducer's surface and outside the paraxial region of the acoustic beam is limited. A frequency domain implementation, known as the Bergen code, has been implemented for piston, rectangular and phased array transducers with or without focusing and for continuous wave or pulsed excitation [Aanonsen 1984, Hamilton 1985, Baker 1988, 1995, Averkiou 1995, Cahill 1998]. Especially for pulsed excitation a time domain implementation, known as the Texas code, is computationally more efficient [Lee 1995]. This code has been implemented for plane and focused piston transducers and recently for rectangular and phased array transducers [Averkiou 1997, Yang 2005, Bouakaz 2003b].

An alternative, combined frequency-time domain approach was developed by Christopher *et al.* [1991]. This angular spectrum method (ASM) uses a spatial Fourier transform for the calculation of the diffraction and does not make use of the parabolic approximation. The limitations of the parabolic ap-

proximation therefore, do not apply to their diffraction algorithm. The ASM was implemented for piston and linear array transducers with continuous wave or pulsed excitation [Christopher 1991, Zemp 2003]. Very recently the ASM was extended with a multistage approach to allow for the simulation of non-planar sources and steered phased array transducers [Christopher 2006].

The advantages of harmonic imaging for diagnostic ultrasound applications has been well established and investigated [Duck 2002]. As a result harmonic imaging is commonly used in the daily clinical practice [Spencer 1998, Tranquart 1999, Frinking 2000]. A simulation tool for harmonic B-mode images based on a focused piston transducer was developed by Li *et al.* [2000]. Despite its importance, development tools that allow the characterization of steered beams from phased array or matrix transducers are not yet available. In this chapter we present a two-stage numerical method, based on the KZK equation, capable of simulating steered acoustic beams. As our main interest lies in diagnostic ultrasound applications we used a time-domain solution, in contrast with Christopher *et al.* [2006], for the simulation of pulsed acoustic signals. The presented algorithm is an extension of the method used be Lee et al. towards apertures with arbitrary geometry [Lee 1995]. Comparison with non-KZK-equation-based algorithms was made to validate our method.

1.2 Methods

The numerical solution of the KZK equation presented in this chapter is based on the time domain method developed by Lee *et al.* [1995]. Their method considers finite amplitude sound beams in homogeneous, thermoviscous fluids from axisymmetric apertures (i.e. circular transducers). This method is extended for apertures with arbitrary geometry to allow the simulation of acoustic beams from phased array or matrix transducers. Sources can be modeled in two spatial dimensions and time (2D+t). Therefore, our method is indicated with three dimensional (3D-)KZK solution.

The 3D-KZK solution itself does not allow the simulation of steered beams due to the parabolic approximation used to obtain the KZK equation. To simulate steered nonlinear beams an additional initialization stage is used. This stage can provide appropriate source conditions for the 3D-KZK solution in case the transducer can not be modeled 2D+t directly, which is the case for steered beams.

The subsequent subsections deal with the 3D-KZK solution, the two-stage 3D-KZK method and the theoretical benchmark.

1.2.1 3D-KZK

Model Equation

In Cartesian coordinates the integro-differential form of the KZK equation is given by:

$$\frac{\partial p}{\partial z} = \frac{c_0}{2}\int_{-\infty}^{t'}\left(\frac{\partial^2 p}{\partial x^2}+\frac{\partial^2 p}{\partial y^2}\right)dt'' + \frac{\delta}{2c_0^3}\frac{\partial^2 p}{\partial t'^2} + \frac{\beta}{2\rho_0 c_0^3}\frac{\partial p^2}{\partial t'} \tag{1.1}$$

Where p is the sound pressure, z is the range coordinate along which the acoustic field is calculated, c_0 is the small signal ambient sound speed, $t' = t - \frac{z}{c_0}$ is the retarded time, t is the time, x and y are the transverse coordinates, δ is the sound diffusivity of a thermoviscous medium, β the coefficient of nonlinearity and ρ_0 the ambient density of the fluid.

To assist the numerical computation, equation (1.1) is transformed into a dimensionless form. The transformation was also employed by Lee *et al.* [1995] and uses the following variables:

$$P = \frac{p}{p_0}, \quad \chi = \frac{x}{r}, \quad \psi = \frac{y}{r}, \quad \sigma = \frac{z}{d}, \quad \tau = \omega_0 t' \tag{1.2}$$

Here p_0 is the characteristic pressure, d is the characteristic range length, r is the characteristic transverse length and ω_0 is the characteristic angular frequency.

Substitution of equation (1.2) into equation (1.1) yields the following transformed beam equation (TBE):

$$\frac{\partial P}{\partial \sigma} = \frac{1}{4G}\int_{-\infty}^{\tau}\left(\frac{\partial^2 P}{\partial \chi^2}+\frac{\partial^2 P}{\partial \psi^2}\right)d\tau' + A\frac{\partial^2 P}{\partial \tau^2} + NP\frac{\partial P}{\partial \tau} \tag{1.3}$$

From which the dimensionless coefficients are defined as:

$$G = \frac{z_0}{d}, \quad A = \alpha_0 d, \quad N = \frac{d}{\bar{z}} \tag{1.4}$$

Where $z_0 = \frac{\omega_0 r^2}{2c_0}$ is the Rayleigh distance, $\alpha_0 = \frac{\delta\omega_0^2}{2c_0^3}$ is the thermoviscous absorption coefficient and $\bar{z} = \frac{\rho_0 c_0^3}{\beta\omega_0 p_0}$ is the plane wave shock formation distance. The ratio $\frac{N}{A}$, known as the Gol'dberg number, signifies the importance of the nonlinearity relative to the absorption.

Source Condition

The source condition defines the time waveform for the transverse plane at $\sigma = 0$. In general the source condition is expressed in the following form:

$$p = p_0 f(t) g(x, y) \tag{1.5}$$

Where $f(t)$ is the source wave form and $g(x, y)$ the amplitude dependence in the transverse direction.

A typical source condition is a focused rectangular aperture for which case can be written:

$$p = p_0 f\left(t + \frac{x^2}{2c_0 d_x} + \frac{y^2}{2c_0 d_y}\right) g(x, y) \tag{1.6}$$

Where d_x and d_y are the focussing distances in the transmission and elevation direction respectively and $g(x, y)$ is equal to the two dimensional top-hat or rectangular function.

In dimensionless form equation (1.6) becomes:

$$P = f\left(\tau + \frac{G\, d\, \chi^2}{d_x} + \frac{G\, d\, \psi^2}{d_y}\right) g(\chi, \psi) \tag{1.7}$$

And $g(\chi, \psi)$ is defined by:

$$g(\chi, \psi) = \begin{cases} 1, & -1 \le \chi \le 1 \quad \& \quad -1 \le \psi \le 1 \\ 0, & -1 > \chi > 1 \quad \& \quad -1 > \psi > 1 \end{cases} \tag{1.8}$$

The above is just an example of a possible source condition since the method allows an arbitrary pulse excitation.

Boundary Conditions

For the numerical computation both the transverse directions and the time domain need to be bounded. Therefore the following limits and boundary conditions are set:

$$P(\sigma, \tau_{min}, \chi, \psi) = 0, \quad P(\sigma, \tau_{max}, \chi, \psi) = 0 \tag{1.9}$$

$$P(\sigma, \tau, \chi_{min}, \psi) = 0, \quad P(\sigma, \tau, \chi_{max}, \psi) = 0 \tag{1.10}$$

$$P(\sigma, \tau, \chi, \psi_{min}) = 0, \quad P(\sigma, \tau, \chi, \psi_{max}) = 0 \tag{1.11}$$

The zero boundary conditions used can result in reflections when the simulated pressure field encounters them. Therefore the boundaries have to be chosen with care to prevent these reflections to interfere with the signals of interest.

Discretization

Both the transverse directions and the time domain are uniformly discretized. For the discretized pressure the following notation is chosen:

$$P^k_{q,i,j} \equiv P\left(\sigma_k, \tau_{min} + q\Delta\tau, \chi_{min} + i\Delta\chi, \psi_{min} + j\Delta\psi\right) \tag{1.12}$$

To increase the efficiency of the calculation a non-uniform discretization of the dimensionless range coordinate σ is used. A dense sampling is needed in the near field, where the pressure varies fast, and a coarse sampling can be used in the far field, where the pressure varies slowly. This is achieved with the following definition of the step size:

$$\Delta\sigma_k = (1 + \sigma_k)^2 \Delta\sigma_0 \tag{1.13}$$

Where $\Delta\sigma_0$ is the given initial spacing of the dimensionless range coordinate.

As a consequence the discretized dimensionless range coordinate σ_k and its step size $\Delta\sigma_k$ are related in the following way:

$$\sigma_k = \sum_{m=0}^{k-1} \Delta\sigma_m \tag{1.14}$$

σ_0 is given by the source condition and σ_1 is equal to $\Delta\sigma_0$.

Numerical Approach

Equation (1.3) is numerically solved with the use of the operator splitting approach [Ames 1992]. With sufficiently small steps for the range coordinate this approach assumes that the effects of diffraction, absorption and nonlinearity are independent. For each step in the range coordinate the effects are accounted for sequentially.

In general the source conditions are modeled with the use of the Heaviside step function. The resulting discontinuities in the source conditions can lead to numerical instability. Therefore the absorption and diffraction in first part of the near field is calculated with use of the implicit backward finite difference (IBFD) method. This method is more effective in damping possible numerical oscillations but has less accuracy. Beyond the oscillatory range the more accurate alternating direction implicit (ADI) method is used allowing for a larger step size.

As the numerical solutions of the absorption and nonlinearity term are identical to those developed by Lee *et al.* [1995] we will only address the numerical solution of the diffraction term in the subsequent paragraphs. For

a detailed description of the numerical solutions of the absorption and nonlinearity term we refer to the dissertation of Lee [1993].

Implicit backward finite difference method To employ the implicit backward finite difference (IBFD) method the χ and ψ component of the diffraction term from equation (1.3) are separated:

$$\frac{\partial P}{\partial \sigma} = \frac{1}{4G}\int_{-\infty}^{\tau} \frac{\partial^2 P}{\partial \chi^2} d\tau', \quad \frac{\partial P}{\partial \sigma} = \frac{1}{4G}\int_{-\infty}^{\tau} \frac{\partial^2 P}{\partial \psi^2} d\tau' \tag{1.15}$$

The IBFD method solves the diffraction in the x and y direction sequentially. As the solutions of both directions are identical we will only consider the x direction from this point on. The numerically approximations of the derivatives in equation (1.15) for the IBFD method are the following [Carnahan 1969]:

$$\frac{\partial P}{\partial \sigma} \quad \rightarrow \quad \frac{P^{k+1}_{q,i,j} - P^{k}_{q,i,j}}{\Delta \sigma_k} \tag{1.16}$$

$$\frac{\partial^2 P}{\partial \chi^2} \quad \rightarrow \quad \frac{P^{k+1}_{q,i+1,j} - 2P^{k+1}_{q,i,j} + P^{k+1}_{q,i-1,j}}{\Delta \chi^2} \tag{1.17}$$

The integral is approximated with the trapezoidal rule which reads as follows, after replacing the lower limit by τ_{min}:

$$\int_{\tau_{min}}^{\tau} f(\tau')\, d\tau' \rightarrow \Delta\tau \left(\sum_{m=1}^{q-1} f_m + \frac{f_0 + f_q}{2} \right) \tag{1.18}$$

As a result of the boundary conditions f_0 can be eliminated since $P^{k}_{0,i,j}$=0.

By combining equation (1.17) and (1.18) we find for the right hand side of equation (1.15):

$$\frac{1}{4G}\int_{-\infty}^{\tau} \frac{\partial^2 P}{\partial \chi^2} d\tau' \rightarrow \frac{\Delta\tau}{4G\Delta\chi^2} \left(\sum_{m=1}^{q-1} \left(P^{k+1}_{m,i+1,j} - 2P^{k+1}_{m,i,j} + P^{k+1}_{m,i-1,j} \right) + \frac{1}{2}\left(P^{k+1}_{q,i+1,j} - 2P^{k+1}_{q,i,j} + P^{k+1}_{q,i-1,j} \right) \right) \tag{1.19}$$

Substitution of equation (1.16) and (1.19) into equation (1.15) yields the desired finite difference equation:

$$-\frac{1}{8}P^{k+1}_{q,i+1,j} + \left(\frac{1}{R} + \frac{1}{4}\right) P^{k+1}_{q,i,j} - \frac{1}{8}P^{k+1}_{q,i-1,j} = \frac{1}{4}\sum_{m=1}^{q-1} \left(P^{k+1}_{m,i+1,j} - 2P^{k+1}_{m,i,j} + P^{k+1}_{m,i-1,j} \right) + \frac{1}{R}P^{k}_{q,i,j} \tag{1.20}$$

Where R is given by:

$$R = \frac{\Delta\tau\Delta\sigma_k}{G\Delta\chi^2} \tag{1.21}$$

For the x direction coordinate index $1 \leq i \leq i_{max} - 1$ equation (1.20) forms a tridiagonal system with the unknown terms in P on the left hand side and the known terms in P on the right hand side. The system can be solved using the Gaussian elimination method [Carnahan 1969]. For each y direction coordinate index $1 \leq j \leq j_{max} - 1$ and for each time index $1 \leq q \leq q_{max} - 1$ a tridiagonal system of $i_{max} - 1$ equations needs to be solved to calculate the pressure field at the next step in the z direction.

Alternating direction implicit method In contrast with the IBFD method the alternating direction method (ADI) solves the diffraction term of equation (1.3) directly [Carnahan 1969].

$$\frac{\partial P}{\partial \sigma} = \frac{1}{4G}\int_{-\infty}^{\tau}\left(\frac{\partial^2 P}{\partial \chi^2} + \frac{\partial^2 P}{\partial \psi^2}\right)d\tau' \tag{1.22}$$

This is achieved by solving two dimensional Laplacian over two half steps. First the diffraction is determined implicitly in the x direction and explicitly in the y direction which is then alternated for the second half step.

The numerical approximation of the derivatives of the diffraction term of equation (1.3) for the x direction are given by:

$$\frac{\partial P}{\partial \sigma} \rightarrow \frac{P^*_{q,i,j} - P^k_{q,i,j}}{\frac{1}{2}\Delta\sigma_k} \tag{1.23}$$

$$\frac{\partial^2 P}{\partial \chi^2} + \frac{\partial^2 P}{\partial \psi^2} \rightarrow \frac{P^*_{q,i+1,j} - 2P^*_{q,i,j} + P^*_{q,i-1,j}}{\Delta\chi^2} + \frac{P^k_{q,i,j+1} - 2P^k_{q,i,j} + P^k_{q,i,j-1}}{\Delta\psi^2} \tag{1.24}$$

Where P^* is the intermediate pressure value after the first half step. The integral is again approximated by the trapezoid rule.

In analog with the IBFD method, substitution of equation (1.24), (1.18) and (1.23) in equation (1.22) yields the following finite difference equation:

$$
\begin{aligned}
&-\frac{1}{16}P^{*}_{q,i+1,j}+\left(1+\frac{R}{8}\right)P^{*}_{q,i,j}-\frac{1}{16}P^{*}_{q,i-1,j}\\
&\qquad=\frac{R}{8}\sum_{m=1}^{q-1}\left(P^{*}_{m,i+1,j}-2P^{*}_{m,i,j}+P^{*}_{m,i-1,j}+P^{k}_{m,i,j+1}-2P^{k}_{m,i,j}+P^{k}_{m,i,j-1}\right)\\
&\qquad\qquad+\frac{1}{16}P^{k}_{q,i,j+1}+\left(1-\frac{R}{8}\right)P^{k}_{q,i,j}+\frac{1}{16}P^{k}_{q,i,j-1}
\end{aligned}
\tag{1.25}
$$

Where $\Delta\chi$=$\Delta\psi$ and R is given by equation (1.21).

For the x direction coordinate index $1 \leq i \leq i_{max}-1$ equation (1.25) again forms a tridiagonal system which can be solved using the Gaussian elimination method.

The numerical approximation of the derivatives for the y direction are:

$$
\frac{\partial P}{\partial \sigma} \quad\rightarrow\quad \frac{P^{k+1}_{q,i,j}-P^{*}_{q,i,j}}{\frac{1}{2}\Delta\sigma_k} \tag{1.26}
$$

$$
\frac{\partial^2 P}{\partial \chi^2}+\frac{\partial^2 P}{\partial \psi^2} \quad\rightarrow\quad \frac{P^{*}_{q,i+1,j}-2P^{*}_{q,i,j}+P^{*}_{q,i-1,j}}{\Delta\chi^2}+\frac{P^{k+1}_{q,i,j+1}-2P^{k+1}_{q,i,j}+P^{k+1}_{q,i,j-1}}{\Delta\psi^2} \tag{1.27}
$$

Which leads to the finite difference equation:

$$
\begin{aligned}
&-\frac{1}{16}P^{k+1}_{q,i,j+1}+\left(1+\frac{R}{8}\right)P^{k+1}_{q,i,j}-\frac{1}{16}P^{k+1}_{q,i,j-1}\\
&\qquad=\frac{R}{8}\sum_{m=1}^{q-1}\left(P^{*}_{m,i+1,j}-2P^{*}_{m,i,j}+P^{*}_{m,i-1,j}+P^{k+1}_{m,i,j+1}-2P^{k+1}_{m,i,j}+P^{k+1}_{m,i,j-1}\right)\\
&\qquad\qquad+\frac{1}{16}P^{*}_{q,i+1,j}+\left(1-\frac{R}{8}\right)P^{*}_{q,i,j}+\frac{1}{16}P^{*}_{q,i-1,j}
\end{aligned}
\tag{1.28}
$$

Solving the tridiagonal system for the y direction index $1 \leq j \leq j_{max}-1$ yields the pressure at the next step in the z direction for the current time index. This has to be repeated for each time index $1 \leq q \leq q_{max}-1$ to obtain the entire pressure field at the next step in the z direction.

1.2.2 Two-stage 3D-KZK

The method described in the previous subsection does not allow the simulation of steered beams. To use our 3D-KZK solution for steered beams an alterative source plane is defined using a coordinate transformation.

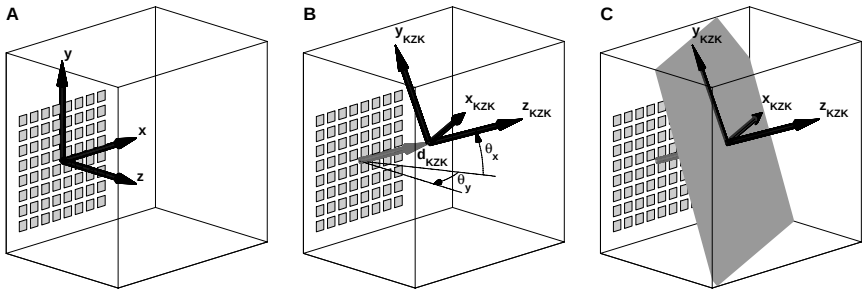

Figure 1.1: *Coordinate systems used for the simulation of steered nonlinear acoustic beams.* ***A.*** *Coordinate system of the transducer.* ***B.*** *Coordinate system of the 3D-KZK solution, d_{KZK} denotes the offset between the two coordinate systems.* ***C.*** *Source plane (grey plane) for the 3D-KZK solution.*

Figure 1.1 shows the coordinate system of the transducer, the coordinate system of the 3D-KZK solution and the source plane. The coordinate transformation between the two systems is defined as follows:

$$\begin{bmatrix} x_{KZK} \\ y_{KZK} \\ z_{KZK} \\ 1 \end{bmatrix} = \begin{bmatrix} \cos\left(\theta_y\right) & 0 & -\sin\left(\theta_y\right) & 0 \\ \sin\left(\theta_x\right)\sin\left(\theta_y\right) & \cos\left(\theta_x\right) & \sin\left(\theta_x\right)\cos\left(\theta_y\right) & 0 \\ \cos\left(\theta_x\right)\sin\left(\theta_y\right) & -\sin\left(\theta_x\right) & \cos\left(\theta_x\right)\cos\left(\theta_y\right) & -d_{KZK} \\ 0 & 0 & 0 & 1 \end{bmatrix} \begin{bmatrix} x \\ y \\ z \\ 1 \end{bmatrix} \tag{1.29}$$

The source field can be calculated using a linear propagation algorithm [Jensen 1992]. Subsequent nonlinear propagation of this source field, using our 3D-KZK solution, results in a two-stage method for simulating nonlinear steered acoustic beams.

Although the offset between the coordinate systems d_{KZK} is generally small, the use of linear acoustic theory over this distance could potentially lead to an under estimation of the harmonic generation. It should also be noted that the orientation of the source plane can be freely chosen using the azimuth θ_y and elevation θ_x angles. This gives the opportunity to explore other parts of the acoustic beam, such as grating lobes, using $\theta_x^{Sim} \neq \theta_x^{Steer}$ and / or $\theta_y^{Sim} \neq \theta_y^{Steer}$.

1.2.3 Theoretical Benchmark

Results from our method are compared with other numerical and analytical solutions. This theoretical benchmark is performed in three steps.

1. The diffraction algorithm is validated using a piston transducer with a 7 mm radius. The result from our solution are compared with those from the axisymmetric code and the analytical solution of equation (1.22) [Lee 1995, Stepanishen 1971]. With the source conditions defined by equation (1.5) the analytical solution reads as follows:

$$\frac{p}{p_0} = f(t') - f\left(t' - \frac{\sqrt{r^2 + z^2} - z}{c_0}\right), \quad x = 0, \quad y = 0 \tag{1.30}$$

2. The combined effect of diffraction and absorption is compared with results from Field II [Jensen 1992]. For this comparison a concave transducer with a radius of 7 mm and a geometric focus of 60 mm is used.

3. The full two-stage 3D-KZK method is compared with the angular spectrum method (ASM) [Zemp 2003]. For this purpose a 64 element phased array transducer with a pitch of 300 μm, a kerf of 50 μm and an elevation and transmission focus of 60 mm is used.

As excitation signal a Gaussian pulse of the following from is used:

$$f(t) = e^{-\left(\frac{\omega_0 t}{\pi n}\right)^{2m}} sin(\omega_0 t) \tag{1.31}$$

Where n is the number of cycles and m the envelope exponent which must be set to 1 for a Gaussian envelope. The medium is set for water at 20 °C: c_0=1482.3 m/s, α=25 mNeper/m/MHz^2 (with $\alpha_0 = \alpha f_0^2$), β=3.48 and ρ_0=998.2 kg/m^3 [Duck 1990].

As mentioned before, the spatial and temporal limits have to be chosen with care to prevent reflections from the boundary to interfere with the pressure signals in the region of interest. For a focusing transducer 3 or 4 times the aperture size is usually enough for a simulation up to a range of about 5 times the aperture size. For the moderate focusing gains (<10) that are considered here, a time window of $7n$ or $8n$ cycles (at the characteristic frequency) suffices. From the time window $4n$ cycles should be used for the trailing edge of the pressure pulse. Depending on the pressure level (i.e. the amount of nonlinearity) 60 to 120 samples per cycle should be used for an accurate estimation up to the third harmonic.

Beam profiles are presented as the envelope amplitude of the time signal, unless otherwise indicated. Harmonic profiles are obtained with an 8$^{\text{th}}$ order Butterworth filter. The first three harmonics are shown (including the fundamental component). To simplify the presentation, the axial profile always originates from the center of the transducer and is aligned with the axis of the acoustic beam.

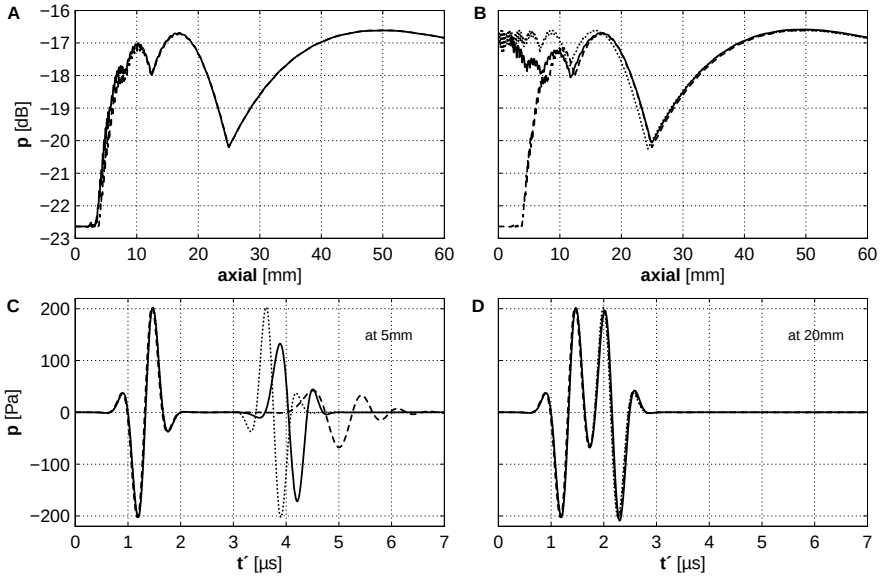

Figure 1.2: *Profiles (spectral amplitude) and time signals from a piston transducer, calculating diffraction only.* ***A.*** *--- axisymmetric solution, — 3D-KZK solution.* ***B–D.*** *⋯ analytical solution, --- axisymmetric solution, — two-stage 3D-KZK method. Simulation settings:* d_{KZK}*=2 mm,* $\Delta\tau$*=0.16,* $\Delta\chi$*=*$\Delta\psi$*=0.020,* $\Delta\sigma_0^{IBFD}$*=0.001,* $\Delta\sigma_0^{ADI}$*=0.002,* f_0*=1.5 MHz and n=1.*

1.3 Results

Figure 1.2 shows the benchmark results of the diffraction algorithm. In panel A the axisymmetric and 3D-KZK solution are compared using a single cycle Gaussian excitation pulse. The differences in the sampling of the transverse plane between both methods result in a minimal deviation very close to the aperture. For distances larger than 8 mm the two methods result in identical on axis values. Panel B shows the results of the analytical solution, the axisymmetric solution and the two-stage 3D-KZK method. Due to the parabolic approximation used for the KZK equation both the arrival time and amplitude of the edge wave is underestimated (see also panel C and D). This is clearly depicted by the axisymmetric profile. The two stage 3D-KZK method seems to do much better in this respect since the source field is provided by Field II, which estimates the edge wave correctly. However, during the first few millimeters the deviation between the analytical solution and the two-

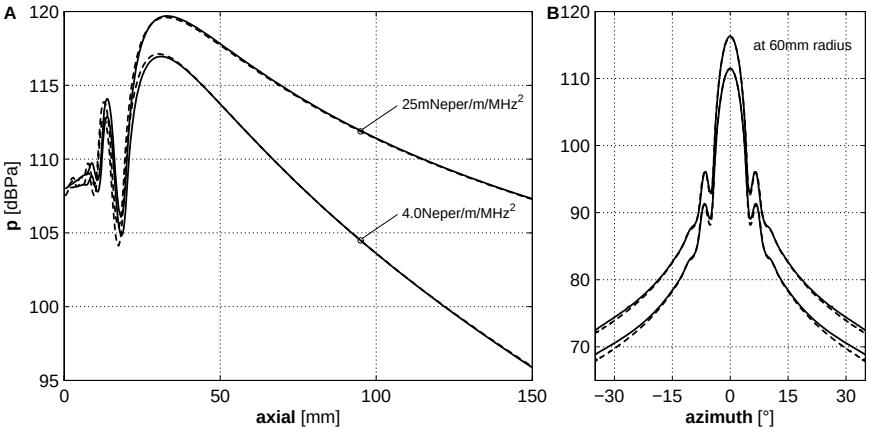

Figure 1.3: *Linear acoustic profiles from a concave transducer. - - - Field II, — two-stage 3D-KZK method. Simulation settings:* d_{KZK}*=2 mm,* $\Delta\tau$*=0.16,* $\Delta\chi$*=*$\Delta\psi$*=0.020,* $\Delta\sigma_0^{IBFD}$*=0.001,* $\Delta\sigma_0^{ADI}$*=0.002,* f_0*=1.5 MHz, n=3 and* α*=0.025 and 4 Neper/m/MHz*^{2}*.*

stage 3D-KZK method is increasing. Both numerical methods give a good agreement at a little bit less than 20 mm (see also panel C and D).

When both absorption and diffraction are taken into account our two-stage 3D-KZK is in agreement with results from Field II as is depicted in figure 1.3. Axial profiles for two attenuation values are shown in figure 1.3: 25 mNeper/m/MHz^2, which is equal to the attenuation value of water at 20 °C, and 4 Neper/m/MHz^2 (not a physical value). The radial profiles give insight in the off-axis validity of the two-stage 3D-KZK method. Identical results are shown up to about 25° off-axis after which a very small overestimation can be seen. An off-axis validity boundary of 25° is beyond what is expected from the parabolic approximation.

Harmonic beam profiles from a non-steered 64 element phased array are shown in figure 1.4. Except for a small underestimation of the harmonic generation in the near field, good agreement is obtained between the two-stage 3D-KZK method and the ASM. The underestimation is a known side effect from the numerical solution of the KZK equation and is partly related to the axial step size [Baker 1995]. However, this has no consequences for the results in the focal region and the far field.

In the transverse profiles of figure 1.4 we see a difference arising between the two methods at about the second side lobe in the second harmonic profile.

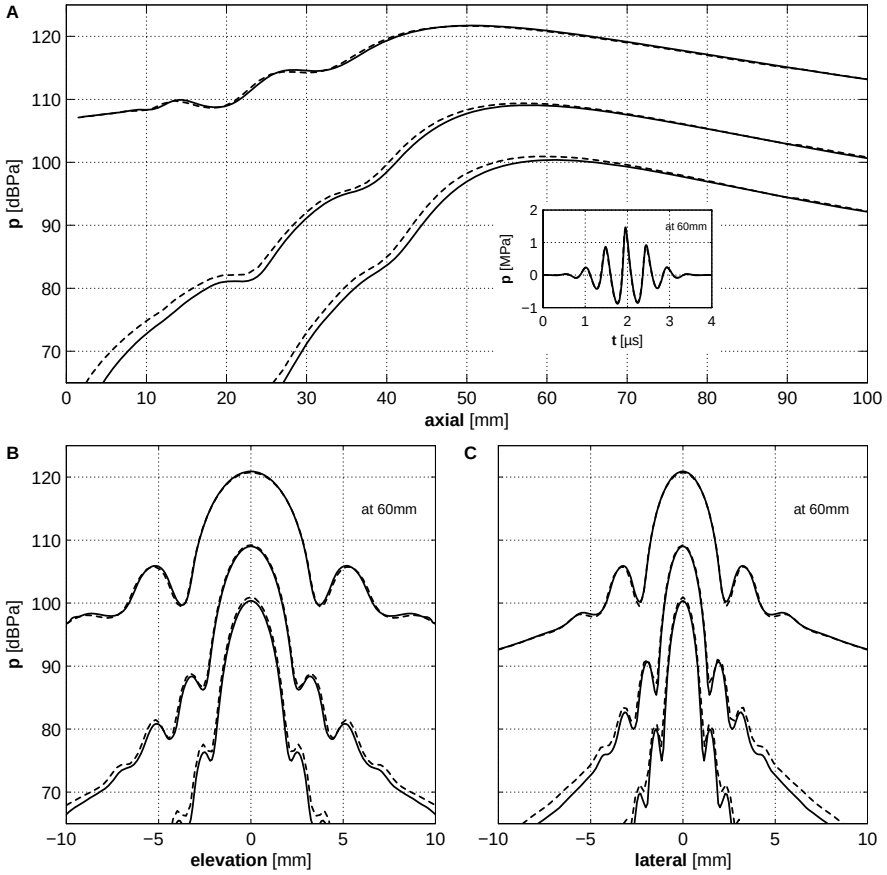

Figure 1.4: *Harmonic profiles from a 64 element phased array transducer. --- angular spectrum method, — two-stage 3D-KZK method. Simulation settings:* d_{KZK}*=2 mm,* $\Delta\tau$*=0.08,* $\Delta\chi$*=*$\Delta\psi$*=0.011,* $\Delta\sigma_0^{IBFD}$*=0.001,* $\Delta\sigma_0^{ADI}$*=0.002,* p_0*=267 kPa,* f_0*=2 MHz,* n*=3 and* θ_y^{Sim}*=*θ_y^{Steer}*=0°.*

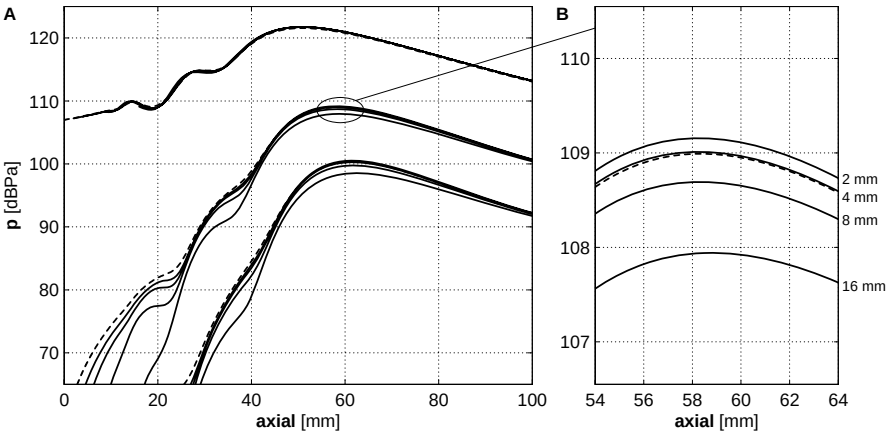

Figure 1.5: *Harmonic profiles from a 64 element phased array transducer. --- 3D-KZK solution, — two-stage 3D-KZK method. Simulation settings:* d_{KZK}*=2, 4, 8, and 16 mm,* $\Delta\tau$*=0.08,* $\Delta\chi$*=*$\Delta\psi$*=0.022,* $\Delta\sigma_0^{IBFD}$*=0.001,* $\Delta\sigma_0^{ADI}$*=0.002,* p_0*=267 kPa,* f_0*=2 MHz,* n*=3 and* θ_y^{Sim}*=*θ_y^{Steer}*=0°.*

It is unclear where this difference originates from. With the off-axis validity results of figure 1.3 it is unlikely resulting from the break down of the parabolic approximation.

To investigate the influence of the offset d_{KZK}, which defines the range over which the propagation is simulated linearly, simulations for offsets of 2, 4, 8 and 16 mm were performed (see figure 1.5). Up to an offset of 8 mm negligible differences between the result of the 3D-KZK solution and the two-stage 3D-KZK method are observed in the focal region of the second harmonic profile. For an offset of 16 mm, however, a significant difference of about 1 dB has been reached. With a minimal distance between the transducer's surface and the source field of 1 mm and a steering angle of 30°, the offset d_{KZK} for our phased array transducer is about 6 mm.

An example of a simulated steered acoustic beam is given in figure 1.6. The comparison with non-steered results show the lower amplitude in the focal region, the lower slope of the axial profiles in the far field, the larger beam width and the asymmetric side lobes of the steered beam.

The non-linear propagation of the source field took 1.5 hours on a 3 GHz processor with 1 GB of RAM. Unfortunately, it takes Field II 3 hours to calculate the source field resulting in a total simulation time of 4.5 hours for the profiles

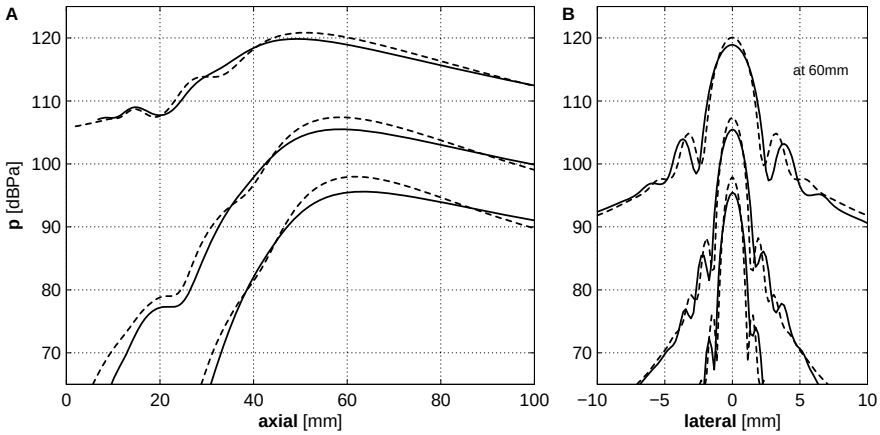

Figure 1.6: *Harmonic profiles from a 64 element phased array transducer. - - - $\theta_y^{Sim}=\theta_y^{Steer}=0°$, — $\theta_y^{Sim}=\theta_y^{Steer}=30°$. Simulation settings: d_{KZK}=2 and 5.8 mm, $\Delta\tau$=0.08, $\Delta\chi=\Delta\psi$=0.022, $\Delta\sigma_0^{IBFD}$=0.001, $\Delta\sigma_0^{ADI}$=0.002, p_0=267 kPa, f_0=2 MHz and n=3.*

shown in figure 1.6.

By using a different angle for the simulation θ_y^{Sim} and the steering θ_y^{Steer} of the acoustic beam we can investigate other regions of the acoustic field. Figure 1.7 gives an example of an acoustic beam steered under an angle of 30° and simulated with an angle of 30, 15 and 0°. For simulation angles of 15 and 0° the beam is not well diffracted in the lateral direction due to the parabolic approximation. However, when we use the valid parts from the three simulation results we can compose a beam profile over an view angle of 70° as is shown in figure 1.7.

1.4 Discussion

This chapter describes a simulation method for steered harmonic acoustic beams from phased array transducers. The algorithm used is a numerical solution of the KZK equation. Good agreement is shown with linear and nonlinear algorithms that do not originate from the KZK equation.

The limitations of the KZK equation resulting from the employed parabolic approximation has been investigated in several publications. For a baffled piston Tjotta *et al.* [1980] derived that the range of validity is given by

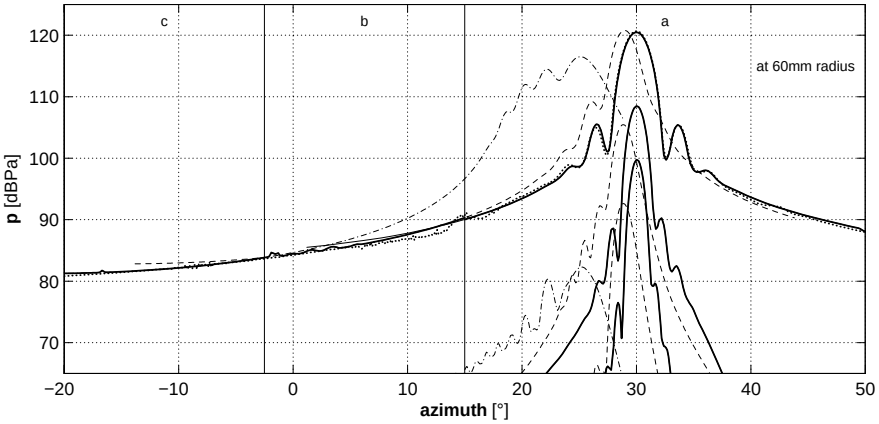

Figure 1.7: *Harmonic radial profiles from a 64 element phased array transducer simulated at three different angles, with a fixed steering angle. Thin lines: — θ_y^{Sim}=30°, - - - θ_y^{Sim}=15°, -·- θ_y^{Sim}=0°, ··· Field II. Thick line: — composite profile, composed from range a, b and c. Simulation settings: d_{KZK}=5.8, 4.5 and 2 mm, $\Delta\tau$=0.08, $\Delta\chi$=$\Delta\psi$=0.022, $\Delta\sigma_0^{IBFD}$=0.001, $\Delta\sigma_0^{ADI}$=0.002, p_0=267 kPa, f_0=2 MHz, n=3 and θ_y^{Steer}=30°.*

$z > a(ka)^{\frac{1}{3}}$, where k the wave number. This result was obtained for a well defined beams, which is ensured when $ka \gg 1$ (i.e. when the size of the aperture is many times larger than the wave length). Subsequent comparison with experimental results by Garrett *et al.* [1982] showed excellent agreement up to an off-axis angle of 20° in the post-focal region. For concave transducers Tjotta *et al.* [1991] derived a validity range of $z > \frac{d}{ka}\left(\frac{d}{a}\right)^{\frac{1}{3}}$ with the additional criteria $\frac{d}{a} \gg 1$ to ensure validity in the focal region. By comparing results from the linearized parabolic equation and the Helmholtz equation Tjotta *et al.* found that the parabolic approximation was good for value of $\frac{d}{a}$ down to 3.5 (i.e. a half aperture angle $\sin^{-1}\left(\frac{d}{a}\right)$ of about 16° or less). It was also mentioned that for cases involving apodization the domain of validity could be larger than predicted by these criteria. The above criteria were obtained for monochromatic sources.

Froysa *et al.* [1993] obtained similar criteria for pulsed concave transducers, by comparing results from the linearized parabolic equation and the full wave equation. Excellent agreement was obtained in the focal region for half aperture angles up to 16° at a fixed focusing gain of 10 and $ka \geq 100$. By

analogy of Tjotta *et al.* [1980] Kamakura *et al.* [1992] derived a validity range for rectangular transducers:

$$z > \frac{\sqrt{S}}{2}\left(\frac{k\sqrt{S}}{2}\right)^{\frac{1}{3}} \tag{1.32}$$

Where S is the surface of the aperture. As this criteria does not depend on the aspect ratio of the aperture it was mentioned that for aspect ratios beyond 5 a more precise expression for the acoustic beam would be preferable. Using a similar comparison as Tjotta *et al.* [1980] Baker *et al.* [1995] concluded that the errors introduced by the parabolic approximation are less important for rectangular than for circular apertures. Contradicting with Kamakura *et al.* it was also stated that more elongated apertures give better results. However, Kamakura *et al.* came to their conclusion comparing constant surface apertures while Baker *et al.* bisected a square transducer into $\frac{1}{2}$ and $\frac{1}{4}$ apertures. While the corners of the aperture for increasing aspect ratio are moving away from the propagation axis for Kamakura *et al.*, the opposite is happening for Baker et al.. Instead of the geometric mean, as used by Kamakura *et al.*, it might be better to use the quadratic mean for the validity range:

$$z > \sqrt{\frac{a^2+b^2}{2}}\left(k\sqrt{\frac{a^2+b^2}{2}}\right)^{\frac{1}{3}} = \sqrt{\frac{S\left(\frac{1}{A}+A\right)}{8}}\left(k\sqrt{\frac{S\left(\frac{1}{A}+A\right)}{8}}\right)^{\frac{1}{3}} \tag{1.33}$$

Where $2a$ and $2b$ are the dimensions of the rectangular aperture and A is the aspect ratio. In relation with Kamakura *et al.* this means that S is corrected by a factor $\frac{\frac{1}{A}+A}{2}$ which is 1 for a square aperture but increases with an increasing aspect ratio resulting in an increasing validity boundary.

Confirming the result of Garrett *et al.* for rectangular transducers, Baker *et al.* obtained identical results in comparison with their analytical solutions up to an off-axis angle of about 20° in the focal region. By comparing the directivity function for the parabolic approximation of a baffled piston transducer with the exact solution Hamilton *et al.* [1998] came to the same validity boundary for the off-axis angle of about 20° in the far field.

As no thorough assessment of the range of validity has been made for phased array transducers we can only estimate it from the validity results for other transducer geometries. Using the criteria of Kamakura *et al.* the validity range boundary for our transducer is 30.3 mm and with the proposed correction 32.5 mm. For a focused piston transducer with equal surface the validity range boundary would be much smaller, namely 15.9 mm. The additional condition of the half aperture angle is also well within range with

8.2°. From these results and the comparison with the ASM, presented in this chapter, it is safe to say that the parabolic approximation is valid in and beyond the focal region for our transducer. In general diagnostic ultrasound transducers for adult cardiac imaging exhibit dimensions and focal distances that allows the parabolic approximation to be made.

The off-axis validity boundary has been intuitively explored by comparing results from the linearized two-stage 3D-KZK method and Field II. Judging from the results an off-axis validity boundary of 20°, as found by several investigators, seems to be a conservative value.

In addition it has been anticipated that our two-stage algorithm does not significantly effect the harmonic levels in and beyond the focal region for steering angles up to 30°. Experimental validation of this finding is the subject of a chapter 2.

In a recent publication by Yang *et al.* [2005] a time domain algorithm for rectangular transducers was implemented for both the Crank-Nicolson finite difference (CNFD) method and the ADI method. The methods showed equal results but their ADI implementation needed double memory and 10 % more processor time. The memory demand of our 3D-KZK solution is equal to the size of the pressure matrix P with a negligible amount of overhead. As this is the minimal amount of memory needed to run a time-domain algorithm it is unlikely that the ADI method is less efficient than the CNFD method.

The 3D-KZK solution presented in this chapter can be readily extended to include non-frequency squared dependent absorption with a time or frequency domain solution [Yang 2005, Khokhlova 2006]. In addition, a second-order operator splitting approach could be introduced to further increase the efficiency the algorithm [Tavakkoli 1998, Zemp 2003].

1.5 Conclusion

Using the presented two-stage 3D-KZK method it is feasible to simulate steered harmonic beams from phased array transducers. The algorithm is based on the nonlinear parabolic wave equation. Good agreement is found between linear and non-linear algorithms that do not make use of the parabolic approximation.

Acknowledgements

The authors wish to thank Koos Huijssen of the Delft University of Technology (Delft, The Netherlands) for his assistance with the ASM simulations.

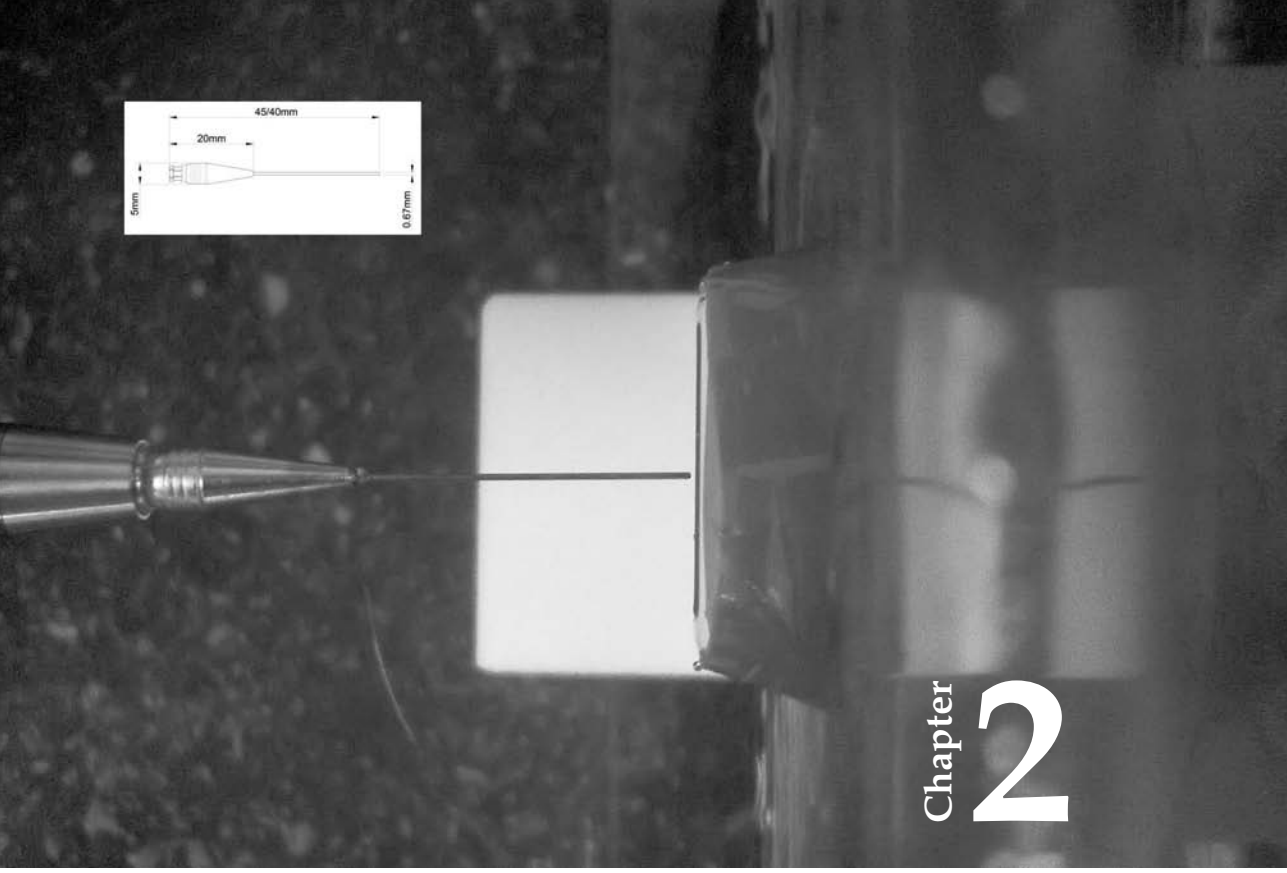

Chapter 2

Simulation of Steered Harmonic Acoustic Beams from Medical Transducers

Part II: Experimental Validation

Rotterdam, October 27th, 2006: *Hydrophone measurement at 0.25 mm from the transducer's surface. With the value of only the hydrophone needle (see inset) being €4000 (including a high accuracy NPL calibration), one should not try this at home.*

The use of a recently developed simulation tool for harmonic medical transducers is compared with measurements. The employed two-stage 3D-KZK method allows the simulation of steered harmonic acoustic beams from apertures with arbitrary geometry. A commercially available 64 element phased array transducer was used to validate the method.

Good agreement is shown between simulations and measurements within the known limitations of both. The feasibility of harmonic level estimation in grating lobes is demonstrated and the suppression of grating lobes for harmonic imaging is shown.

Based on:

Voormolen, M.M., G.M. Matte, N. de Jong and A. Bouakaz. Simulation of steered harmonic acoustic beams from medical transducers - Part II: Experimental validation. *The Journal of the Acoustical Society of America*, submitted, 2007.

2.1 Introduction

From its introduction in the late 90's, tissue harmonic imaging has become the most frequently used imaging modality of diagnostic echography [Ward 1997, Spencer 1998, Tranquart 1999]. The main advantages of harmonic imaging are: a narrower beam width, resulting in a improved lateral resolution, lower side lobes and suppressed reverberations in surface layers, both reducing the clutter [Humphrey 2000]. Designing harmonic medical transducers that fully exploit these advantages has become obvious since.

To assist an efficient development of new harmonic medical transducers, it is desirable to simulate the propagation of nonlinear acoustic beams from apertures with arbitrary geometry. A numerical solution to compute steered nonlinear pressure fields from such sources has been presented in the previous article chapter. In this chapter we compare measurements with simulations.

2.2 Methods

The transducer used for the experimental validation, the simulation method and the measurement set-up are discussed in the following subsections.

2.2.1 Phased Array Transducer

To validate our simulation method we used a GE VingMed Ultrasound (Horten, Norway) Vivid 5 system with a FPA-2.5MHz-1C transducer (see figure 2.1). The FPA-2.5MHz-1C is a 64 element phased array transducer with a 290 μm pitch and a 50 μm kerf. The height of the aperture is 12.5 mm. The acoustical lens has a fixed elevation focus of 71 mm and covers 84 % of the total height (i.e. leaving 1 mm of unfocused aperture on both ends). In addition some apodization, due to the clamping of the array, was present in the elevation direction. Therefore, a quadratic apodization down to $\frac{1}{4}$ of the amplitude was set for 1.5 mm at both ends. For the measurements presented here a 2 MHz excitation pulse with a duration of 2.5 cycles was used. The transmission focus was set at 62 mm.

2.2.2 Simulation

The simulations were computed with a recently developed two-stage 3D-KZK method. In short: Field II is used to calculate the pressure distribution close

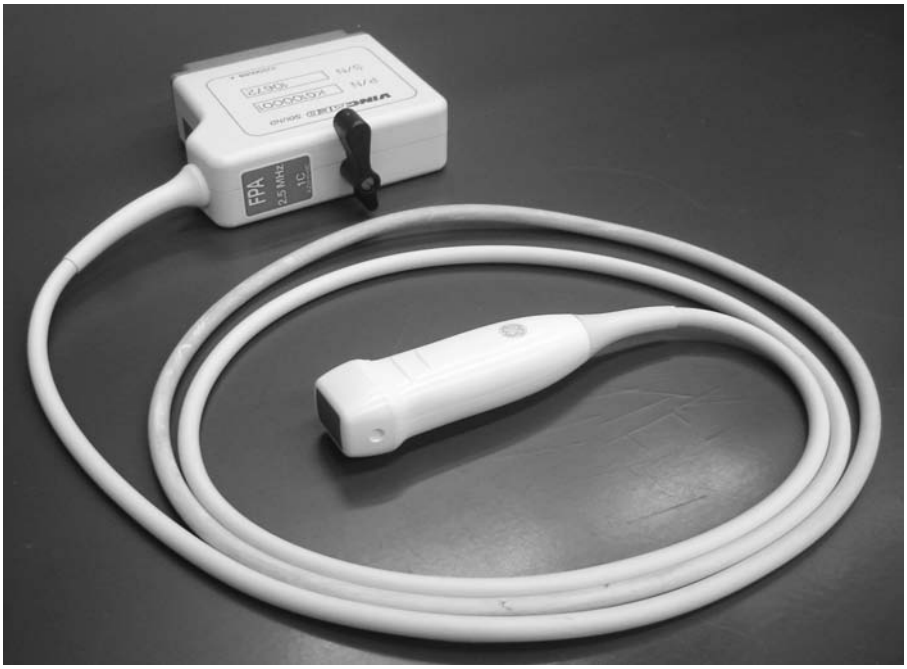

Figure 2.1: *The FPA-2.5MHz-1C transducer used for the validation of the simulation tool.*

to the transducer's surface, at a plane perpendicular to the direction of interest [Jensen 1992]. The source plane is then propagated with a numerical solution of the KZK equation. The method allows the simulation of nonlinear steered acoustical beams from apertures with an arbitrary geometry. A detailed description of the method can be found in chapter 1.

The transducer is excited with a rectangular pulse. A good estimate of the emitted wave was obtained using a hyper-Gaussian pulse of the following form:

$$f(t) = -e^{-\left(\frac{\omega_0 t}{\pi n}\right)^4} cos(\omega_0 t) \tag{2.1}$$

Where ω_0 is the angular frequency of the emitted pressure wave, t is the time and n is the number of cycles. Remaining simulation settings are: the offset of the 3D-KZK solution grid d_{KZK}, the resolution of the dimensionless time variable $\Delta\tau$, the resolution of the dimensionless transverse direction coordinates $\Delta\chi$ and $\Delta\psi$, the initial spacing of the dimensionless range coordinate

for the implicit backwards finite difference method $\Delta\sigma_0^{IBFD}$ and the alternating direction method $\Delta\sigma_0^{ADI}$ and the characteristic pressure p_0 (i.e. source pressure amplitude). For a detailed description of these parameters we refer to chapter 1.

2.2.3 Measurement Set-up

Hydrophone measurements were performed with a 0.2 mm diameter needle hydrophone (Precision Acoustics, Dorchester, UK). The hydrophone was calibrated by the National Physical Laboratory (Teddington, UK) with a remaining uncertainty of 9 % in the range of 0.5 to 6 MHz. Pressure signals were recorded using a LeCroy 9400A oscilloscope (Chestnut Ridge, New York, USA). The needle hydrophone can be manoeuvered through the water tank in which the transducer is mounted using an xyz-system (Time & Precision Industries, Hampshire, UK). The hydrophone can be moved in all three perpendicular directions with a minimum step size of 5 μm. Before each beam profile measurement the tip of the hydrophone is set in the direction of the acoustic beam. The relatively small directional dependency of the hydrophone (1 dB at ±20° for 6 MHz) allowed for manual adjustment in this case. Figure 2.2 shows the hydrophone set up for the measurement of a 30° steered acoustic beam.

A calibration routine is used to determine the exact position of the acoustic beam and the steering plane of the transducer. The accuracy of this routine is 100 μm. To facilitate the measurement of axial and transverse profiles with high spatial accuracy, a coordinate system transformation is used (based on the calibration results) to manoeuvre the hydrophone. The recorded signals were averaged 30 or 100 times depending on their strength. The water temperature during the hydrophone measurements was 23°, resulting in the following medium parameters for the simulation: a small signal ambient sound speed c_0 of 1491.1 m/s, a thermoviscous absorption coefficient α of 91.5 mNeper/m/MHz, a coefficient of nonlinearity β of 3.52 and a ambient density ρ_0 of 997.6 kg/m^3 [Duck 1990]. The source pressure p_0 for the various configurations was determined by matching the fundamental profile of the measurements and the simulations.

Beam profiles are presented as the envelope amplitude of the time signal. The harmonic profiles are obtained with an 8$^{\text{th}}$ order Butterworth filter. The first three harmonics are shown (including the fundamental component), unless otherwise indicated. To simplify the presentation, the axial profile always originates from the center of the transducer and is aligned with the axis of the

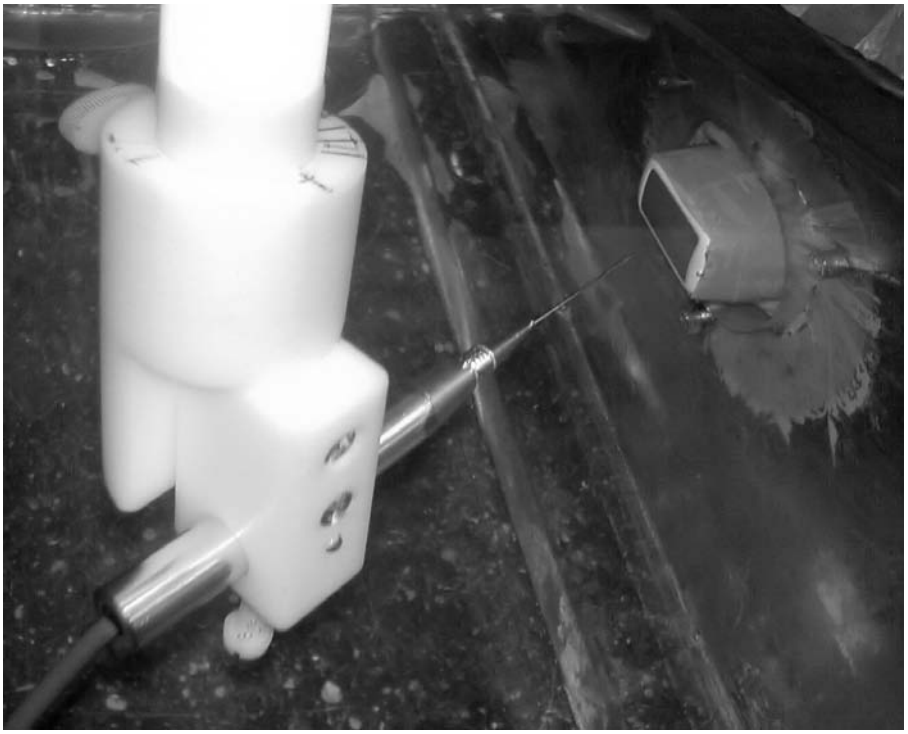

Figure 2.2: *Measurement set-up for a 30° steered acoustic beam.*

acoustic beam or grating lobe.

2.3 Results

Figure 2.3 shows the simulation and measurement results for a non-steered acoustic beam at low source pressure (34.2 kPa). Most noticeable is the moderate underestimation of the harmonic levels (about 3 dB in the focal area for the second harmonic). With the hydrophone as major source of errors the accuracy of the measurement is about 1 dB. The significant underestimation in figure 2.3 is most likely due to an underestimation of the emitted harmonic frequency components in the source field. With a signal-to-noise ratio of approximately 50 dB, figure 2.3 also shows that a source pressure of about 35 kPa

Table 2.1: *Beam with and side lobe levels from fundamental and second harmonic lateral profiles for a non-steered and a 30° steered beam at a depth of 66 and 63 mm respectively.*

steering angle		**beam width** (mm)		**side lobe level** (dB)	
		measurement	simulation	measurement	simulation
0°	fundamental	3.2	3.1	13.9	14.9
	2nd harmonic	2.0	1.9	16.3	18.0
30°	fundamental	3.5	3.3	13.4	14.2
	2nd harmonic	2.1	2.1	16.1	18.0

is the lower limit for our experimental set-up. Lower source pressures will not allow the measurement of a full axial beam profile for the second harmonic.

Figure 2.4 shows that for higher source pressures (300 kPa), good agreement between simulation and measurement is found in the focal area and far field of the axial profile. As with the low source pressure profiles (see figure 2.3), the harmonic levels are behind in the near field. However, this has no consequences for the validity in the focal area and the far field. The shape of the simulated transverse profiles match well with the measured once. However, the side lobe levels of the elevation profile is slightly overestimated and the side lobe levels of the harmonic lateral profiles is slightly underestimated. Despite the efforts to model the transducer several properties could not be accounted for, such as: the sensitivity variations between the elements, irregularities in the backing, matching layer(s) and / or acoustic lens (or their bonding) and side effects from the housing. The suboptimal fit of the fundamental component in the pre-focal area is also an indication for discrepancies between the transducer / excitation model and the FPA-2.5MHz-1C transducer [Kamakura 1992].

The time waveform shown in figure 2.4 clearly shows the nonlinear distortion due to propagation. Good agreement is demonstrated between the simulated and measured waveform.

The narrower beam width and reduced side lobes of the second harmonic profiles, in comparison with the fundamental profiles, can be clearly appreciated from figure 2.4 and table 2.1. The beam width and side lobe level values of the simulation show good agreement with the measurement.

Similar agreement, as with the non-steered acoustic beam, was obtained for a 30° steered beam at high source pressure. Figure 2.5 depicts the simulation and measurement results. Table 2.1 shows the slightly deteriorated

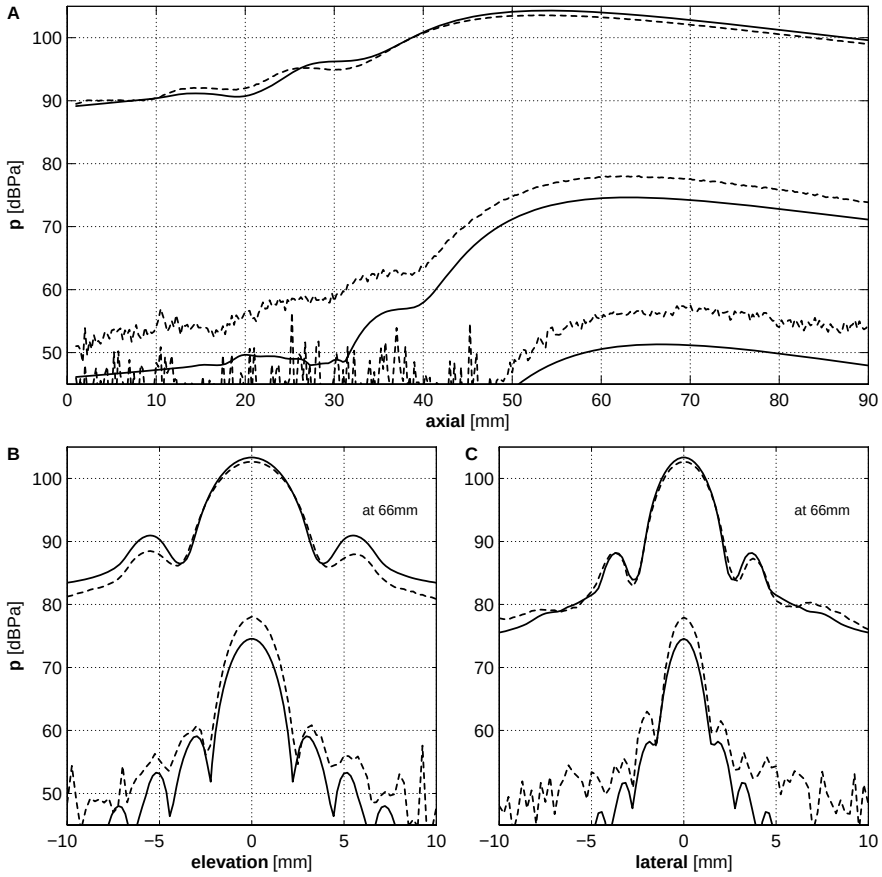

Figure 2.3: *Profiles of a non-steered acoustic beam at low source pressure. - - - measurement, — simulation.* ***B*** *and* ***C.*** *For clarity the third harmonic has been excluded. Simulation settings:* d_{KZK}*=1 mm,* $\Delta\tau$*=0.08,* $\Delta\chi$*=*$\Delta\psi$*=0.022,* $\Delta\sigma_0^{IBFD}$*=0.001,* $\Delta\sigma_0^{ADI}$*=0.002,* p_0*=34.2 kPa and n=2.7.*

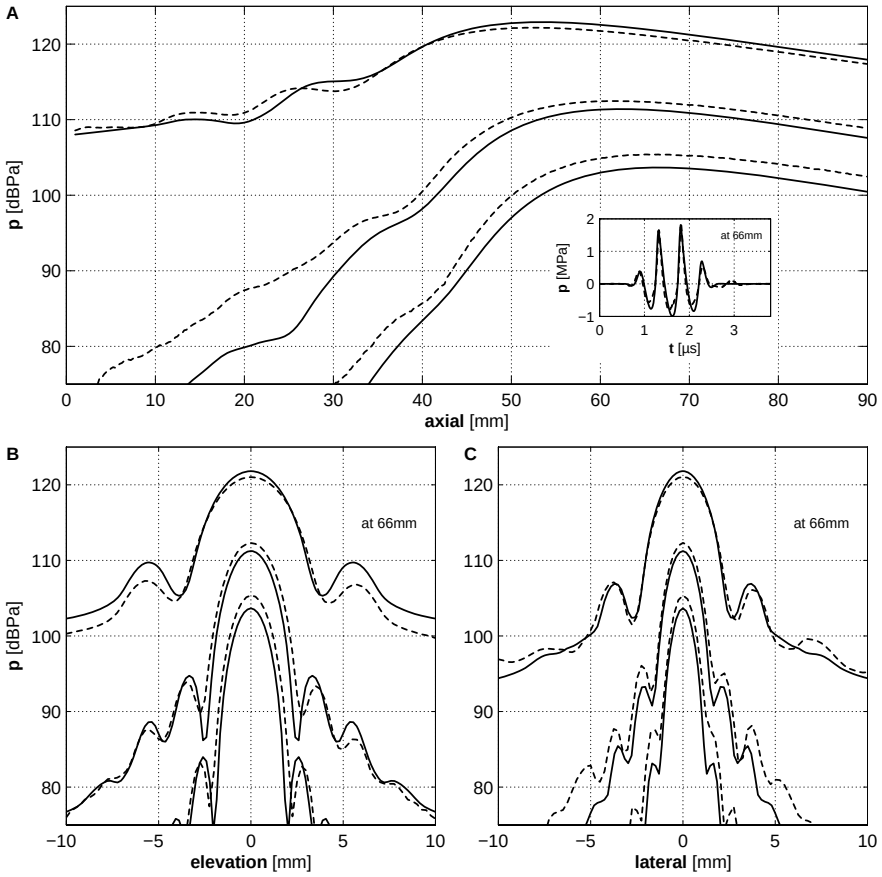

Figure 2.4: *Profiles and time signals of a non-steered acoustic beam at high source pressure. - - - measurement, — simulation. Simulation settings:* d_{KZK}*=1 mm,* $\Delta\tau$*=0.08,* $\Delta\chi$*=*$\Delta\psi$*=0.022,* $\Delta\sigma_0^{IBFD}$*=0.001,* $\Delta\sigma_0^{ADI}$*=0.002,* p_0*=300 kPa and n=2.7.*

beam width and side lobe levels of the lateral profile, when compared with the non-steered case. In the focal area of the axial profiles a difference between simulation and measurements of about 1 dB can be observed for the fundamental and second harmonic components. The third harmonic has a somewhat larger difference of about 1.5 dB. As mentioned by Baker *et al.* [1995], this can be improved by using a larger temporal resolution at the expense of a higher memory demand and a longer computation time.

Good agreement between simulation and measurement was again found when only every third element of the phased array was enabled. The results of a 30° steered acoustic beam in this triple pitch configuration is shown in figure 2.6. Although the profiles are in good agreement, the slope of the simulated axial profile is slightly higher and the side lobes of the lateral profile are significantly shifted inwards. This could however be the result of crosstalk between the elements as two thirds of the elements were simply disabled, not removed.

The simulation and measurement results of the grating lobe evoked by the triple pitch configuration is shown in figure 2.7. The angles at which grating lobes appear can be found with the following equation [Szabo 2004]:

$$\theta_{Grating} = \pm \arcsin\left(\frac{m\lambda}{d_{Pitch}} + \sin\left(\theta_{Steer}\right)\right), \quad m \in \{\cdots, -3, -2, -1, 1, 2, 3, \cdots\} \tag{2.2}$$

Where $\theta_{Grating}$ is the grating lobe angle, λ is the wavelength, d_{Pitch} is pitch and θ_{Steer} is the steering angle. For m is -1 equation 2.2 predicts a grating lobe at $-20.9°$.

The accuracy of the transducer and / or excitation model, clearly become more critical for a correct estimation of the harmonic levels in the grating lobe. Although the harmonic levels are significantly underestimated, the shape of the grating lobe is well captured. In addition it can be seen from figure 2.6 and 2.7 that the grating lobe is suppressed for harmonic imaging when compared to fundamental levels [Duck 2002]. While the ratio between main beam and grating lobe is about 9 dB for the fundamental components, it is approximately 15 dB for the harmonic components. The simulation results show a main beam / grating lobe ratio of about 10 and 18 dB for fundamental and second harmonic components respectively.

To illustrate the capabilities of our simulation tool figure 2.8 combines the simulation results of figure 2.6 and 2.7. The harmonic profiles of both the main beam and grating lobe are depicted in a radial profile covering an angle of 80°.

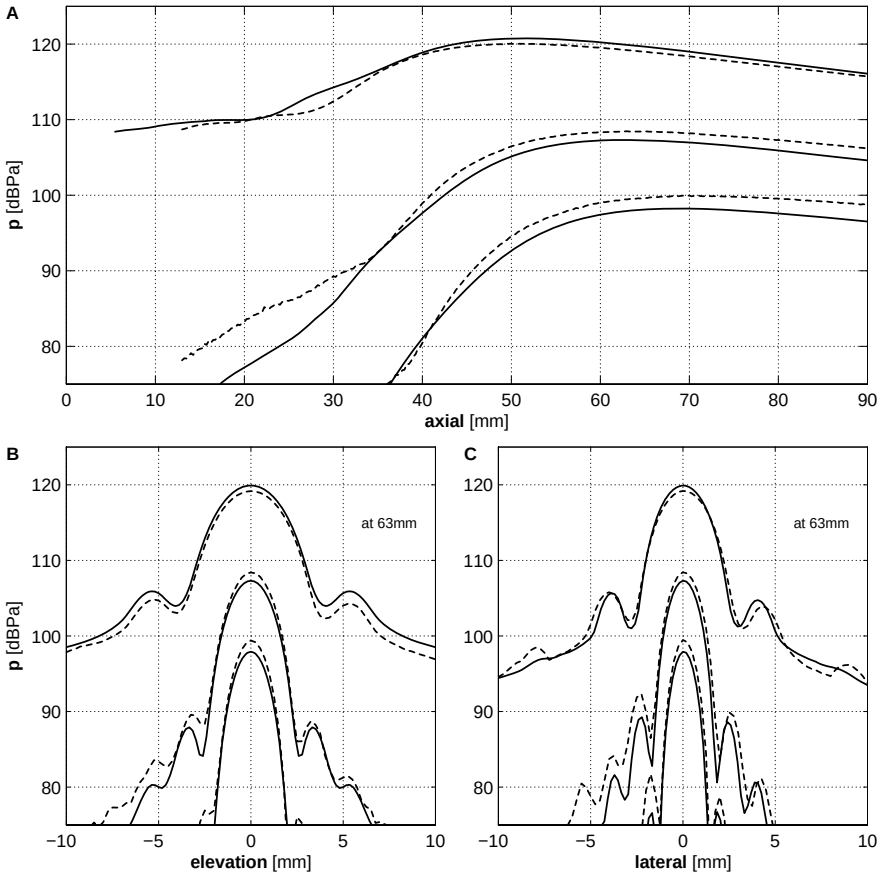

Figure 2.5: *Profiles of a 30° steered acoustic beam at high source pressure. - - - measurement, — simulation. Simulation settings:* d_{KZK}*=5.5 mm,* $\Delta\tau$*=0.08,* $\Delta\chi$*=*$\Delta\psi$*=0.023,* $\Delta\sigma_0^{IBFD}$*=0.001,* $\Delta\sigma_0^{ADI}$*=0.002,* p_0*=300 kPa and n=2.7.*

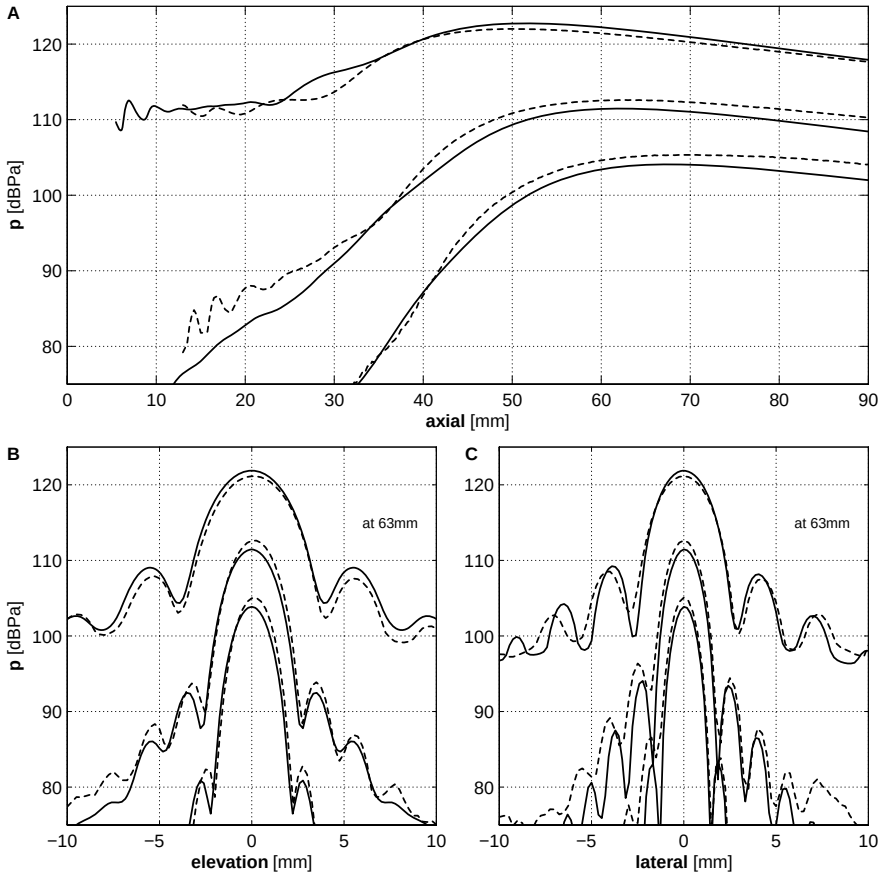

Figure 2.6: *Profiles of a 30° steered acoustic beam in triple pitch configuration. --- measurement, — simulation. Simulation settings:* d_{KZK}*=5.5 mm,* $\Delta\tau$*=0.08,* $\Delta\chi$*=*$\Delta\psi$*=0.023,* $\Delta\sigma_0^{IBFD}$*=0.001,* $\Delta\sigma_0^{ADI}$*=0.002,* p_0*=1.07 MPa and n=5.4.*

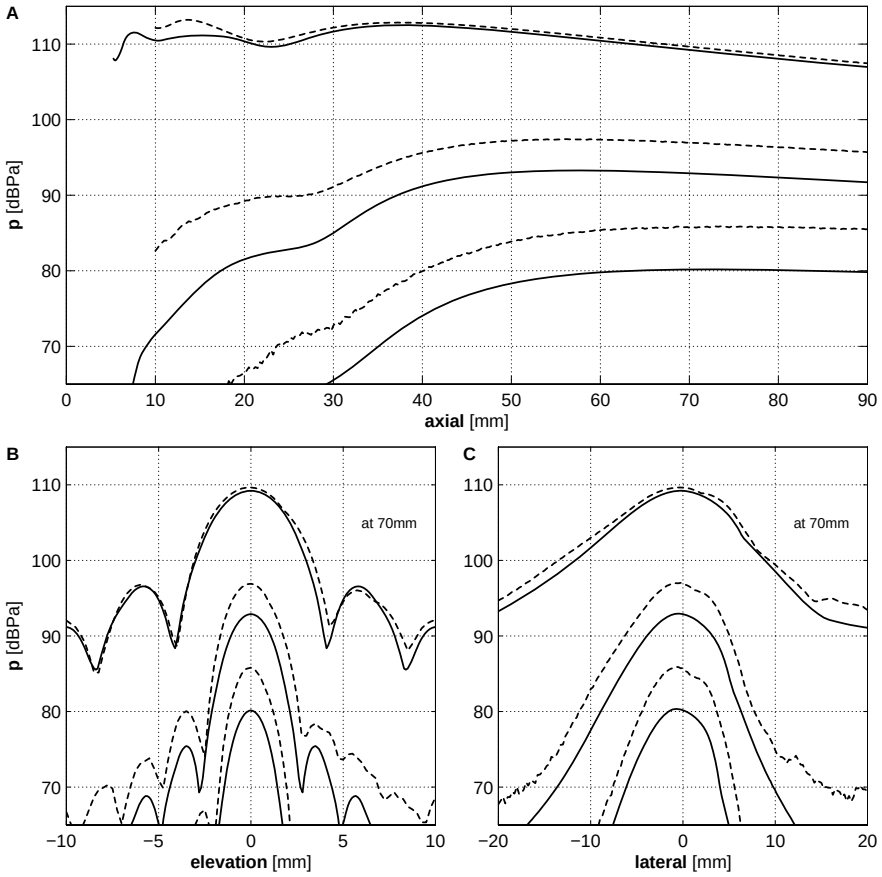

Figure 2.7: *Profiles of the grating lobe (at ≈−20.9°) from a 30° steered acoustic beam in triple pitch configuration. --- measurement, — simulation. Simulation settings:* d_{KZK}*=5.5 mm,* $\Delta\tau$*=0.16,* $\Delta\chi$*=*$\Delta\psi$*=0.022,* $\Delta\sigma_0^{IBFD}$*=0.001,* $\Delta\sigma_0^{ADI}$*=0.002,* p_0*=1.07 MPa and n=5.4.*

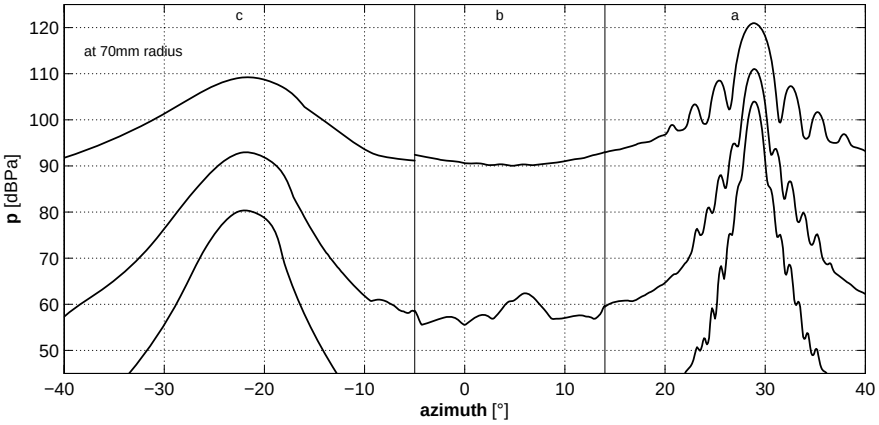

Figure 2.8: *Composite radial profile from three separate simulations, showing a 30° steered acoustic beam and its grating lobe in triple pitch configuration. Simulation angle:* ***a.*** *30°,* ***b.*** *5° and* ***c.*** *−21.9°. Simulation settings:* d_{KZK}*=5.5 mm,* $\Delta\tau$*=0.08, 0.16 and 0.16,* $\Delta\chi$*=*$\Delta\psi$*=0.022,* $\Delta\sigma_0^{IBFD}$*=0.001,* $\Delta\sigma_0^{ADI}$*=0.002,* p_0*=1.07 MPa and n=5.4.*

2.4 Discussion

Good agreement is shown between simulated and measured profiles for non-steered and steered acoustic beams from a phased array transducer. The feasibility of simulating harmonic grating lobes is also demonstrated although accurate modeling of the transducer and its excitation is believed to be more critical here. As suggested by Nachef *et al.* [1995] the underestimation of the harmonic levels could also be caused by non-negligible amplitude dependent variations in the parameter of nonlinearity not accounted for in the KZK equation Nachef *et al.* [1995]. Given the good agreement with the measurements for the other high pressure simulations this is however less likely. Better results could also have been obtained by propagating a measured source field very close to the transducer's surface as used by Cahill *et al.* [1998]. However, this is not the intended application of the simulation tool since this requires an existing transducer while the two-stage 3D-KZK simulator is meant to assist the design of new transducers, before prototyping.

Although simulations could take days, the first algorithm for the simulation of array transducers was developed by Cahill *et al.* [1998]. This is also one of the two publication in which simulation results are experimentally

validated with measurements from a phased array transducer. Reasonable agreement was achieved with their frequency domain solution for a small 8 element phased array transducer. The other experimental validated solution for array transducer simulations was developed by Bouakaz *et al.* [2003b]. This time domain solution showed good agreement with a 64 element phased array transducer. A combined frequency-time domain solution to simulate array transducers was developed by Zemp *et al.* [2003]. Good agreement was found in a comparison with piston and concave transducers. On a 533 MHz processor with 512 MB of random access memory (RAM) the harmonic field from a 64 element phased array up to a range of 60 mm could be simulated in 5 hours. More recently a time domain and a frequency-time domain method were presented by Yang *et al.* [2005] and Khokhlova *et al.* [2006] respectively. Although capable of simulating array transducers only results from rectangular transducers are shown. On a 1.5GHz processor the field from a rectangular transducer could be simulated up to a range of 100 mm in 9 hours with the method of Yang *et al.* [2005].

The above methods do not allow the simulation steered harmonic acoustic beams. Very recently however, Christopher *et al.* [2006] proposed a multi-stage method, as an extension to the solution developed by Zemp *et al.* [2003], to allow the simulation of steered beams. Steered axial beam profiles from a 64 element phased array are shown and could be calculated up to a range of 90 mm in 1.5 hours on a 1.2 GHz processor. The non-linear propagation of the initial field up to 100 mm for the results shown in figure 2.5 took 1.5 hours on a 3 GHz processor with 1 GB of RAM. Unfortunately, it takes Field II 3 hours to calculate the initial field. Calculating the initial field with a more dedicated algorithm will drastically reduce the total computation time.

2.5 Conclusion

The two-stage 3D-KZK method accurately predicts harmonic levels of non-steered and steered acoustic beams from a phased array transducer. The feasibility of simulating harmonic grating lobes is demonstrated and the suppression of grating lobes for harmonic imaging is shown.

Acknowledgements

The authors wish to thank Johan Kirkhorn of GE VingMed Ultrasound (Horten, Norway) for his assistance with the hydrophone measurement.

Chapter 3

Harmonic 3D Echocardiography with a Fast-Rotating Ultrasound Transducer

Waikiki Beach, Honolulu, October 5th, 2003: *Part of this chapter was presented at the IEEE Ultrasonics Symposium in Hawaii, where I also had the opportunity to study other wave phenomena.*

Although the advantages of three dimensional (3D) echocardiography have been acknowledged, its application for routine diagnosis is still very limited. This is mainly due to the relatively long acquisition time. Only recently has this problem been addressed with the introduction of new real-time 3D echo systems. This chapter describes the design, characteristics, and capabilities of an alternative concept for rapid 3D echocardiographic recordings.

The presented fast-rotating ultrasound (FRU)-transducer is based on a 64-element phased array that rotates with a maximum speed of 8 Hz (480 rpm). The large bandwidth of the FRU-transducer makes it highly suitable for tissue and contrast harmonic imaging. The transducer presents itself as a conventional phased-array transducer; therefore, it is easily implemented on existing 2D echo systems, without additional interfacing.

The capabilities of the FRU-transducer are illustrated with in-vitro volume measurements, harmonic imaging in combination with a contrast agent, and a preliminary clinical study.

Based on:

© 2006 IEEE. Reprinted, with permission, from: **Voormolen, M.M.**, B.J. Krenning, C.T. Lancée, F.J. ten Cate, J.R.T.C. Roelandt, A.F.W. van der Steen and N. de Jong. Harmonic 3D Echocardiography with a Fast-Rotating Ultrasound Transducer. *IEEE Transactions on Ultrasonics, Ferroelectrics and Frequency Control*, 53(10):1739–1748, 2006.

3.1 Introduction

Over the last 20 years the application of three dimensional (3D) echocadiography has been explored extensively. The reconstruction of unconventional 2D views from a 3D dataset has been seen as a welcome addition to the possibilities of echocardiography [Pandian 1994]. Also, the examination of volume-rendered 3D recordings, the so-called *surgical view*, has proven very useful for the preparation of surgical interventions [Roelandt 2000]. In addition, many studies have validated the increased accuracy obtained with the quantification of cardiac structures from 3D data as compared to 2D data [Krenning 2003].

In spite of its advantages, 3D echocardiography is still mainly used for research purposes. Most 3D echocardiographic techniques developed in the past are based on the stepwise displacement of a phased array [Delabays 1995, Roelandt 1995, Papavassiliou 1998]. With these techniques, only one position is covered during a cardiac cycle. The subsequent cycle then is used to move to the next location. This relatively slow process prolongs the acquisition time beyond the feasible duration of a single breath hold, which in turn calls for respiratory and electrocardiogram (ECG) gating. For a densely sampled 3D recording, the process described above requires an acquisition time of several minutes. The recordings often suffer from motion artefacts as a result of the lengthy acquisition time. Although the acquisition of a 3D dataset does not consume more time than alternative techniques, such as magnetic resonance imaging (MRI), it is still considered a drawback. As long as standard 2D examinations are performed in the same amount of time as a single 3D recording, it will not likely be widely accepted in daily clinical practice.

Real-time 3D echocardiography solves the problem of lengthy acquisition times; however, first-generation realtime 3D echo systems suffered from insufficient image quality [Sheikh 1991]. The recently introduced second-generation systems from Philips Medical Systems (Best, The Netherlands) and General Electric (Milwaukee, Wisconsin, USA) possess an improved image quality. These commercially available systems have resulted in the increased use of 3D echocardiography for routine diagnosis [Von Bardeleben 2004].

State-of-the-art 2D echo systems cover two spatial dimensions and time with sufficient spatial and temporal resolution. Therefore, the key to fast acquisition of a 3D dataset is an effective coverage of the third spatial dimension. With stepwise, displaced phased arrays, more frames are discarded during motion and gating than used for the actual 3D dataset. However, a phased

array moved in a continuous, uniform motion would be able to make use of the full frame rate. This chapter describes the design, characteristics, and capabilities of a continuous, rotating, phased-array transducer intended for rapid 3D echocardiographic recordings.

3.2 Materials and Methods

In the first subsection, the transducers design and its consequences for the acquisition morphology will be described. The rotation speed of the transducer is not stored with the echo data but is extracted from it. The technique to recover the rotation speed from the data is explained in a subsequent subsection. The process needed for the reconstruction and quantification of a scanned volume will be discussed. The optimization of the rotation speed for the clinical setting is described.

3.2.1 The Fast-Rotating Ultrasound Transducer

The fast-rotating ultrasound (FRU)-transducer consists of three major parts: a high precision drive, a slip-ring device, and a phased array. Figure 3.1 shows the latest prototype of the transducer [Djoa 2000]. Key features of the transducer are its wide bandwidth, allowing harmonic imaging, and its ergonomic design (width: 53 mm, height: 33 mm, length: 147 mm, and weight: 350 g).

The drive of the transducer consists of a direct current (DC) motor, a gear, an encoder, and a controller (see figure 3.1). The DC motor, gear, and chain wheel transmission combination produce a maximum torque of 85 mNm, which is well above the torque required to drive the slip-ring and the array. The encoder and controller provide a feedback regulation for a highly constant rotation speed, which can be controlled manually. For the acquisition of a 3D dataset, the rotation speed is set between 4 and 8 Hz (240 and 480 rpm). In addition, the array can be positioned at two fixed stationary and perpendicular angles (0° and 90°) that are indicated with LED's on the housing of the transducer (see figure 3.1). Using a footswitch, these positions can be alternated for alignment of the transducer prior to the acquisition of a 3D dataset (e.g., by checking the four and two chamber views before a left ventricular acquisition).

The slip-ring device is custom made (Kaydon, Reading, Berkshire, UK) and contains 82 contacts, of which 64 are used for the array elements and 16

Figure 3.1: *The latest prototype of the fast-rotating ultrasound (FRU)-transducer. The upper panel shows the construction of the transducer with some key components annotated. The lower panel shows the transducer with its housing. Note the LEDs on the housing, which are used to indicate whether the phased array is located in one of its two fixed positions (0° and 90°).*

as distributed signal ground. No measurable noise generation from the slip-ring device could be detected within the frequency range used for imaging.

The transducer's array, custom made by Delft Instruments, Delft, The Netherlands, contains 64 elements with a pitch of 0.21 mm and is tapered into an octagonal shape, approximating a circle with a radius of 7 mm. It has a fractional bandwidth of 86 % with a center frequency of 3.2 MHz (see figure 3.2A). The fixed focus of the acoustic lens in the elevation direction is set at 60 mm. Figure 3.2B gives the lateral transmit beam profiles at the focal distance for an excitation frequency of 1.8 MHz and a pulse length of 2.5 cycles. At −6 dB a fundamental beam width of 3.86 mm and a harmonic beam width of 2.62 mm were found. The side lobe levels of both the fundamental and harmonic profile were equal to −18.1 dB.

The transducer is connected to a GE VingMed Ultrasound (Horten, Nor-

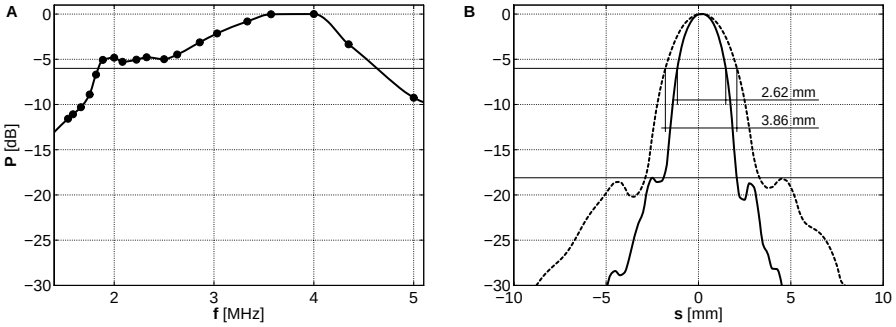

Figure 3.2: ***A.*** *Shows a normalized fundamental (dashed line) and harmonic (solid line) beam profiles in lateral direction for an excitation frequency of 1.8 MHz, a pulse length of 2.5 cycles, and a nonderated mechanical index (MI) of 1.7MI.* ***B.*** *Shows the transmit sensitivity of the transducer.*

way) Vivid 5 system like a conventional phased array, but it could be used with any scanner as no additional interfacing is required.

3.2.2 Morphology of the Acquisition

The typical acquisition time for a full 3D dataset is approximately 10 seconds, which allows for a dataset to be recorded within a single breath hold. With a standard frame rate of about 100 frames per second (fps), a typical dataset consists of approximately 1000 harmonic B-mode images. The frames are first stored in the scanner and later transferred to a computer for processing. The ECG signal is stored with the frames. No ECG gating is used, and exclusion of irregular cardiac cycles is carried out after the acquisition.

The continuous rotation of the array results in non-uniformly sampled 4D datasets (three spatial dimensions and time). First, the individual frames of the recording have a curved morphology in space, as shown in figure 3.3A. Second, the frames will sample the volume in an interleaved manner. This is most clearly illustrated in the spherical coordinate system, which is the native coordinate system of the acquisition (see figure 3.3B). In the spherical coordinate system, the frames are divided into halves by the imaging (or rotation) axis of the transducer. By definition, this is a consequence of the limited range of the elevation angle ($-\frac{1}{2}\pi$ to $\frac{1}{2}\pi$ rad), which represents the steering angle of the individual ultrasonic beams in the spherical domain. When a frame is acquired from right to left, the steering angle from the right

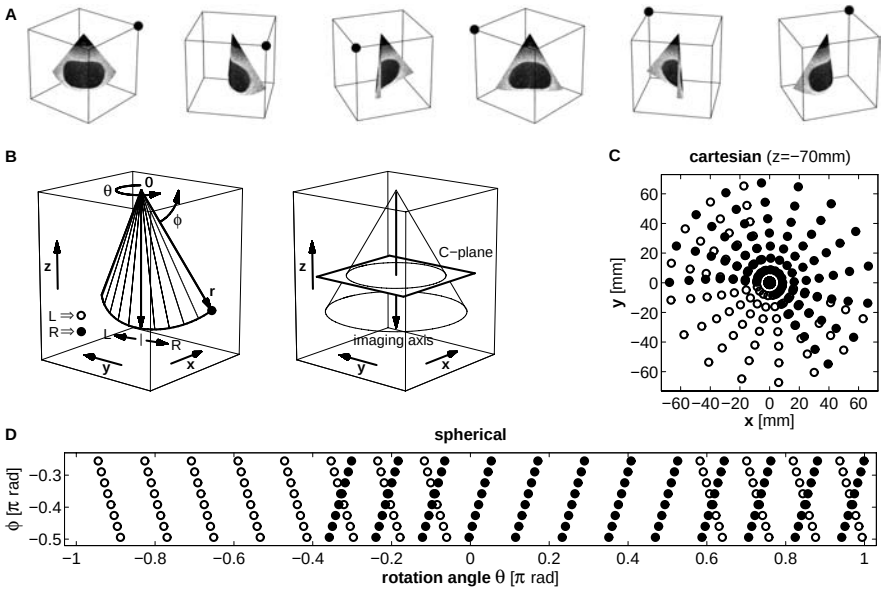

Figure 3.3: ***A.*** *Shows a typical 2D image recorded with the FRU-transducer from a cavity phantom in perspective. The consecutive frames repeat the same image, but each time rotated 60° clockwise. The sequence gives a good appreciation of the curved shape of the frame.* ***B.*** *The first part shows a curved frame and its relation to the spherical and cartesian coordinate system. The second part depicts the conical shape of the volume sampled by the FRU-transducer and the position of a C-plane. In addition, it is shown how a frame is divided by the imaging axis into a left and a right half, indicated with L and R.* ***C.*** *Shows the position of the ultrasonic beams from a number of frames in the cartesian coordinate system. Beams from the left half of the frames are indicated with an open dot and those from the right half with a closed dot (see also panel B).* ***D.*** *Shows the more orderly position of the same beams in the spherical coordinate system.*

half of the frame will run down. However, for the beams of the left half, the steering angle will run up. This results in inclined and intersecting rows of ultrasonic beams from the two frame halves (see figure 3.3D). The intersecting nature of the frame halves also can be observed in the cartesian coordinate system, but less clearly due to the curvature of the frames (see figure 3.3C).

From figure 3.3C, it also can be seen that the sample density increases toward the rotation axis. The uniformity of the sampling could be improved by optimizing the scanning in the 2D sector. In the cartesian coordinate system, which is used for visualization, there is no uniform sampling along any axis (see figure 3.3C). For volume rendered reviewing of recorded datasets, the data, therefore, are interpolated with the use of a uniform cartesian grid. Reconstruction can, of course, be performed only with the availability of an accurately determined rotation speed.

3.2.3 Determination of the Rotation Speed

To avoid additional interfacing between the echo system and the transducer, the rotation speed is extracted from the recorded harmonic B-mode data in two steps. A first estimate of the rotation speed is obtained by correlating all frames of the dataset with an arbitrary reference frame from the same dataset. The correlation value is calculated as the sum of absolute difference between the frames. An example of the resulting correlation signal is shown in figure 3.4A. The correlation result reveals a periodic signal with a periodicity related to the rotation speed. Fourier analysis of the correlation signal gives the first estimate of the rotation speed.

The accuracy of the first estimate of the rotation speed is limited to approximately 10 MHz due to noise and the interference of cardiac motion. To improve this accuracy, the rotation speed is corrected in a second step. End-diastolic C-planes are reconstructed from each recorded cardiac cycle. The C-plane of the first cardiac cycle is used as a reference for correlation with the C-planes of subsequent cycles. By maximizing the correlation between the planes, by rotating them around the rotation axis, the angular correction for each C-plane can be found. Figure 3.4B gives an example of the result from a C-plane correlation.

The correlation result of the C-planes shows a linear increase of the angular error due to the insufficient accuracy of the first rotation speed estimation. Using the regression of the C-plane correlation, the accuracy of the rotation speed can be increased an order of a magnitude beyond the first estimate. Typically, the residual angular error after the second order rotation speed estimation is not larger than a few degrees (see figure 3.4B), which is only

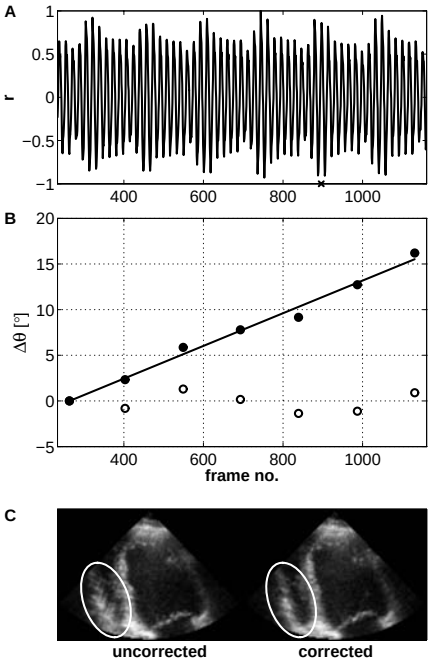

Figure 3.4: ***A.*** *Shows an example of a normalized frame-to-frame correlation signal r with the reference frame indicated by the cross on the x-axis. The value at the reference frame is a linear interpolation of the values of its neighboring frames and, therefore, is not equal to 1. Approximately 50 rotations are shown for a recording that was made with a frame rate of 106.1 fps.* ***B.*** *An example of the second order rotation speed estimation is shown. The regression (solid line) of the angular errors $\Delta\theta$ calculated (solid dots) resulted in a rotation speed correction of 5.3 MHz. The residual angular error after correction of the rotation speed also is shown (open dots).* ***C.*** *Shows two reconstructed long axis images of the left ventricular acquisition in question. For the image on the right, the second order rotation speed correction was used, but the left image did not use the second order correction. The circled area of the image on the left clearly shows the artefacts resulting from inaccuracies in the rotation speed used.*

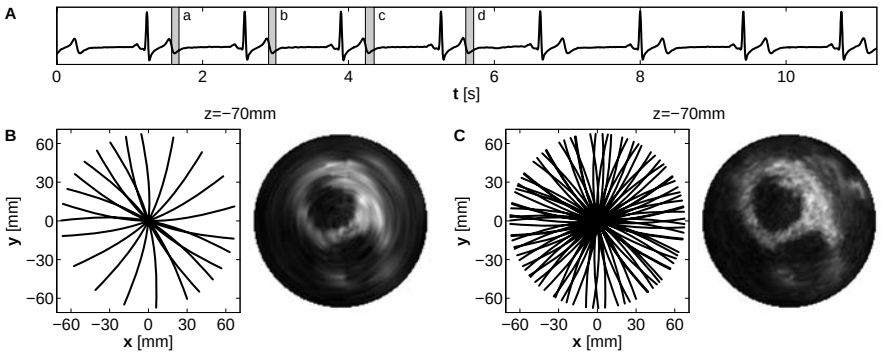

Figure 3.5: ***A.*** *The time intervals of four corresponding cardiac segments are indicated when each cardiac cycle is divided into 12 segments of equal width.* ***B.*** *If only segment a is used for reconstruction, a sparse sampling of the volume is obtained. Both the sampling of the rotation angle and the reconstruction of the corresponding C-plane for this case are depicted (z is the axial direction of the transducer; see also figure 3.3). The individual frames recorded within the time interval of the segment are indicated with solid lines.* ***C.*** *Shows the same results when all four segments are used. The denser sampling of the volume and the improved resolution of reconstructed images clearly can be appreciated.*

a fraction of the optimal angular resolution (see also appendix A). Figure 3.4C gives an example of the artefacts resulting from inaccuracies in the first estimate of the rotation speed. As can be seen from figure 3.4C, the artefacts are resolved when the second order estimate is used.

3.2.4 Reconstruction

Following the determination of an accurate rotation speed, 4D datasets can be constructed from the recorded frames. Datasets constructed from an acquisition of one cardiac cycle result in a sparse sampling of the time-volume space. To obtain a denser sampling of the time-volume space, a number of cardiac cycles are fused, which is also referred to as multibeat fusion.

Although the multibeat fusion results in a densely sampled 4D dataset of the scanned volume, the dataset still has a nonuniform structure. A suitable interpolation technique is used to resample the data into a uniformly spaced cartesian grid.

Figure 3.5 gives an example of the above techniques. The improved image quality obtained with the use of multibeat fusion is clearly depicted in figure

3.5.

3.2.5 Optimization of the Rotation Speed

For successful reconstruction, the acquired frames should be distributed adequately over the rotation angle. This distribution depends, in the first place, on the rotation speed and the frame rate. With the use of multibeat fusion, the distribution also is dependent on the heart rate and the number of cardiac segments (i.e., the number of time intervals in which the cardiac cycle is subdivided, typically 16). For a recording of a stationary volume with an arbitrary rotation speed, the minimum sampling interval of the rotation angle is the angle between two consecutive frames. For a cardiac recording, even this minimal resolution is not assured. It is not even unlikely that the frames from the cardiac segments used will end up in the same quadrant of the rotation angle. To prevent this from happening, an optimized rotation speed needs to be used for a given frame rate, heart rate, and number of cardiac segments. Appendix A gives the details of the calculation of such an optimized rotation speed. The calculation is based on the use of a candidate rotation frequency in which the continuity of the frame distribution over the rotation angle is assured. By correcting this candidate rotation speed toward an equiangular distribution, an optimized rotation speed is obtained. Table 3.1 gives a number of examples of the calculation for some randomly selected clinical settings.

3.2.6 Quantification

Quantification tools are based on manual or semiautomatic tracing of an anatomical feature in a stack of 2D images. This is necessary due to the fact that currently there are no fully automatic quantification algorithms available. In addition, computers are equipped with 2D monitors that essentially can be used only to view two spatial dimensions plus time. Therefore, the recorded 4D dataset needs to be resliced in order to obtain the 2D image set required by the selected quantification tool. In the case of left ventricular (LV) volume measurement this could mean a set of long and / or short axis images.

3.3 Results

The capabilities of the FRU-transducer are illustrated in three examples: in-vitro volume measurements, harmonic imaging in combination with contrast,

Table 3.1: *Randomly selected examples of the rotation frequency calculations with heart rates from a wide range, commonly used frame rates and an intended reconstruction with 16 cardiac segments. The angular position of the first ultrasonic beam from each frame is defined as the angular position of the frame itself. The deviation then is specified as the standard deviation of the difference between the maximum resolution and the achieved inter-frame resolution. The mean difference between the maximum resolution and the achieved resolution always will be zero with a given number of frames and, therefore, is not included.*

heart rate (bpm)	f_{Frame} (Hz)	$f_{Candidate}$ (Hz)	$N_{Rotation}$ (Hz)	$f_{Rotation}$ (Hz)	**resolution** (°)	**deviation** (%)
47	98.7	6.6894	3	6.6920	8.18	6.4
51	98.7	7.2417	3	7.2402	8.78	3.2
64	93.4	5.6266	3	5.6252	7.20	4.1
73	104.8	6.4677	3	6.4644	7.35	7.0
81	104.8	5.7412	3	5.7394	6.54	4.6
89	104.8	6.2554	3	6.2572	7.20	2.9
97	106.1	5.1319	3	5.1319	5.81	2.0
104	106.1	7.4427	4	7.4427	6.32	1.8
120	93.4	6.3683	3	6.3683	8.18	1.4
142	104.8	7.6666	4	7.6634	6.55	3.5

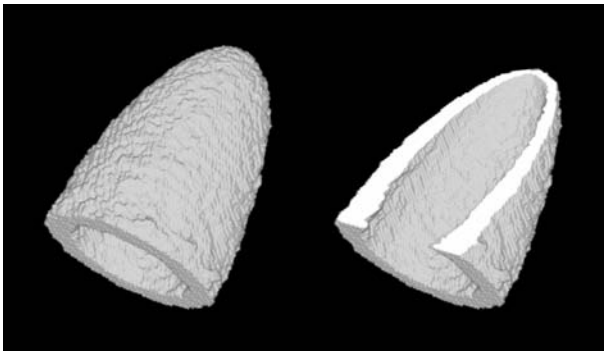

Figure 3.6: *Rendered reconstruction of the LV-shaped agar phantom.*

and a preliminary clinical study.

3.3.1 In-Vitro Evaluation

Two geometrical agar units were made with cavities in the shape of a sphere and a beam. Each unit consisted of two halves. From the units, five different phantoms were constructed: a sphere, a beam, half a sphere, half a beam and a mixed combination of half a sphere and half a beam (or 'mushroom'). Another agar phantom was made that had a LV shape.

Recordings of the phantoms were made with a rotation speed of 6 Hz (360 rpm) and a frame rate of 67.5 fps. One to two seconds of each recording were used to reconstruct the phantoms. After reconstruction, the phantom cavities were extracted with an advanced threshold-based method. For this method, depth dependent bimodal histogram thresholding, a closing procedure with a diamond structuring element of size three and volume extraction using a connectivity of six were used [Sonka 1999]. The extracted volumes were compared with the actual volume of the phantom cavity.

The result of one of the agar phantom reconstructions is depicted in figure 3.6. The reconstructions of the six different phantoms showed an average volume error of approximately 1 % (see table 3.2).

3.3.2 Contrast Harmonic Imaging

A commercially available tissue mimicking flow phantom (Model 524, ATS Laboratories, Bridgeport, Connecticut, USA) was used to explore the har-

Table 3.2: *Results of the in-vitro volume measurement evaluation.*

phantom	**volume** (ml)		**deviation** (%)
	actual	reconstructed	
sphere	135.5	136.9	1.0
beam	133	131.5	1.1
$\frac{1}{2}$ sphere	68.5	67.6	1.3
$\frac{1}{2}$ beam	63	62.5	0.7
'mushroom'	131.5	132	0.4
LV	131	128.7	1.8

monic capabilities of the FRU-transducer in combination with the use of contrast agents. Backscatter power spectra from a tissue and a contrast region of interest (ROI) were calculated from recorded radio frequency data. The spectra and the extracted contrast to tissue ratio from these spectra were used to determine the efficacy of harmonic imaging over fundamental imaging [Voormolen 2004].

The contrast to tissue ratio (CTR) was defined as the ratio of the scattered power caused by the contrast to that of the tissue. The contrast and tissue ROI were selected as shown in figure 3.7A. Optison contrast agent (Amersham Health, Princeton, NJ) was used at a dilution of 1 over 2000 in Isoton II (Beckman Coulter, Fullerton, CA) and was flowing at a constant rate of 90 ml/minute through the phantom. The ROIs were insonified with a pulse comprising a derated peak negative pressure of 150 kPa, a transmit frequency of 1.74 MHz, and a pulse length of 2.5 cycles. With these settings, an increase of more than 8 dB in the CTR was found at the second harmonic compared to the fundamental frequency (see figures 3.7B and 3.7C).

3.3.3 Clinical Recordings

Figure 3.8 shows a rendered patient recording of the left ventricle. The image shows the LV cavity, the mitral valve, and the aortic outlet tract. In addition, two reconstructed 2D images of the LV short and long axis are shown.

From another patient, the LV volume and ejection fraction was determined. Quantification of the recorded echo data was performed with 4D LV Analysis software from TomTec Imaging Systems (Unterschleißheim, Germany)

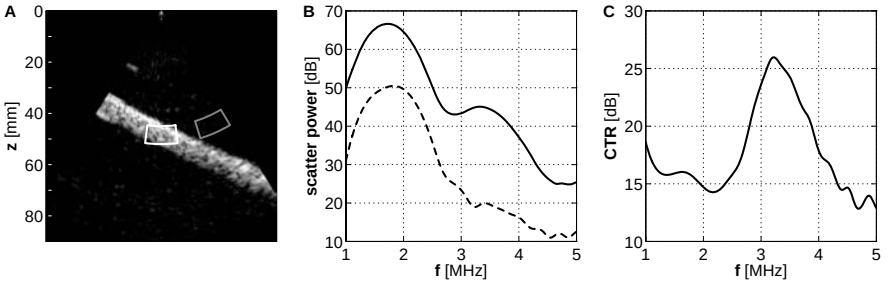

Figure 3.7: ***A.*** *A B-mode image from the tissue-mimicking phantom with contrast in the flow area is shown. The gray and white solid lines indicate the ROI used for the power spectra calculations.* ***B.*** *The power spectra obtained from the tissue (dashed line) and contrast (solid line) region at a transmission frequency of 1.74 MHz are depicted.* ***C.*** *The difference of these power spectra, defined as the CTR, is shown.*

featuring a semiautomated border detection algorithm. End diastolic and end systolic volumes were determined using seven slices per volume with equiangular intervals. Figure 3.9 shows the analysis result. An end-diastolic and end-systolic surface rendering of the endocardial border is shown along with the obtained time-volume curve. From the time-volume curve, an end diastolic volume of 131 ml, an end-systolic volume of 66 ml, and an ejection fraction of 50 % were extracted. An MRI recording of the same patient on the same day resulted in an end-diastolic volume of 131 ml, an end-systolic volume of 62 ml, and an ejection fraction of 53 %.

3.4 Discussion

A novel transducer design, based on the continuous rotation of a phased array, for rapid 3D echo has been presented. The short acquisition time, of approximately 10 seconds, makes it highly suitable for echocardiographic application and avoids the need for respiratory gating. In addition, its wide bandwidth allows for tissue and contrast harmonic imaging.

Although the need for fast 3D echocardiography has been widely recognized, only one other research group has reported on a similar concept as presented here [Canals 1999, Nguyen 2002, 2003]. Their transducer uses a fast-rotating array that is oscillating within its rotation angle range of 720°. Although its rotation speed matches that of the FRU-transducer, the oscilla-

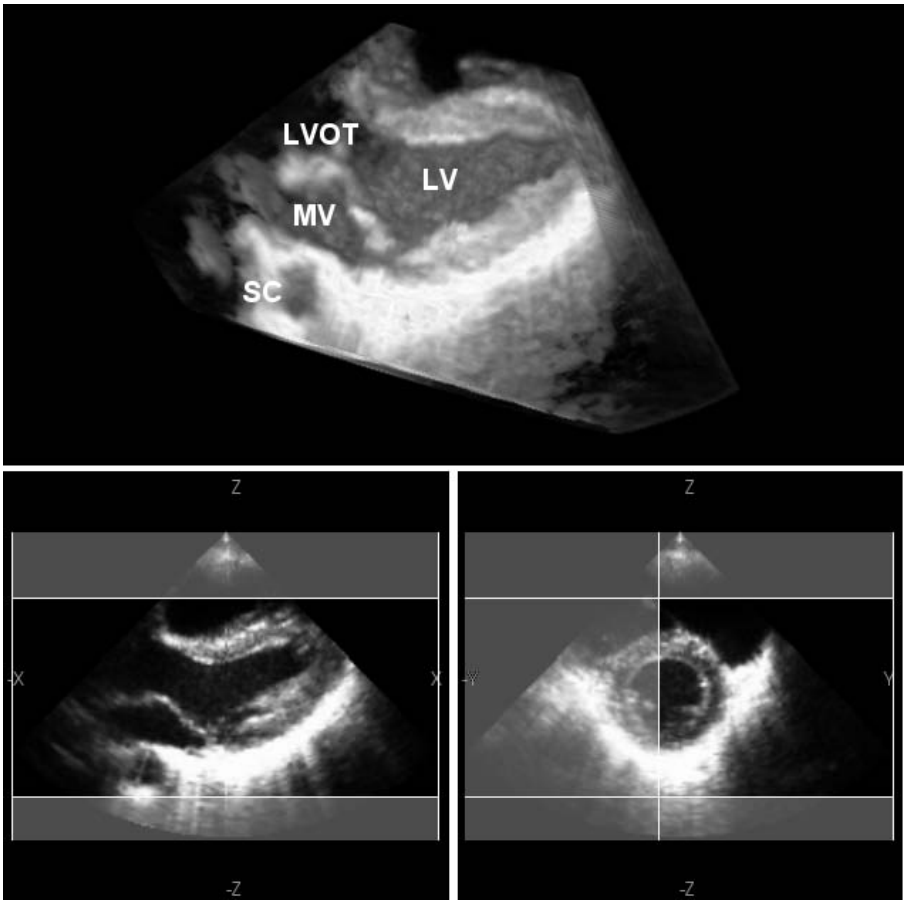

Figure 3.8: *The upper panel depicts a volume-rendered reconstruction of a left ventricular patient recording. The two lower panels show a reconstructed long and short axis image, respectively. The shaded regions in the lower panels annotate the cut away areas of the volume rendered image in the upper panel. LV: left ventricle; MV: mitral valve; LVOT: left ventricular outflow tract; SC: sinus coronaries.*

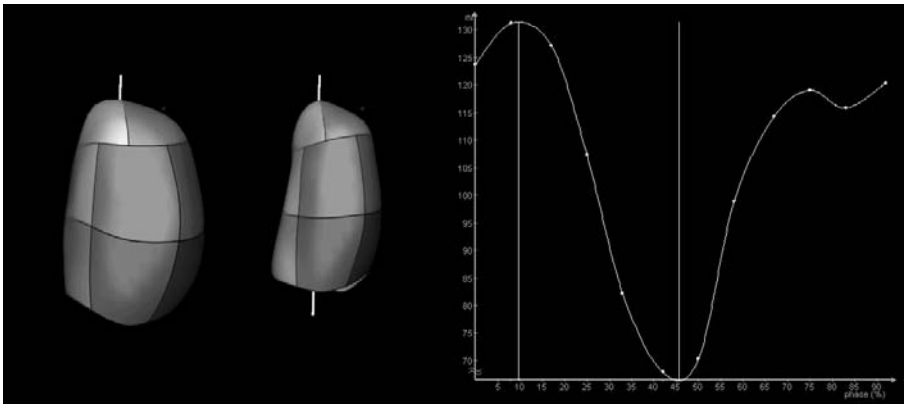

Figure 3.9: *The left panel shows an end-diastolic and end-systolic surface rendered tracing result from a patient recording. The corresponding time-volume curve is shown in the right panel. From the time-volume curve, the end-diastolic volume (131 ml), the end-systolic volume (66 ml), and the ejection fraction (50 %) are derived.*

tory motion results in an even more complex sampling of the time-volume space. Studies in which this transducer has been used have been limited to fundamental imaging, so no record exists on its harmonic imaging capabilities.

Another concept for fast 3D echocardiography is the use of matrix array transducers, which are currently available with the Philips Sonos 7500 scanner (Best, The Netherlands) and its x4 xMATRIX transducer as well as the General Electric Vivid 7 scanner (Milwaukee, Wisconsin, USA) with its 3V transducer. At the current state-of-the-art, it is very difficult for matrix transducers to both deal with the complex technology involved and also match the image quality of contemporary, phased-array transducers. Although it has been reported that second generation matrix array transducers show a big improvement of image quality compared to its predecessors [Von Bardeleben 2004, Arai 2004], this relatively young technique still provides suboptimal image quality, especially when it comes to harmonic imaging [Chan 2004, Schnabel 2005]. In addition, advanced 2D imaging techniques, such as contrast superharmonic imaging [Bouakaz 2003a], can be implemented with the FRU-transducer in a straightforward manner and extended for use in 3D applications.With the use of multibeat fusion, an acquisition with the FRU-transducer requires 10 seconds maximally. In principal, the matrix approach has the advantage of real-time acquisition and display; but in clinical practice, the field-of-view of

real-time scanning is too limited. For a so-called *full-volume recording* with the Philips scanner, the acquisition is extended to four cardiac cycles, after which the data can be viewed and analyzed offline. In this respect, there is no difference between our approach and matrix-array transducers. Ultimately, the FRU-transducer also provides a cost-effective alternative to matrix-array transducers.

Although the results show feasibility of the clinical application of the FRU-transducer, a full evaluation of its clinical capabilities will be conducted in the near future. This will include the determination of the LV function compared with other techniques such as MRI and the use of contrast agents for improved 3D assessment of the heart.

With the availability of fast 3D echocardiographic acquisition, quantification of the recorded data has become the most time-consuming element in the diagnostic use of 3D datasets. This is mainly due to the lack of tracing algorithms that do not need an expert to initialize the algorithm and review the tracing result. Improved image quality and border delineation will be a welcome contribution toward fully automatic quantification tools. The unique harmonic capabilities of the presented transducer could be beneficial for this purpose. Therefore, future efforts will be aimed at the use of tissue and contrast harmonic images from the FRU-transducer for such algorithms.

3.5 Conclusion

A continuous rotating array transducer has been presented suitable for fast acquisition of 3D datasets within a clinical setting without the use of respiratory or ECG gating. Its harmonic capabilities provide unique possibilities for tissue and contrast harmonic 3D imaging, which could be beneficial for quantification algorithms. The concept is easily integrated in state-of-the-art, 2D echo systems due to its innovative and cost-effective design.

Acknowledgments

The authors would like to thank W.J. van Alphen, L. Bekkering, and F.C. van Egmond for their significant contribution in the construction of the fast-rotating ultrasound transducer.

Part II

Basic Application: Left Ventricular Volume Quantification

Chapter 4

Rapid and Accurate Measurement of Left Ventricular Function with Semi-Automated Border Detection

Rotterdam, June 18th, 2002: *Three prototypes of the fast rotating ultrasound transducer, showing the progress in its design throughout the years.*

Measurement of left ventricular (LV) volume and function are the most common clinical referral questions to the echocardiography laboratory. A fast, practical, and accurate method would offer important advantages to obtain this important information. To validate a new practical method for rapid measurement of LV volume and function, we developed a continuous fast-rotating transducer, with second-harmonic capabilities, for three dimensional echocardiography (3DE).

Fifteen cardiac patients underwent both 3DE and magnetic resonance imaging (reference method) on the same day. 3DE image acquisition was performed during a 10 second breath-hold with a frame rate of 100 frames/second and a rotational speed of 6 rps. The individual images were postprocessed with Matlab software using multibeat data fusion. Subsequently, with these images, 12 datasets per cardiac cycle were reconstructed, each comprising seven equidistant cross-sectional images for analysis in the new TomTec 4D LV Analysis software, which uses a semi-automated border detection (ABD) algorithm. The ABD requires an average analysis time of 15 minutes per patient.

A strong correlation was found between LV end-diastolic volume (r=0.99; y=0.95x − 1.14 ml; SEE=6.5 ml), LV end-systolic volume (r=0.96; y=0.89x + 7.91 ml; SEE=7.0 ml), and LV ejection fraction (r=0.93; y=0.69x + 13.36 %; SEE=2.4 %). Inter- and intraobserver agreement for all measurements was good.

The fast-rotating transducer with new ABD software is a dedicated tool for rapid and accurate analysis of LV volume and function.

Based on:

© 2006 Blackwell Publishing. Reprinted, with permission, from: **Krenning, B.J.**, M.M. Voormolen, R.-J.M. van Geuns, W.B. Vletter, C.T. Lancée, N. de Jong, F.J. ten Cate, A.F.W. van der Steen and J.R.T.C. Roelandt. Rapid and Accurate Measurement of Left Ventricular Function with a New Second-Harmonic Fast-Rotating Transducer and Semi-Automated Border Detection. *Echocardiography*, 23(6):447–454, 2006.

4.1 Introduction

Left ventricular (LV) volumes and function have major diagnostic and prognostic importance in patients with heart disease [White 1987, Hall 1995], and are the most common referral questions to the echocardiography laboratory. A fast, practical, and accurate method is a prerequisite to obtain this important information for patient management. Three dimensional echocardiography (3DE) allows accurate calculation of LV ejection fraction (LVEF) without geometric assumptions of its shape [Siu 1993, Tanabe 1998, Nosir 1996]. Recent transducer and software developments may now allow fast acquisition and semi-automated analysis, enabling the routine clinical application of 3DE [Shiota 1999, Belohlavek 2001, Kuhl 2004].

This study was performed to assess both the feasibility and accuracy of a new, continuous, fast-rotating phased array transducer for LV volume and EF calculation using commercially available quantification software. Magnetic resonance imaging (MRI) was used as the reference method.

4.2 Materials and Methods

4.2.1 Study Patients

Seventeen male patients (mean age 52 years, range 29–74 years) with a history of myocardial infarction and various degrees of wall-motion abnormalities were included. All patients were in sinus rhythm. Two patients suffered from ischemic cardiomyopathy. None of the patients had to be excluded because of insufficient image quality. However, two patients were excluded because of incomplete visualization of the LV in the echocardiographic window due to LV dilatation. The mean heart rate (SD) during echocardiographic examination was 57 (13) bpm. Both studies were completed in each patient within 4 hours, and MRI was performed before 3DE examination. All patients gave informed consent.

4.2.2 Three Dimensional Echocardiography

Instrumentation We used a new third generation prototype transthoracic, fast-rotating 64-element array transducer with a center frequency of 3 MHz. Besides decreased transducer size and technical improvements, this transducer features the capability of second harmonic imaging (figure 4.1). The

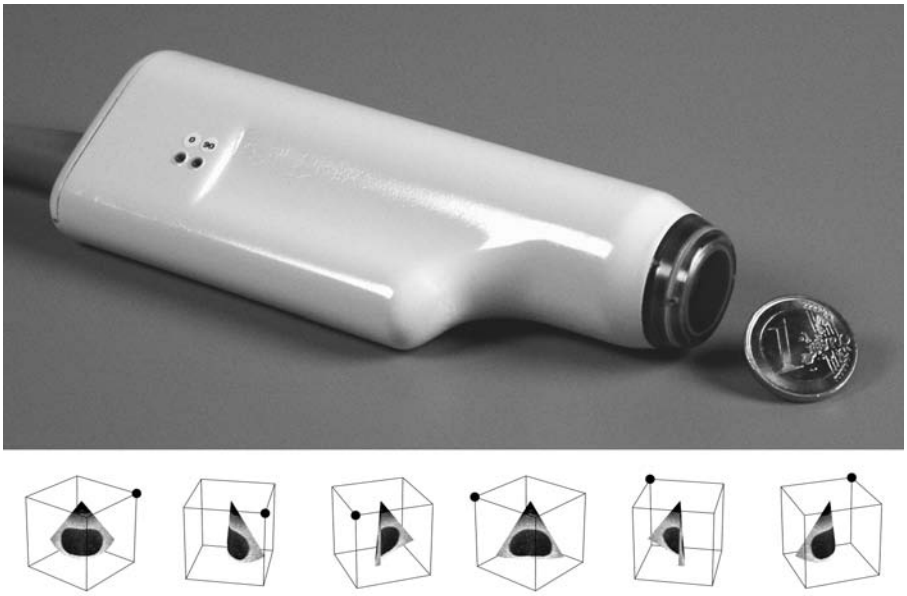

Figure 4.1: *Image of the most recent prototype of the continuous, fast-rotating transducer used in this study. Below, a 2D phantom image displayed in perspective from different angles. As shown, continuous rotation results in a curved shape of the original images.*

transducer continuously rotates around its central axis with a maximum rotation speed of 480 rpm and is connected to a commercially available ultrasound system (Vivid 5, GE VingMed Ultrasound, Horton, Norway) [Djoa 2000, Voormolen 2006]. Interfaces are present for motor control, image synchronization, and data processing. Unlike other mechanical 3D acquisition systems, which can only collect images over a limited number of rotations, this transducer acquires images over as many rotations as required [Nosir 1996, Belohlavek 2001, Kupferwasser 1997, Nguyen 2002]. A slip-ring, consisting of a static and a rotating part, maintains electrical contact between the rotating array and the static part of the transducer. Therefore, any cable twisting and subsequent need for rotation inversion is not present. Because this transducer is capable of using standard two dimensional (2D) ultrasound capabilities, a high frame rate at a wide sector angle of 90° can be chosen, which is necessary to capture the full LV in most patients. The size of the transducer is nearly the same as a standard 2D transducer. The typical frame rate for a 3D acquisition is

approximately 100 frames/second.

Image acquisition Patients are studied in the left lateral decubitus position, with the transducer in the apical position and the image plane rotating around the LV long axis. The depth settings are adjusted to visualize the entire LV and part of the left atrium. Gain and power settings are optimized for endocardial border visualization. The image acquisition is made during a single end-expiratory breath-hold of approximately 10 seconds, in second-harmonic imaging mode (transmit frequency: 2 MHz). The ECG is simultaneously recorded for the 3D reconstruction process.

Image processing and analysis Image data are transferred via a network connection to a dedicated PC for processing and analysis. With custom-designed software, based on MatLab (The MathWorks, Natick, Massachusetts, USA), the original 2D images are postprocessed (figure 4.2A). Using the ECG, the echo data are located in their correct spatial and temporal positions [Lancée 2000, Voormolen 2006]. To obtain an adequate density of the spatial and temporal sampling, multibeat data fusion is employed [Lancée 2000, Voormolen 2006]. Twelve 3D-datasets were reconstructed by dividing the cardiac cycle in 12 equidistant time-intervals, irrespective of its length. Due to the continuous rotation of the transducer-array, the original 2D imaging planes have a curved shape and are not suited for automated contour analysis with currently available software. Therefore, seven equidistant cross-sectional images are resampled from the 12 datasets and used for further contour analysis. This resulted in a rotational interval of 27° between the cross-sectional images [Voormolen 2006].

Subsequently, all resampled cross-sectional images are imported into the TomTec 4D LV Analysis software (TomTec Imaging Systems, Unterschleißheim, Germany). Their orientation in 3D space is determined by manually marking the mitral valve, aortic root and apex. An elliptical model is then placed over one of the images of each of the seven cross-sectional positions. Contrast and gain settings can be adjusted for optimal endocardial border visualization. After this, the software automatically performs endocardial border detection in all images of each cross-sectional position in the 12 datasets. A spatiotemporal spline model is used to generate smooth contours for both the temporal and the spatial domains. Two investigators verified and corrected the results from the automated border detection independently. This was done blinded to MRI results. The first investigator analyzed the 3DE images twice, blinded for the results of the first analysis.

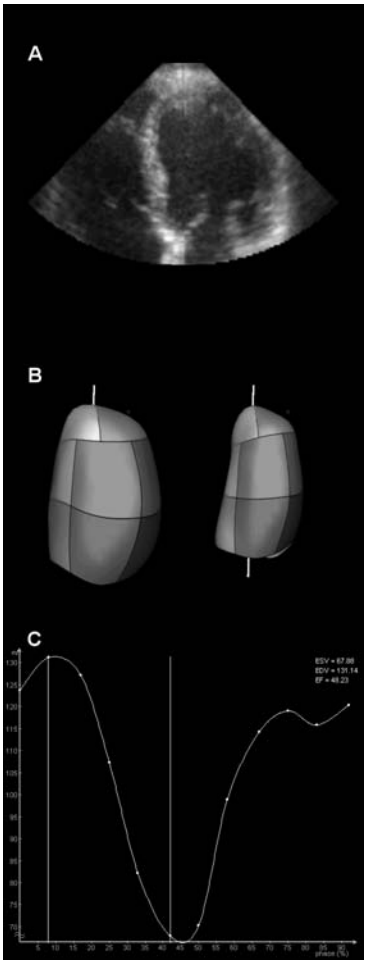

Figure 4.2: ***A.*** *An original image of the apical long-axis view showing the image quality during fast rotation.* ***B.*** *Endocardial surface rendered image of the endocardial border.* ***C.*** *Volume-time curve; dots show measured data points.*

The analysis program displays a reconstruction of the LV as a dynamic surface rendered image, in which LV wall motion is shown in three dimensions (figure 4.2B). From an automatically plotted time-volume curve (figure 4.2C), LV end-diastolic (LVEDV) and end-systolic volume (LVESV) were determined by the maximal and minimal volume, and LVEF was calculated.

4.2.3 MRI

All patients are studied in a supine position, with a four-channel quadrature body phased array coil placed over the thorax, in a 1.5 T whole-body MRI system (Signa CV/i, General Electric, Milwaukee, Wisconsin, USA; with an amplitude of 40mTm^{-1} and a slew rate of 150 Tm^{-1}s^{-1}). For quantitative analysis, approximately 10 to 12 cine short-axis series (slice thickness 8 mm, gap 2 mm) covering the heart from base to apex were acquired using a breath-hold cardiac triggered steady-state free precession sequence (FIESTA) with a TR and TE of 3.5 and 1.3 ms, respectively, and a flip angle of 45°. Additional imaging parameters were: field of view of 340×255 mm, a matrix of 160×128, and a temporal resolution of 28 ms. The whole protocol could be performed within 30 minutes.

Quantitative analysis was performed using standardized software (Mass-Plus, General Electric, Milwaukee, Wisconsin, USA). With this software, endocardial contours were semiautomatic traced on all end-diastolic and systolic images to calculate the LV volumes and EF using Simpson's rule. Review of the automated tracing was performed by an investigator, blinded to the 3DE data.

4.2.4 Statistical Analysis

Data are presented as mean (standard deviation, SD). A linear regression analysis was performed for the comparison of results obtained by 3DE and MRI. The first measurement of the first observer was used for comparison with MRI. The 3DE measurements from two independent observers were compared mutually to assess interobserver variability. To assess intraobserver variability, the two blinded measurements by the first observer were compared. In addition, the limits of agreement were calculated for all comparisons and expressed as the mean ± 2SD [Bland 1986]. To determine whether there is a statistically significant difference between the populations of each comparison, a paired t-test was performed. Data were tested for normality with the Kolmogorow-Smirnov test with Lilliefors significance correction. A probability level of $p<0.05$ was considered significant.

4.3 Results

LVEDV measurements for MRI ranged from 127 to 241 ml and from 122 to 239 ml for 3DE. LVESV measurements for MRI ranged from 58 to 144 ml and from 60 to 144 ml for 3DE. The mean (SD) for LVEDV measurements were 186 (41) ml and 177 (40) ml (p<0.001), for MRI and 3DE, respectively. The mean (SD) for LVESV measurements were 99 (28) ml and 96 (25) ml (p=NS), for MRI and 3DE, respectively. The Kolmogorow-Smirnov tests for normality were not significant, indicating a normal distribution of data. The time for data analysis averaged 15 (5) minutes per patient.

4.3.1 Comparison Between 3DE and MRI

Results of the regression analysis and the limits of agreement calculation for LVEDV, LVESV, and LVEF are shown in figure 4.3. A strong correlation was observed between MRI and 3DE for both LVEDV (r=0.99; y=0.95x − 1.14 ml; SEE=6.5 ml) and LVESV measurements (r=0.96; y=0.89x + 7.91 ml; SEE= 7.0 ml). The limits of agreement analysis demonstrated a mean difference of −9.7 ± 13.1 ml for LVEDV and −3.0 ± 14.7 ml for LVESV. A good correlation was also observed for calculated LVEF (r=0.93; y=0.69x + 13.36 %; SEE=2.4 %), with a mean difference of −1.7 ± 7.2 %.

4.3.2 Intraobserver Variability

The two independent measurements from the first observer show an excellent correlation for LVEDV (r=1.00; y=0.97x + 4.3 ml; SEE=3.2 ml), LVESV (r=1.00; y=1.00x − 0.2 ml; SEE=2.3 ml), and LVEF (r=0.99; y=1.04x − 2.4 %; SEE=1.2 %). The limits of agreement analysis demonstrated a mean difference of −1.4 ± 6.6 ml for LVEDV, −0.1 ± 4.4 ml for LVESV, and −0.3 ± 2.4 % for LVEF. No significant difference was present between the two measurements.

4.3.3 Interobserver Variability

The linear regression and limits of agreement calculation for LVEDV, LVESV, and LVEF from the 3D echocardiographic data by two independent observers are shown in figure 4.4. These results show a good correlation and only a small mean difference for LVEDV (r=0.99; y=0.98x + 3.53 ml; SEE=6.0 ml) and LVESV (r=0.99; y=1.00x + 0.97 ml; SEE=4.5 ml). The results of the linear regression analysis for LVEF were acceptable (r=0.93; y=0.91x + 3.24 %;

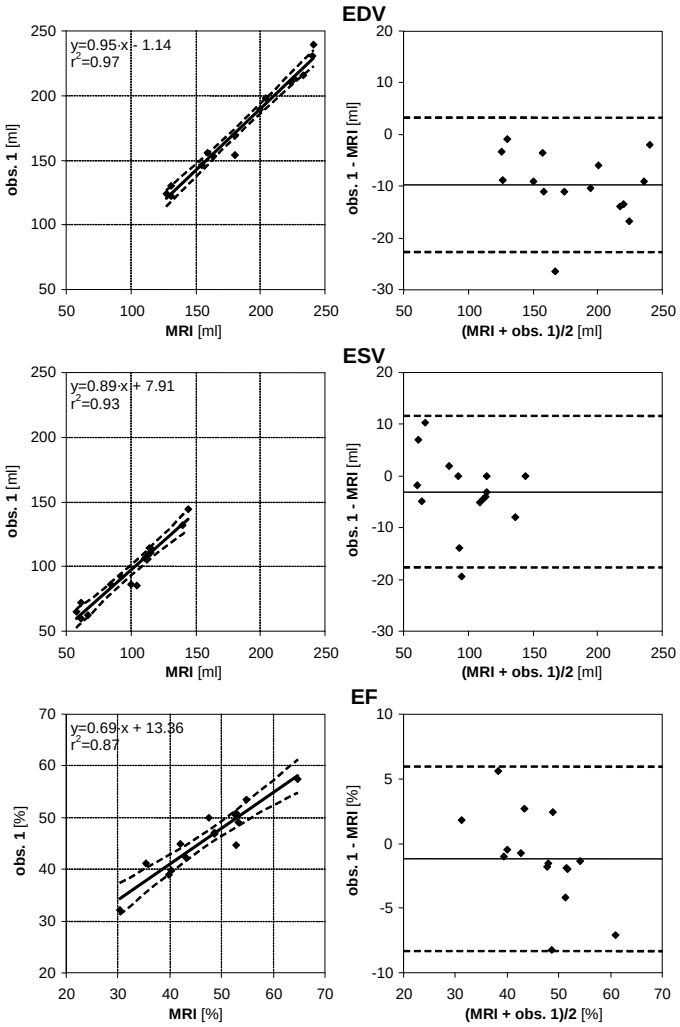

Figure 4.3: *Relation between 3DE and MRI measurements of LVEDV, LVESV, and LVEF. The left panels show the regression line between the two methods. Dashed lines delimit 95 % confidence interval. The right panels show plots of the difference between MRI and 3DE, as a function of the average calculated volumes. Solid and dashed lines represent mean ± 2SD of the difference, respectively. (LVEDV: left ventricular end-diastolic volume; LVEF: left ventricular ejection fraction; LVESV: left ventricular end-systolic volume).*

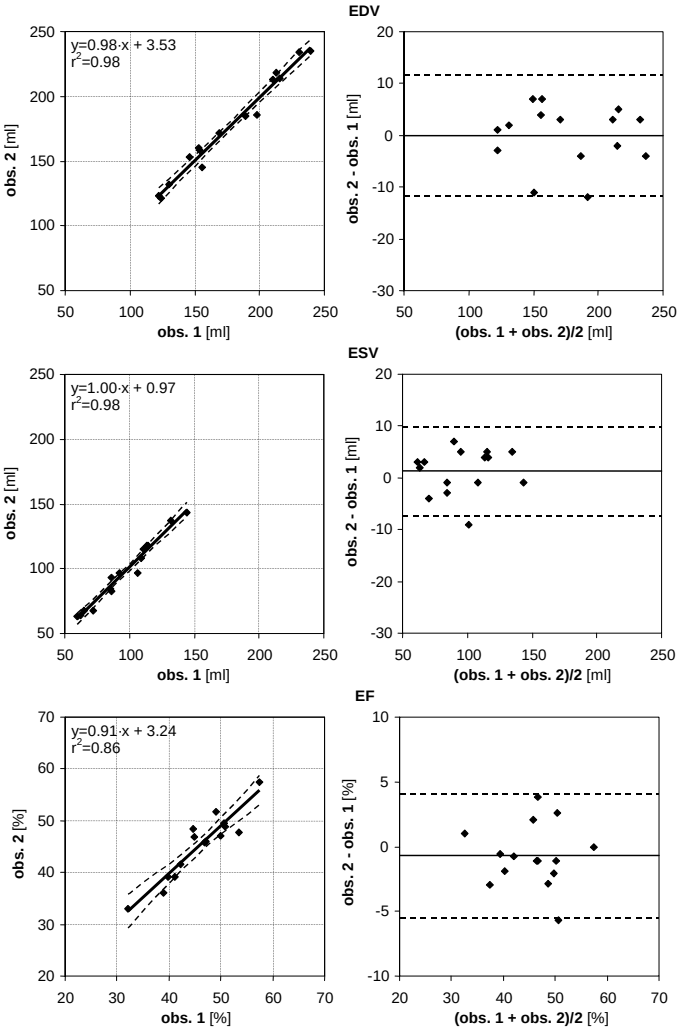

Figure 4.4: *Interobserver variability for 3DE measurements of LVEDV, LVESV, and LVEF. The left panels show the regression line between measurements obtained by two different observers. Dashed lines delimit 95 % confidence interval. The right panels show plots of the differences between both measurements by the two observers as a function of the average measurement. Solid and dashed lines represent mean ± 2SD of the differences, respectively. (LVEDV: left ventricular end-diastolic volume; LVEF: left ventricular ejection fraction; LVESV: left ventricular end-systolic volume).*

SEE=2.4 %). The limits of agreement analysis demonstrated a mean difference of −0.1 ± 11.7 ml for LVEDV, 1.3 ± 8.7 ml for LVESV, and −0.7 ± 4.8 % for LVEF. No significant difference was present between the two observers.

4.4 Discussion

This study demonstrates that 3DE, with a continuous, fast-rotating ultrasound transducer and TomTec 4D LV Analysis software, provides an accurate method for determination of LV volume and function. This technique allows the acquisition on data during 10 seconds of suspended respiration, which makes it clinically feasible. We found a strong overall correlation between MRI and 3DE in a group of patients with a wide range of LV volumes, who underwent MRI and 3DE examination on the same day. Further, analysis of inter- and intraobserver variability also showed a good correlation.

The MRI measurements for LVEDV in our study were higher than those of 3DE. However, almost all 3DE studies tend to underestimate LV volumes when compared to MRI [Krenning 2003]. One explanation for this underestimation may be a difference in tracing method. TomTec 4D LV Analysis software requires long-axis images for endocardial border detection, while the MRI software uses short-axis cross-sections with a disk-summation method to obtain an LV volume. Using the latter method, a part of the aortic root or left atrium can be included in the volume of the reconstructed disk in the most basal cross-section. This error can theoretically be reduced by increasing the number of disks (and subsequent decrease of slice thickness), resulting in an increased review time.

Second, the endocardial contour tracing may have an important influence on volume determination [Mannaerts 2003]. MRI tracings were performed excluding the trabeculae, while 3DE tracings were performed on the endocardial border, mostly including the trabeculae. During diastole, individual trabeculae are difficult to visualize due to their small size. In systole, however, the trabeculae form a compact layer, clearly distinguishable from the bloodpool. This may explain differences in LVEDV.

In this study, we used seven equidistant long-axis cross-sections for endocardial border detection, resulting in a good agreement as compared to MRI. Several studies calculated the optimal rotational interval for LV volumes mostly based on endocardial border tracing of short-axis slices of the LV or intersecting long- and short-axis images [Nosir 2000, Siu 1996]. Tanabe *et al.* [1998] showed that as few as 4–6 axial slices can accurately quantify LV volumes using a similar apical rotational technique in nonbeating canine heart

specimens with irregular shapes. Because currently available software most often uses long-axis border tracing, further studies are needed to determine the optimal rotational interval for this tracing method in normal and remodeled or asymmetric human ventricles with a low error in volume calculation. Also, the method described should be compared with available methods used in daily echocardiographic practice, such as acoustic quantification [Yvorchuk 1994, Perez 1992] and new electronic real-time (matrix) ultrasound systems [Kuhl 2004, Schmidt 1999, Qin 2000, Lee 2001, Ota 2001]. Theoretically, major advantages of our system are the availability of all conventional 2D echocardiography features (such as harmonic imaging and Doppler capabilities, and 90° sector angle imaging) and the compatibility with multiple commercially available ultrasound systems. Also, new echocardiographic techniques, such as super-harmonic imaging, may be easier to implement in our transducer [Bouakaz 2003a].

LV volume and function analysis is the most frequent referral question for echocardiography. A recent meta-analysis showed that 2DE can only provide a moderately accurate assessment of LV systolic function [McGowan 2003]. In literature, a 95 % confidence interval for LVEF<±10 % is suggested to be important in patients with borderline LV dysfunction (LVEF 30–50 %) for adequate diagnosis and risk stratification. 3DE can serve as an additional imaging technology for more accurate LVEF assessment in these patients. A routine 2D examination can then be completed with a fast 3D LV function analysis.

4.5 Conclusions

The results of this study demonstrate that the fast-rotating transducer in combination with TomTec 4D LV Analysis software provides a dedicated tool for accurate measurement of LV volume and function.

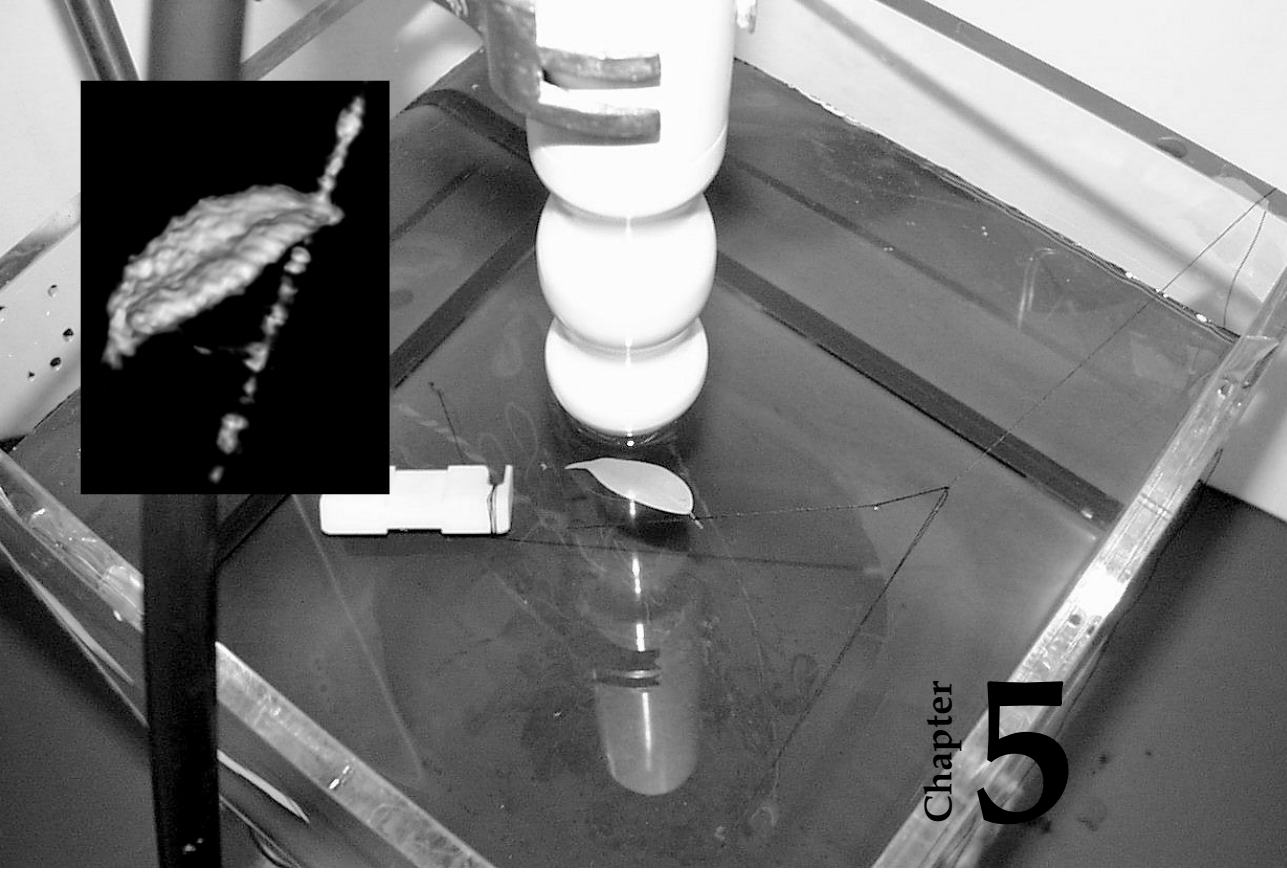

Chapter 5

Left Ventricular Volume Estimation in Cardiac Three dimensional Ultrasound: a Semiautomatic Border Detection Approach

Rotterdam, May 27th, 2002: *Setup and volume rendered reconstruction (inset) of a ficus leaf, recorded with the second prototype of the Fast Rotating Ultrasound Transducer. Successful recordings and reconstructions can be made of a wi(l)d(e) variety of bodies. It is the accurate quantification of its characteristics that poses the challenge.*

We propose a semiautomatic endocardial border detection method for three dimensional (3D) time series of cardiac ultrasound (US) data based on pattern matching and dynamic programming, operating on two-dimensional (2D) slices of the 3D plus time data, for the estimation of full cycle left ventricular volume, with minimal user interaction.

The presented method is generally applicable to 3D US data and evaluated on data acquired with the Fast Rotating Ultrasound (FRU-)Transducer, developed by Erasmus Medical Center (Rotterdam, the Netherlands), a conventional phased-array transducer, rotating at very high speed around its image axis. The detection is based on endocardial edge pattern matching using dynamic programming, which is constrained by a 3D plus time shape model. It is applied to an automatically selected subset of 2D images of the original data set, for typically 10 equidistant rotation angles and 16 cardiac phases (160 images). Initialization requires the drawing of four contours per patient manually. We evaluated this method on 14 patients against MRI end-diastole and end-systole volumes. Initialization requires the drawing of four contours per patient manually. We evaluated this method on 14 patients against MRI end-diastolic (ED) and end-systolic (ES) volumes.

The semiautomatic border detection approach shows good correlations with MRI ED / ES volumes (r=0.938) and low interobserver variability (y= 1.005x − 16.7 ml, r=0.943) over full-cycle volume estimations. It shows a high consistency in tracking the user-defined initial borders over space and time.

We show that the ease of the acquisition using the FRU-transducer and the semiautomatic endocardial border detection method together can provide a way to quickly estimate the left ventricular volume over the full cardiac cycle using little user interaction.

Based on:

© 2005 Association of University Radiologists. Reprinted, with permission, from: **Van Stralen, M.**, J.G. Bosch, M.M. Voormolen, G. van Burken, B.J. Krenning, R.-J.M. van Geuns, C.T. Lancée, N. de Jong and J.H.C. Reiber. Left Ventricular Volume Estimation in Cardiac Three-dimensional Ultrasound: A Semiautomatic Border Detection Approach. *Academic Radiology*, 12(10):1241–1249, 2005.

5.1 Introduction

For diagnosis of cardiovascular diseases, the volume and ejection fraction of the left heart chamber are important clinical parameters. Three dimensional (3D) ultrasound (US) offers good opportunities to visualize the whole left ventricle (LV) over the complete cardiac cycle. 3D US is noninvasive, relatively cheap, flexible in use, and capable of accurate volume measurements. New, fast 3D US imaging devices are entering the market and have the potential of allowing such measurements rapidly, reliably, and in a user-friendly way, provided that a suitable automated analysis is available. Manual segmentation of the large data sets is very cumbersome and suffers from inconsistencies and high variability. On the other hand, the human experts interpretation and intervention in the detection are often essential for good results. Therefore, a semiautomatic segmentation approach seems most suitable.

Some methods for segmentation of four-dimensional (4D) echocardiographic images have been published. Angelini *et al.* [2001] reported on a wavelet-based approach for 4D echocardiographic image enhancement followed by an LV segmentation using standard snakes. Corsi *et al.* [2002] presented a level-set-based semiautomatic method. Montagnat and Delingette [2000] used a two-simplex mesh and a feature detection based on a simple cylindrical gradient filter. Sanchez-Ortiz *et al.* [2000] used multiscale fuzzy clustering for a rough segmentation in two dimensional (2D) longitudinal slices. B-splines are used for 3D surface fitting in each time frame. These methods have not been validated successfully on a reasonable data set. The most practical approach is described by Schreckenberg *et al.* [1998]. It uses active surfaces that are controlled by difference-of-boxes operators applied to averages and variances of the luminance. This technique is implemented in a commercially available workstation (4D LV Analysis, TomTec Imaging Systems, Unterschleißheim, Germany). The general experience is that this technique requires much initialization and corrections and a consistent segmentation is still hard to reach. Recently, Philips presented its new online quantification tool QLAB (Philips Medical Systems, Best, The Netherlands), which can be used for semiautomatic 3D volume quantification. However, technical details or an extensive evaluation of this method has not yet been published.

We present a new semiautomatic endocardial border detection method for time series of 3D cardiac US data. Our method is based on pattern matching and dynamic programming techniques and combines continuity, robustness, and accuracy in 2D cross sections with the spatial and temporal continuity of the 4D data. It aims at optimally using a limited amount of user interaction

Figure 5.1: *Fast rotating ultrasound transducer.*

(capturing essential information on shape and edge patterns according to the users interpretation of the US data) to attain a fast, consistent, and precise segmentation of the LV. The presented method is general and suitable for any apically acquired 3D set.

5.2 Materials and Methods

5.2.1 Fast Rotating Ultrasound Transducer

We performed this study on a special type of image data acquired with a new device: the Fast Rotating Ultrasound (FRU-)Transducer (figure 5.1). The transducer has been developed by the Department of Experimental Echocardiography of the Erasmus MC, the Netherlands [Djoa 2000, Voormolen 2006]. It contains a linear phased-array transducer that is continuously rotated around its image axis at very high speed, up to 480 rotations per minute (rpm), while acquiring 2D images. A typical data set is generated during 10 seconds at 360 rpm and 100 frames per second (fps). The images of the LV are acquired from an apical position, with the transducers rotation axis more or less aligned with the LV long axis. The analysis assumes that the rotation axis lies within the LV lumen and inside the mitral ring.

An important advantage of this transducer is that it can be used with

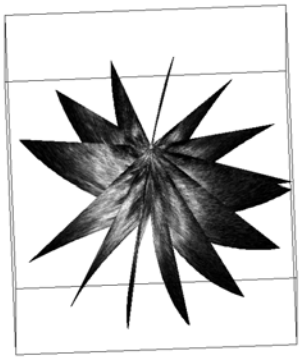

Figure 5.2: *A sequence of seven consecutive FRU images with curved image planes.*

any US machine, because a conventional phased-array transducer is used. It also acquires relatively high-quality 2D images, compared with matrix-array transducers used for real-time 3D. Further, no ECG triggering is applied, just an ECG registration for offline analysis, which allows very quick acquisitions.

As a consequence of the very high continuous rotation speed, the images have a curved image plane (figure 5.2). During the acquisition, the probe rotates about 22° per image with the typical settings given above. The combination of these curved image planes, and the fact that the acquisition is not triggered by or synchronized to the ECG signal, results in an irregular distribution over the 3D+t space (three spatial dimensions and time). Therefore, a single cardiac cycle in general is not sufficient for adequate coverage of the whole 3D+t space and multiple consecutive heart cycles are merged. The cardiac phase for each image is computed offline using detected R-peaks in the ECG [Engelse 1979]. The total set of 2D images, each with cardiac phase and rotation angle information, can be used for selection of a subset of images with a regular coverage of the 3D+t space and / or for the generation of a 4D voxel set. We perform analysis on the prior.

5.2.2 Frame Selection

To achieve adequate coverage of the whole 3D+t space and a convenient representation of the data for the user, multiple consecutive cardiac cycles are merged and an optimal subset of the total set of images is selected (figure 5.3). This subset is an optimal selection of the images on a chosen set of equidistant rotation angles and cardiac phases, minimizing the total deviation in rotation angle and cardiac phase. Typically a fixed number of 16 cardiac phases and 10 rotation angles is chosen. For each combination of a chosen cardiac phase

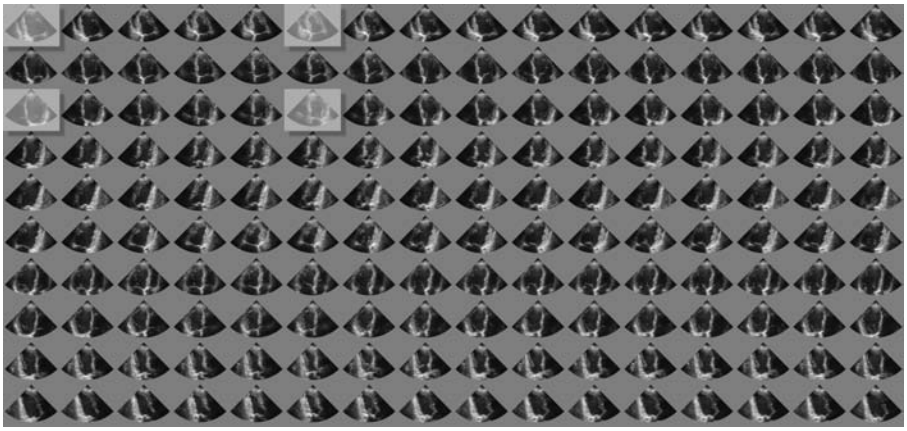

Figure 5.3: *Selected subsets of 2D FRU images in 16 cardiac phases and 10 rotation angles. Contours are manually drawn in the highlighted images, at two-chamber (2C) and four-chamber (4C) views.*

and rotation angle, the best fitting image should be selected. Moreover, the variation in acquisition time of the entire subset is minimized to limit possible motion artifacts that may have occurred during acquisition. A cost function is defined that represents the mismatch of a certain image to the targeted rotation angle and cardiac phase, also regarding the image acquisition time. Minimization of this cost function over all possible subsets results in the optimal selection and is achieved in an iterative process since costs regarding the image acquisition time depend on the average acquisition time of the current subset: changing the subset results in a new cost function that may result in a new subset again. For a more detailed description of this selection process, we refer to Van Stralen *et al.* [2004].

5.2.3 Border Detection Approach

We base our method on the knowledge that the edge patterns of the endocardial border can be complex, very different from patient to patient and even between regions within an image set. The border position need not correspond to a strong edge and may be only definable from 'circumstantial evidence' as identified by an expert observer. Rather than applying artificial, idealized edge models or templates derived from a large training set, we propose a tracking approach based on edge templates extracted from the

user-defined initial borders in the patients own images.

The method is based on these continuity assumptions (in order of strength):

1. Border continuity in separate 2D slices of the LV;

2. Spatial continuity of shape and gray value edge patterns over the LV surface in 3D;

3. Temporal and cyclic motion continuity of the endocardium.

For the FRU-transducer, within the original 2D images, both spatial and temporal distances between neighboring samples are smaller than toward adjacent images in angle and phase; therefore, border continuity is supposed to be strongest here.

The method is initialized from four manually drawn contours, taken from two roughly perpendicular views (more or less corresponding to two- and four-chamber cross sections) in two phases: end-diastole (ED) and end-systole (ES). These are used to initialize a model for the edge patterns near the 3D LV surface over time and a 3D shape model of the LV endocardial surface over the entire heart cycle. Both models are inherently 4D and can be polled at any spatial position and phase.

The actual border detection takes place in individual 2D images from the selected subset and is an extension of an approach for 2D+t sequences earlier developed by Bosch *et al.* [1998]. For each image in the selected subset, an estimation of the border shape is derived by intersecting the 3D shape model at the desired cardiac phase, with the (curved) image plane with the desired rotation angle.

The edge templates are also interpolated for the desired phase and angle. In the 2D image, a neighborhood of the estimated shape is resampled along lines perpendicular to the shape estimate. Using a template matching with the local edge templates, the similarity of each candidate edge point to the template is calculated. Dynamic programming is applied to find an optimal continuous border within the restrictions posed by the 3D model. In this way, the 4D surface and edge pattern models guard the (looser) spatial and temporal consistency of the detection, while the dynamic programming approach supplies a continuous and optimal detection locally. The set of detected contours describes the 3D endocardial surface over the whole cardiac cycle from which LV volumes, ejection fraction, etc. can be computed.

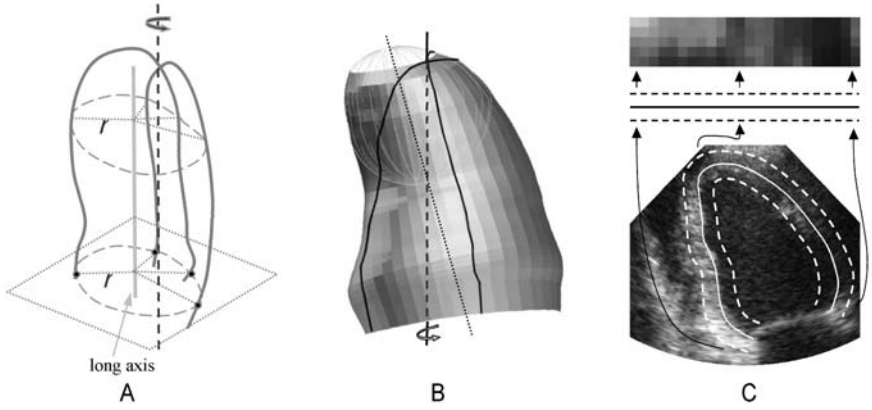

Figure 5.4: ***A***. *The interpolation of the endocardial surface in a cylindrical coordinate system oriented around the LV long axis (LAX).* ***B***. *3D surface model. The LAX estimate (dotted) and the rotation axis (dashed) are shown, together with the reconstruction of the apex by spline interpolation (light gray) from two manually drawn contours (solid black).* ***C***. *The extraction of a stylized edge pattern from the image.*

5.2.4 3D Shape Models

As said, for two cardiac phases (ED and ES), a 3D surface model of the LV endocardium is constructed from two almost perpendicular contours. During the acquisition, the rotation axis is more or less aligned with the long axis of the LV, but in practice there may be a considerable mismatch (figure 5.4B). This implies that the two image planes do not contain the true apex of the heart, and estimating the position and shape of the true apex (and the LV long axis) is a nontrivial issue. The local long axes in the 2D manually drawn contours are defined as the lines between the midpoint of the mitral valve (MV) and the 2D apex. We estimate the 3D long axis from the local long axes by computing the intersection of the planes perpendicular to these images through the local long axis in the image.

The endocardial surface is estimated by expressing the two contours in a cylindrical coordinate system with respect to the estimated LV long axis, set up by the radial component r, which represents the distance to the long axis, and the angle a, which represents the rotation around the long axis. The endocardial surface is interpolated within this system by applying a Kochanek spline interpolation [Kochanek 1984] of the radial component over the angle in planes perpendicular to the long axis (short axis planes). This interpolation

provides a natural approximation of the ellipsoidal shape of the LV within these short axis planes.

Because the initial two image planes in ED or ES generally do not intersect the real apex, the apical cap of the endocardial surface cannot be estimated simply from the two manually drawn contours within the short axis planes, as shown in figure 5.4B. Therefore, near the 3D apex we use a spherical coordinate system oriented around the LV long axis, centered at three-fourths of its length. The surface is estimated by a Kochanek spline interpolation of the radial component over the elevation angle for multiple rotation angles.

A contour estimate for any image at a given rotation angle and cardiac phase can be made by intersecting its curved image plane with the 3D contour models in ED and ES and then linearly interpolating between the two resulting '2D' contours over cardiac phase to obtain the contour estimate at the desired cardiac phase.

5.2.5 Edge Pattern Model

The desired edges are tracked over space and time by applying a pattern-matching approach with edge templates. These edge patterns are derived from the manually drawn contours and interpolated over the (phase, angle) space.

The image is resampled clockwise along the manually drawn contour, on line segments perpendicular to this contour from the inside out. The gray values on these line segments are smoothed and subsampled to form a stylized edge pattern for this contour (figure 5.4C). A typical edge pattern for a single 2D frame is represented by 32 positions along the contour and 5 samples around each edge position.

A linear interpolation over cardiac phase is performed between the edge patterns in ED and ES. The interpolation over rotation angle is less straightforward. Because the character of the edge pattern is strongly related to the angle between the endocardial border and the US beam and the distance from the transducer, the pattern changes considerably over the rotation angle, especially when the angle between the rotation axis and LV long axis is substantial. For images with rotation angles opposite ($\approx 180^\circ$) to those with the manually drawn contours, the image appears nearly mirrored and the mirrored (anti-clockwise) edge pattern is used. For angles in between, the edge patterns are linearly interpolated.

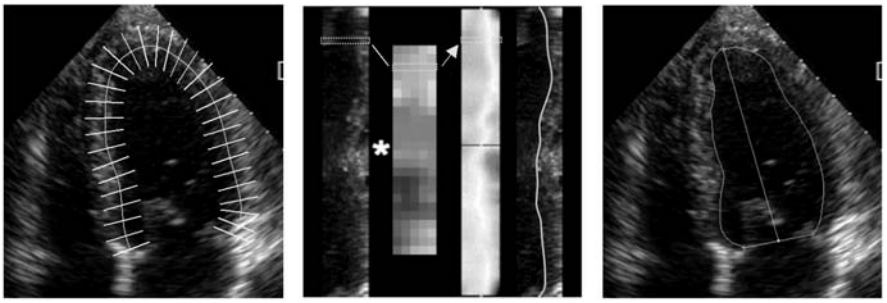

Figure 5.5: *Contour detection. Left, resampling of the image around the 2D shape estimate. Center, edge pattern matching and dynamic programming to detect the optimal contour. Right, detected contour.*

5.2.6 Contour Detection

With an estimated edge pattern and contour shape for each image in the selected subset, we can now detect the individual endocardial borders. In a neighborhood of the initial contour, the image is resampled into an array of candidate edge points, by sampling points along scan lines perpendicular to the contour shape (figure 5.5, left). From the estimated edge pattern for the image, an edge template for each scan line is extracted. For all nodes in the array (all candidate edge positions), the sum of absolute differences with its respective edge template defines the cost of the node. We now use a dynamic programming approach [Sonka 1999] to find the optimal connective path through the array of costs (figure 5.5, center). A connective path contains exactly one node per line, and the positions on consecutive lines cannot differ more than a predefined sidestep size. Dynamic programming is a well-known technique that finds the optimal path (the path with the lowest sum of costs) out of all possible connective paths in an effective manner by calculating lowest cumulative costs for consecutive layers (lines) while keeping track of the partial optimal paths. Backtracking from the node with lowest cumulative cost in the last layer provides the overall optimal path. Contour smoothness constraints are enforced by applying additional costs for sidestepping during cumulative cost calculation. To limit the influence of lines with relatively poor image information, this additional penalty is calculated per line from the statistics of node costs per line with respect to overall cost statistics, such that relatively unreliable lines get higher penalties for sidestepping.

For each phase, the detected contours of all angles together constitute a 3D

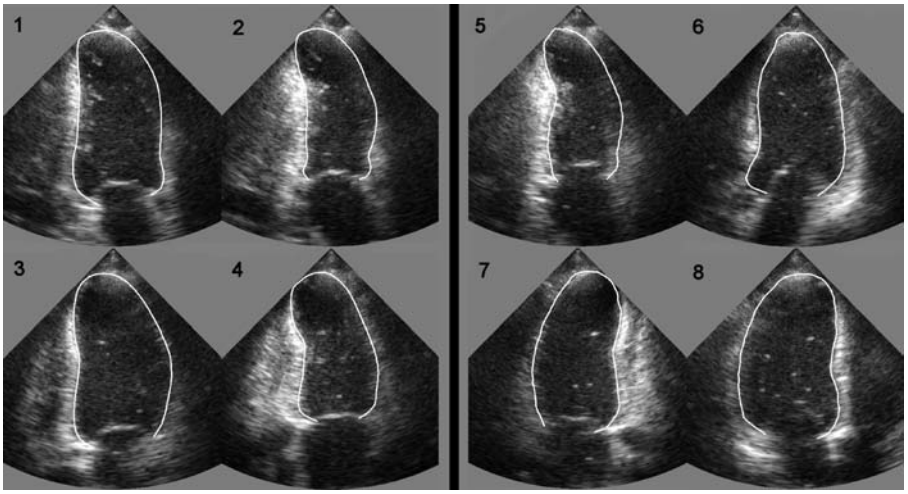

Figure 5.6: *Detection examples: frames at different (phase No., angle No.) with contours. Left, four frames with manual contours, respectively 1: ED 2C (1, 1), 2: ES 2C (6, 1), 3: ED 4C (1, 3), 4: ES 4C (6, 3). Right, four frames with detected contours, respectively 5: (8, 2), 6: (14, 5), 7: (4, 8), 8: (14, 9).*

mesh that describes the endocardial surface. We observe the volume of the LV over the whole cardiac cycle, by calculating the volumes inside the surface meshes of all selected cardiac phases.

5.2.7 Evaluation

We performed a validation study for this detection method on a group of 14 patients (age, 56 ± 14 years) with different diagnoses of cardiovascular disease, mostly myocardial infarction but also cardiomyopathy and apical aneurysm (table 5.1). A transthoracic apical scan was acquired for each patient using the FRU-transducer, which was connected to a commercially available US system (Vivid FiVe, GE VingMed Ultrasound, Horten, Norway). Short axis MRI images (Signa CV/i 1.5 T; GE Healthcare; Milwaukee, WI) were obtained using a breath-hold cardiac-triggered steady-state free precession sequence (FIESTA). US and MRI images were acquired on the same day. MRI ED and ES volumes of these patients were calculated offline by automated tracing with manual corrections in short-axis images using MASS (Medis Medical Imaging Systems, Leiden, The Netherlands), independent of the US study.

Table 5.1: *Evaluation.*

	ED volume (ml)		**ES volume** (ml)		**N**	**correlation**	**regression**
	average	SD	average	SD			
MRI	209	67	133	69	28	0.938	0.762x + 30.4
US	194	57	127	50			
obs. 1	203	56	133	48	224	0.949	1.013x − 17.4
obs. 2	187	63	119	52			

Two observers independently performed the US analysis semiautomatically using the presented method. For all patients, subsets of images were created with P=16 phases and A=10 angles. After establishing equivalent tracing conventions, the observers individually analyzed all subsets. Reading and converting the data and the automated selection of the subset took 7 minutes per patient on average. After the drawing of the four contours, the fully automated detection of the other 156 contours took approximately 90 seconds per patient. No contour corrections were allowed afterwards. Some examples of manual and detected contours are shown in figure 5.6. From the analyses of both observers, interobserver variabilities of ED / ES volumes, ejection fraction, and all other volumes were determined, as well as averages that were correlated to MRI ED and ES volumes.

5.3 Results

Results of 3D US (average of the two observers) versus MRI are shown in table 5.1 and figure 5.7 (left). These show the ED and ES volumes and the corresponding correlation coefficients and regression equations. A Bland-Altman plot [Bland 1986] of this comparison is shown in figure 5.7 (right). A relative overestimation of small volumes is shown, as well as an underestimation of the larger volumes. This could be due to the tracing conventions we applied to the echocardiographic data, which might be suboptimal for comparison to MRI data.

A high correlation of r=0.938 was found between MRI and US volumes. Overall, the MRI volumes were slightly higher. This has been reported in many studies [Iwase 1997, Buck 1997, Altmann 1997] and can be attributed to the different tracing conventions (see Discussion). The differences be-

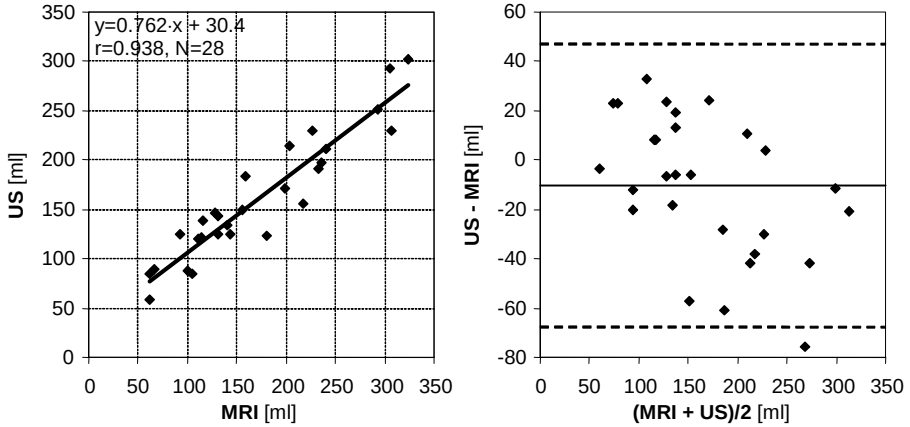

Figure 5.7: *Left, ED/ES volumes US versus MRI. Right, Bland-Altman plot of the difference in LV volume between the average US observer and MRI in ml.*

tween MRI and US volumes were not significant (paired t-test, p=0.068). Ejection fraction results showed a reasonable difference of 3.3 ± 8.6 % (regression y=0.493x + 16.6 %, r=0.755).

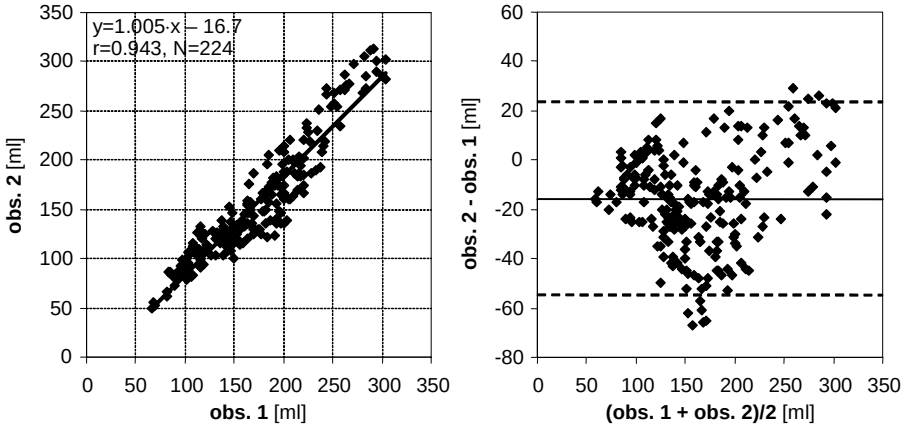

Figure 5.8: *Left, interobserver variability of full-cycle volumes. Right*[1]*, Bland-Altman plot of the difference in LV volume between the observers in ml.*

For the interobserver variability, results are presented in table 5.1 (ED and ES) and figure 5.8 (right) (full-cycle). For ED and ES volumes only, the differences were 15.0 ± 21.0 ml (average ± SD) with a regression of y=1.013x − 17.4 ml (r=0.949). We found similar differences of 15.6 ± 19.3 ml over all other phases (y=1.005x − 16.7 ml; r=0.943). This difference (ED / ES versus other phases) was not significant (unpaired t-test, p=0.628). This implies that the detection does not introduce additional variability / errors with respect to interobserver differences from the manual contours.

Absolute differences in volumes may seem high, but this is partially due to the dilated hearts in the set and the consequent high average volumes (average MRI ED=209 ml). The systematic differences in tracing between observers were equally reflected in the detected contours, which is encouraging.

5.4 Discussion

5.4.1 Manual Corrections

The method is suitable for effective correction of the detected contours in 2D images other than the initial four, although this was not yet used or evaluated in this study. A corrected contour will be treated as an additional

[1]Not included in the original publication.

manual contour and both the edge patterns and shape models will be updated accordingly, achieving a more specific approximation of the actual shape and appearance. This results in a new set of shape and edge pattern estimates, and all remaining images are redetected. In this manner, corrections will cumulatively lead to a superior global solution.

It is expected that this will further improve the results, although requiring just little interaction; similar improvements were found with the methods predecessor for the 2D+t analyses.

5.4.2 Initialization

The method is initialized by drawing four contours manually: two- and four-chamber views in ED and ES. This method is based on a tracking principle. It analyzes the expert's manual input to find corresponding endocardial positions over the full cardiac cycle in 3D. Consequently, if the expert supplies different initial contours, this will result in modified shape and edge pattern models and detections, resulting in different full-cycle volumes. These differences in the resulting volumes will therefore be proportional to the changes in the initial contours.

In the frame selection, shape and edge pattern modeling, and the contour detection, no additional, patient-specific parameters need to be set.

5.4.3 Mitral Valve Tracking

The movement of the mitral valve over the cardiac cycle is not actually detected and assumed to be linear in systole and diastole, although it is generally known that this movement is highly nonlinear, especially in diastole. A major improvement in the analysis of full-cycle volumes could therefore be made using a mitral valve tracking algorithm, for which several approaches are known.

5.4.4 Validation

The feasibility of measuring LV volumes using 3D US has been extensively shown [Nosir 1999, Jenkins 2004]. This justifies the development of automated detection methods for LV volume estimation. For the validation of such a method, comparison with manually traced contours may be desired. However, manual 3D US endocardial tracings are highly time consuming and, moreover, suffer from inconsistency and subjectivity.

Therefore, we chose to use volumes from manual MRI tracings as a golden standard in our study. Despite the fact that MRI in general acquires at a higher image quality, comparison of short axis MRI to long axis 3D US also has its drawbacks. It is a comparison of different modalities. In MRI, a high contrast between blood and tissue is imaged, which highlights the blood between the trabeculae. The outer endocardial contour therefore appears more pronounced in MRI than in 3D US, where the inner edge of the trabeculae is the strongest feature. In ES, the difference is minimal because the blood between the trabeculae is squeezed out. This may result in larger volumes compared with 3D US [Mannaerts 2003], especially in ED. Another issue in the comparison to MRI is the difference of the views in which was traced, namely apical long axis for 3D US versus short axis for MRI. This may lead to different interpretations.

5.5 Conclusions

We presented a new semiautomatic endocardial border detection method for 4D US data. This method offers fast and reasonably precise automated border detection with minimal user interaction and very promising results. However, one should bear in mind that this analysis is only preliminary. Methods have not yet been optimized and small flaws still exist. In some cases, phase information was inexact, hampering the model interpolations.

It is expected that an expansion of this method with the possibility to apply corrections and a potential extension with a mitral valve tracking algorithm (see Discussion) will further improve the results.

Despite the fact that this method is optimized for data of the FRU-transducer, the algorithm can be easily adapted to data of other image acquisition systems, for example, 4D voxel sets. The detection will then be performed in 2D slices through the LV long axis (figure 5.5).

Chapter 6

Efficient Quantification of the Left Ventricular Volume Using Three Dimensional Echocardiography: The Minimal Number of Equiangular Long-axis Images for Accurate Quantification of the Left Ventricular Volume

Rotterdam, June 20th, 2004: *A room with a view. The view from my desk over the south of Rotterdam, with Het Park, the Nieuwe Maas and the Maashaven at the foreground.*

For quantification of the left ventricular volume from three dimensional echocardiograms a number of cross-sectional images are used. The goal of this study was to determine the minimum number of long-axis images necessary for accurate quantification of the left ventricular volume.

A strong correlation was observed between volumes obtained from magnetic resonance imaging and three dimensional echocardiography using 16 equiangular images (r=0.99; y=0.95x + 3.3 ml; standard error of the estimate=7.0 ml; N=30). Comparison of these results with random subsets showed a significant difference for volumes obtained with 4 and 2 equiangular images (p<0.005). However, when the subsets were selected to target the eccentric region of the endocardial border this was only the case for subsets of two images (p<0.001).

This study demonstrates that accurate left ventricular volume quantification can be performed with as little as 8 equiangular long-axis images. By selecting the correctly oriented image set, this number can even be brought down to 4, which will further reduce the analysis time.

Based on:

© 2007 American Society of Echocardiography. Reprinted, with permission, from: **Voormolen, M.M.**, B.J. Krenning, R.-J.M. van Geuns, J. Borsboom, C.T. Lancée, F.J. ten Cate, J.R.T.C. Roelandt, A.F.W. van der Steen and N. de Jong. Efficient Quantification of the Left Ventricular Volume Using 3-Dimensional Echocardiography: The Minimal Number of Equiangular Long-axis Images for Accurate Quantification of the Left Ventricular Volume. *Journal of The American Society of Echocardiography*, 20(4):373–380, 2007.

6.1 Introduction

The advantages and usefulness of three dimensional (3D) echocardiography (3DE) have been demonstrated in numerous studies[Pandian 1994, Roelandt 2000, Belohlavek 1993, Spicer 2000, Salustri 1995]. However, 3DE requires fast acquisition and processing to become accepted as a practical clinical tool. Both the fast rotating ultrasound transducer and the recently introduced second-generation matrix transducers allow rapid acquisition [Voormolen 2006, Von Bardeleben 2004]. However, quantification of the left ventricular (LV) volume and function is still time-consuming, even with the availability of advanced semiautomatic analytic software.

Measurement of the LV volume has major diagnostic and prognostic importance [White 1987, Hall 1995]. However, LV volume is currently quantified by tracing the endocardial border in a number of cross-sectional images, preferably long-axis images [Rusk 2000]. To limit the analysis time the number of images to analyze should be minimized. Several groups are also working on fully automatic quantification but this remains complex [Sanchez-Ortiz 2002, Bosch 2002, Van Stralen 2005, Zagrodsky 2005]. Therefore, the objective of this study was to determine the minimal number of long-axis images to be used for accurate quantification of the LV volume.

6.2 Method

6.2.1 Patient Population

After informed consent, 16 men (mean age 55 ± 13 years; range 30–74 years) with a history of myocardial infarction and various degrees of wall-motion abnormalities, underwent both a magnetic resonance imaging (MRI) and 3DE examination. Two patients had dilated ischemic cardiomyopathy. One of these patients was excluded from the analysis because of incomplete visualization of the LV caused by a large apical aneurysm. The MRI examination was performed before the 3DE examination and both studies were completed within 4 hours to ensure comparable hemodynamic conditions. All patients were in sinus rhythm (mean heart rate 58 ± 13 bpm, range 41–87 bpm).

6.2.2 Echocardiographic Image Acquisition

The 3DE examinations were carried out with the fast rotating ultrasound transducer (figure 6.1) [Voormolen 2006, Djoa 2000]. It holds a continuously

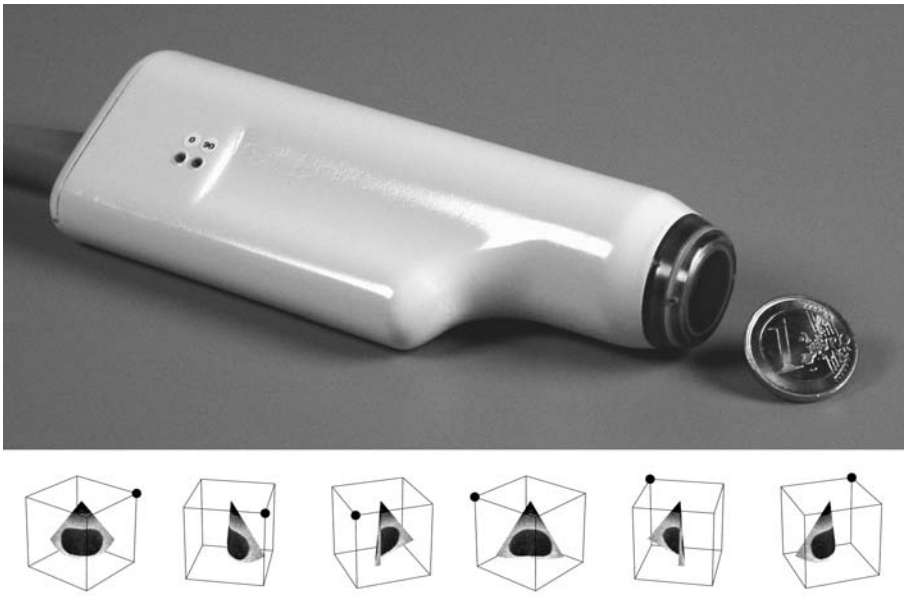

Figure 6.1: *Picture of latest prototype of fast rotation ultrasound transducer. Bottom, Original harmonic B-mode image from bladder phantom recording, in perspective. From sequence, in which two dimensional image is viewed from different angles, it can be clearly appreciated that continuous rotation of transducer results in curved shape of recorded images.*

rotating 64-element phased array that was custom made (Delft Instruments, Delft, The Netherlands). The array rotates at a speed between 240 and 480 rpm, which can be manually set. The transducer, which has a fractional bandwidth of 86 % with a center frequency of 3.2 MHz, is connected to a system (Vivid 5, GE VingMed Ultrasound, Horten, Norway). The acquisition time is approximately 10 seconds.

Patients were studied in the left lateral decubitus position with the transducer in the apical position and the image axis aligned with the LV long axis. The image acquisition included several cardiac cycles during a single end-expiratory breath hold and was made in second harmonic mode with a transmit frequency of 2 MHz, reception set for 4 MHz, a frame rate of 100 frames/second, and a rotation speed of 360 rpm.

6.2.3 Processing and Analysis of the Echocardiographic Data

The recorded two dimensional (2D) images cannot be directly processed by the quantification software because of their curved shape, resulting from the continuous rotation of the transducer (figure 6.1). Therefore, a time series of 3D data sets is reconstructed from the 2D images using the simultaneously recorded electrocardiogram and the applied rotation speed as a reference. To obtain an adequate spatial sampling density in each 3D data set, images from multiple cardiac cycles were used for the reconstruction [Voormolen 2006]. Each cardiac cycle was divided into 12 equal time intervals and the images from corresponding intervals were used to reconstruct 12 time-sequential 3D data sets. For quantification, the 3D data sets were then resliced into 16 plane long-axis images at equiangular intervals of 11.25 degrees randomly oriented around the imaging axis.

Semiautomated contour detection of the resliced images was performed with analysis software (4D LV Analysis, TomTec Imaging Systems, Unterschleißheim, Germany). These contours were used to construct a dynamic surface-rendered LV volume and to calculate a time-volume curve (figure 6.2). From the 12 traced time-sequential LV volumes, only the results from the volumes at the end-diastolic and end-systolic moment were used. Subsequently, the number of equiangular long-axis images was varied from 16 to 8, 4, and 2 images, to find the minimal number of images for accurate LV volume measurement. As pointed out by Takemoto *et al.* [2003] in a biplane study, it is beneficial for the quantification to target the eccentric region of the endocardial border with an image used for analysis. To test this effect, both random and selected equiangular long-axis image sets were investigated (figure 6.3[1]). Selection of the selected subsets was based on the most eccentric point on the endocardial border. For illustrative purposes the LV end-diastolic and end-systolic volumes were also determined using the standard 2D methods: the single plane area length method and the disk summation method [Schiller 1989].

6.2.4 MRI

Acquisition, Processing, and Analysis All patients were studied in a whole body MRI system (Signa CV/i 1.5 T, General Electric, Milwaukee, Wisconsin, USA) with an amplitude of $40\mathrm{mTm}^{-1}$ and a slew rate of $150\mathrm{Tm}^{-1}\mathrm{s}^{-1}$. The patients were in a supine position and a 4-channel quadrature body phased-array coil was placed over the thorax. For quantification, approximately 10

[1]Not included in the original publication.

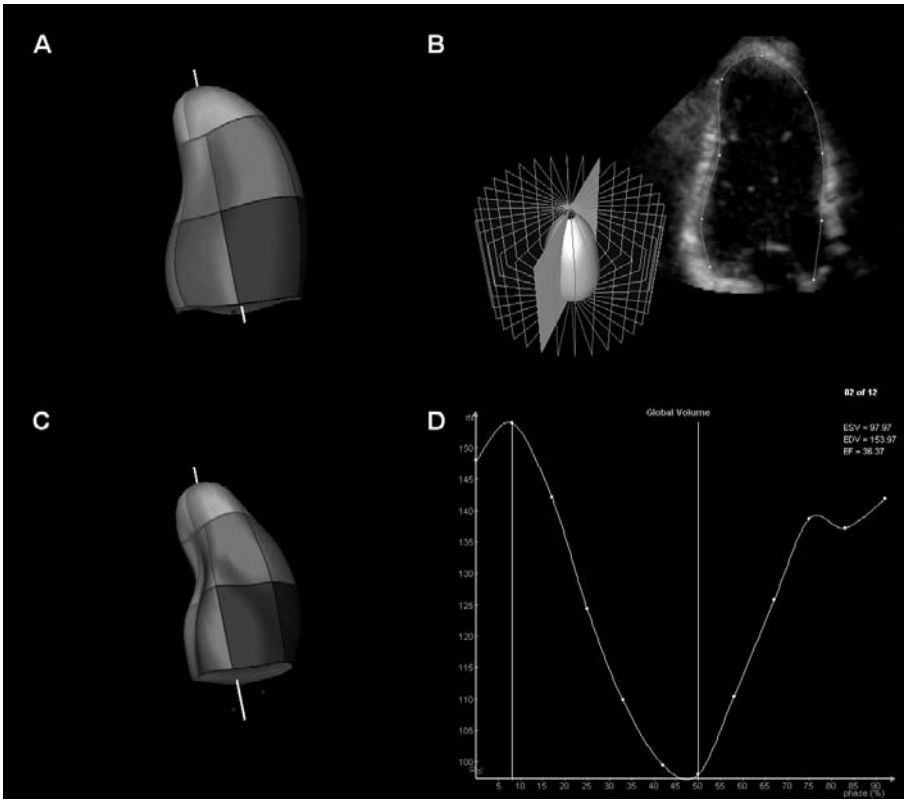

Figure 6.2: ***B***. *Resliced image with traced contour and its position in respect to the LV (grey plane).* ***A*** *and* ***C***. *Resulting surface-rendered end-diastolic volume (EDV) and end-stystolic volume (ESV).* ***D***. *Corresponding time-volume curve. From the time-volume curve, EDV and ESV are derived.*

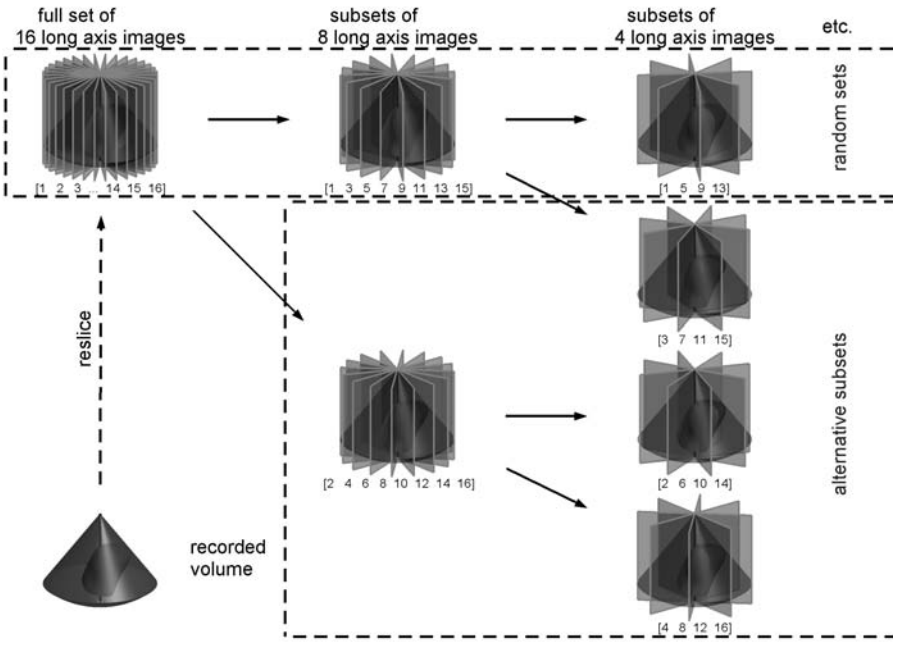

Figure 6.3: *A set of equi-angular long axis images is resliced from the recorded volume. By simply reducing the number of images, random subsets are obtained. The alternative subsets are used when selection is based on their orientation.*

to 12 cine short-axis series (slice thickness 8 mm, gap 2 mm) covering the heart from base to apex were acquired. Images were recorded using a breath hold cardiac triggered steady-state free precession sequence with a temporal resolution and time to echo of 3.5 and 1.3 milliseconds, respectively, and a flip angle of 45 degrees. Additional imaging parameters were: a field of view of 340 × 255 mm, a matrix of 160 × 128, and a temporal resolution of 28 milliseconds. The whole protocol was within 30 minutes.

Quantitative analysis was performed using standardized software (MassPlus, General Electric, Milwaukee, Wisconsin, USA). With this software endocardial contours were semiautomatically traced on all end-diastolic and end-systolic images to calculate the LV volumes and ejection fraction using the disk summation method. An investigator blinded to the 3DE data reviewed the automated tracings.

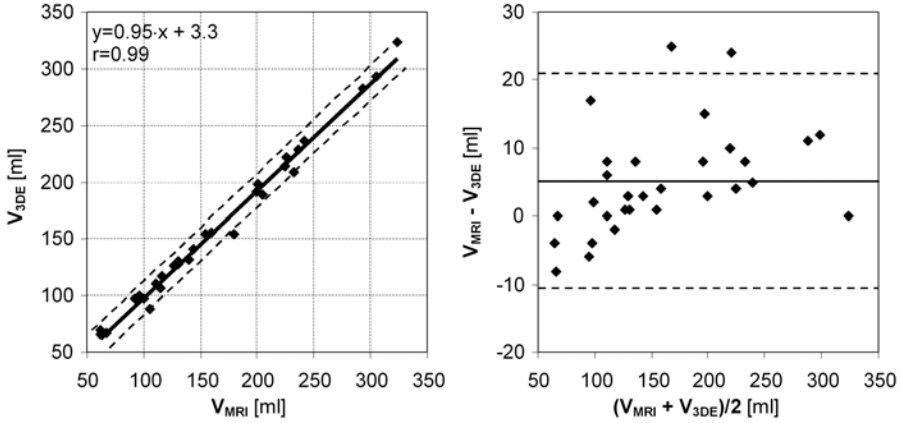

Figure 6.4: *Regression and limit of agreement results from the comparison of left ventricular volumes obtained from magnetic resonance imaging (MRI) and three dimensional echocardiography (3DE), using 16 equiangular long-axis images. Left, regression line between the two methods. Dashed lines delimit the 95 % prediction interval. Right, scatter plot of the difference between MRI and 3DE as function of the average volume. Solid and dashed lines depict the mean and two times SD of the difference, respectively.*

6.2.5 Statistical Analysis

MRI and 3DE results from the full set of 16 long-axis images were compared using the paired *t*-test, regression and agreement analysis [Bland 1986]. The results from the full image set were used as a reference for the various subsets to avoid the influence of the variance from the MRI results on the comparison [Gopal 1992]. A repeated measures analysis of variance was used to assess the differences between the results from the full image set and the random 8, 4, and 2 subsets. The results from the 2D quantification methods were not included in the analysis of variance for reasons of unequal variance. Post hoc testing was performed with the paired *t*-test. Ultimately, regression and agreement analysis was used to explore the echocardiographic data. All data was tested for normality with the Shapiro-Wilk test (SPSS 11.0.1, SPSS Inc., Chicago, Illinois, USA). A probability level of p less than .05 was considered significant.

Table 6.1: *Regression and post hoc test results from the comparison between three dimensional echocardiographic left ventricular volumes obtained from 16 long-axis images and those obtained with fewer images.*

no. of images	r	y (ml)	**LoA** (ml)	**SEE** (ml)	**paired t-test**
8	1.00	$1.01x - 1.5$	0.6 ± 7.2	3.6	NS
4 (selected)	1.00	$1.03x - 6.9$	1.5 ± 12	5.5	NS
4 (random)	1.00	$0.94x + 5.5$	3.4 ± 12	4.3	$p<0.005$
2	0.99	$0.82x - 5.4$	34 ± 30	8.4	$p<0.001$
2 (DS)	0.89	$0.70x + 41$	6.0 ± 65	26	NS
1 (SPAL)	0.80	$0.61x + 63$	-0.8 ± 83	32	NS

DS: disk summation method; LoA: limits of agreement expressed as the mean difference and 2SD; NS: not significant; SEE, standard error of the estimate (or residual SD); SPAL: single plane area length method.

6.3 Results

The Shapiro-Wilk test for normality was not significant, indicating that the data did not significantly deviate from the normal distribution. LV volume measurements ranged from 62 to 323 ml for MRI and from 66 to 323 ml for 3DE when 16 long-axis images were included ($p<0.005$). Results of the regression and agreement analysis from the full image set and MRI are shown in figure 6.4. A good correlation was observed between MRI and 3DE with 16 long-axis images ($r=0.99$; $y=0.95x + 3.3$ ml; standard error of the estimate=7.0 ml). The agreement analysis demonstrated a mean difference of 5.2 ± 15.7 ml.

The repeated measures analysis of variance revealed a significant difference over the number of random long-axis images used for LV volume quantification ($F=133$, $p<0.001$). Table 6.1 gives an overview of the comparison results when volumes obtained from randomly chosen subsets of 8, 4, and 2 images were compared with those from the full set of 16 images. Only volumes from the subset of 8 images appeared to be not significantly different from those of the full image set ($p<0.001$) (table 6.1 and figure 6.5).

When the selected subsets of 4 images were used the LV volumes were no longer significantly different from those of the full image set (table 6.1). An improvement in the slope of the regression and the mean difference was observed. Figure 6.6 shows an example of the effect on the volume quantification when images were selected using the most eccentric point on the

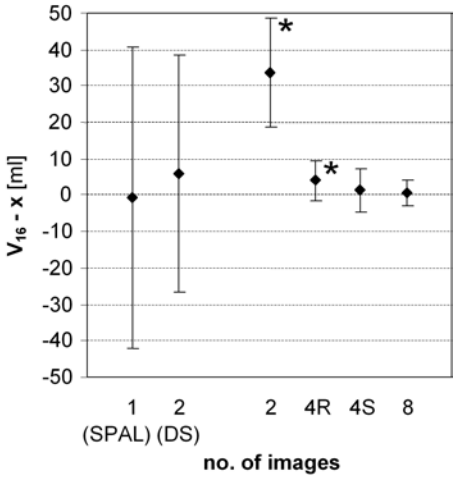

Figure 6.5: *Differences between left ventricular volumes obtained with the full set of 16 equiangular long-axis images (V16) and the various subsets. DS: Disc summation method; SPAL: single plane area length method; 4R: 4 random equiangular long-axis images; 4S: 4 selected equiangular long-axis image; *: results that deviated significantly from those of full image set (p<0.001).*

endocardial border. The resulting surface-rendered volume from the selected subset of 4 images was improved compared with the result of the random subset of 4 images.

6.4 Discussion

This study shows that accurate LV volume quantification can be performed using analysis of 8 equiangular long-axis images. By selecting the correctly oriented image set, using the most eccentric point on the endocardial border, the number of images to be analyzed can be brought down to 4. With a limit of agreement interval of 15.7 ml and a standard error of the estimate of 7.0 ml our method performs better than the methods of several similar studies [Iwase 1997, Mannaerts 2003, Kuhl 2004]. In accordance with these studies, MRI-derived volumes were significantly higher than those from 3DE. An explanation for this overestimation is likely caused by differences between the tracing methods. The analysis software (TomTec Imaging Systems) requires long-axis images for endocardial border detection, whereas the MRI software

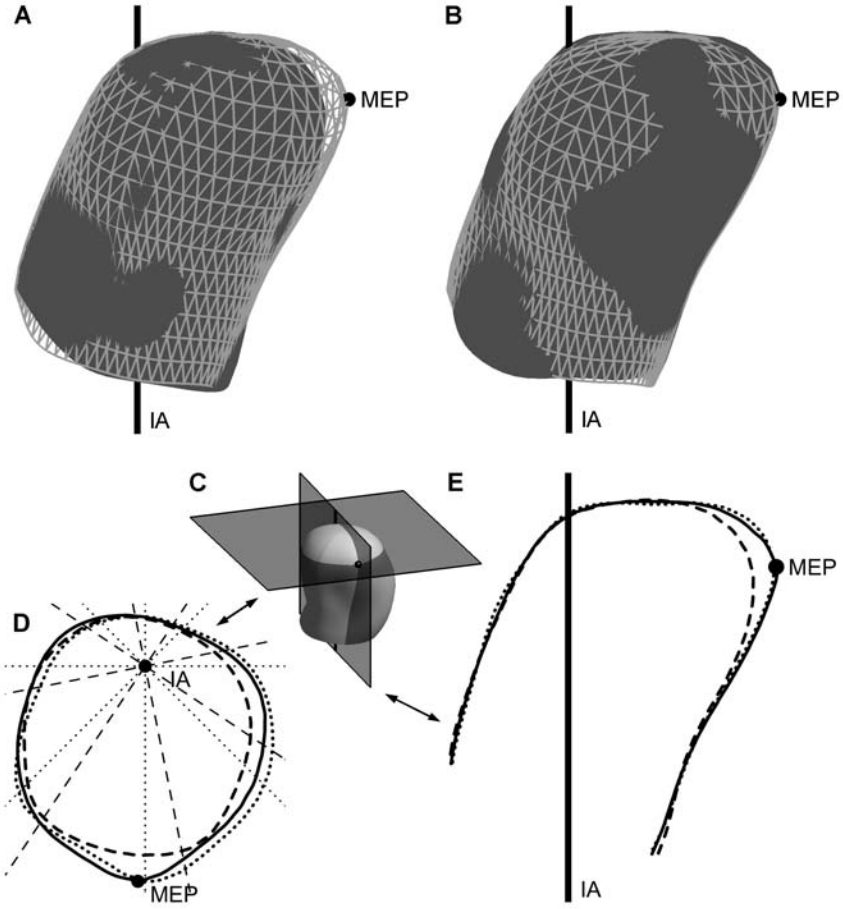

Figure 6.6: ***A** and **B**. Surface-rendered example of left ventricular volume measurement results from full set of 16 equiangular long-axis images (light wire frame) and 4 random equiangular images (dark solid surface). **A**. The gap between both results around the most eccentric point (MEP) can be clearly appreciated. **B**. When 4 long-axis images were selected in respect to MEP, the difference with full image set is negligible. **C**. Long- and short-axis view at angle and level of the MEP. **D** and **E**. Solid, dashed, and dotted curves depict analysis result from 16, 4 random, and 4 selected images, respectively. **D**. The thin dashed and dotted lines depict the orientation of 4 equiangular long-axis images from random and selected image sets, respectively. IA, Imaging axis.*

Table 6.2: *Results from related studies including the results from this study.*

author	**subject**	**ref. method**	**range** (ml)
Voormolen	15 patients	MRI	62–323
(this study)		echo (16 images)	66–323
		MRI	62–323
		echo (16 images)	66–323
Nixorff, 2005	16 latex models	actual volume	56–303
Teupe, 2001	12 fixed porcine models	actual volume	5–149
	8 aneurysmal ...	actual volume	9–40
Kühl, 2000	24 patients	echo (60/90 images)	unknown
Nosir, 2000	5 volunteers and	MRI	218 ± 98 (LVEDV)
	16 patients		154 ± 98 (LVESV)
Nguyen, 1999	9 volunteers and 6 pts.	echo (±17 images)	36–433
Yao, 1999	3 volunteers and 7 pts.	echo (90 images)	119±23 and 74±21
Danias, 1998	41 patients	MRI	unknown (LVEDV)
			unknown (LVESV)
Tanabe, 1998	6 excised canine models	actual volume	29–105
Krebs, 1996	7 silicon rubber models	actual volume	165–265
Siu, 1996	10 open chest	actual volume	14–85 (LVEDV)
	canine models		4–73 (LVESV)
Aakhus, 1994	18 latex balloons	actual volume	32–349
Weiss, 1983	5 isolated canine models	actual volume	9.4–45

LoA: limits of agreement expressed as mean difference (reference minus investigated method) and 2SD; LVEDV: left ventricular (LV) end-diastolic volume; LVESV: LV end-systolic volume; MRI: magnetic resonance imaging; SEE: standard error of the estimate (or residual SD).

uses short-axis images for the disk summation method. With this method part of the aortic root, left atrium, or both is included in the most basal disk.

In addition, a slight increase of the difference between 3DE and MRI as a function of the ventricular volume can be observed in figure 6.4. The relation is, however, weak and the sample size of this study is too small to investigate this suggested effect. Nevertheless, a possible explanation might be a different manifestation of the trabeculae in end diastole and end systole. Where the trabeculae will form a compact layer in end systole, individual trabeculae can be identified during end diastole, forming an irregular, undulated surface [Mannaerts 2003]. As MRI shows the blood between the trabeculae, the observer will be inclined to include the trabeculae while tracing the end-diastolic

Table 6.2: *(continued)*

	no. of images	***r***	**LoA** (ml)	**SEE** (ml)	**author** (duplicate)
	8 (long axis)	0.99	5.8 ± 20	9.3	Voormolen
	idem.	1.00	0.63 ± 7.2	3.6	(this study)
	4 (long axis)	0.99	6.6 ± 19	9.7	
	idem.	1.00	1.5 ± 12	5.5	
	6 ± 2 (short axis)	1.00	1.0 ± 7.5	unknown	Nixorff, 2005
	3 (long axis)	0.99	−1.8 ± 17	7.1	Teupe, 2001
	3 (long axis)	0.95	2.7 ± 7.5	3.1	
	9(long axis)	0.99	0.2 ± 8.2	4.9	Kühl, 2000
	11 (long axis)	0.98	3.1 ± 38	unknown	Nosir, 2000
	idem.	0.99	0.8 ± 29	unknown	
	5 (short and long axis)	unknown	2 ± 12	5.1	Nguyen, 1999
	12 (long axis)	0.97	6.3 ± 16	8.5	Yao, 1999
	10 (short and	0.97	−0.4 ± 18	unknown	Danias, 1998
	long axis)	0.99	−0.2 ± 18	unknown	
	4 or 6 (long axis)	0.99	−0.5 ± 7.4	3.3	Tanabe, 1998
	9 (long axis)	unknown	unknown	unknown	Krebs, 1996
	8–12 (short and	0.96	0.65 8.9	4.4	Siu, 1996
	long axis)	0.97	−0.33 ± 7.4	4.0	
	3 (long axis)	1.00	3.0 ± 7.2	3.7	Aakhus, 1994
	4 (short axis)	0.94	2.4 ± 4.2	3.3	Weiss, 1983

endocardial border. In 3DE images, the inner tissue-to-blood transitions of the trabeculae cause relatively strong reflections and the observer will be inclined to trace within the trabeculae, (partly) excluding them. This might have caused the increased discrepancies for the larger LV volumes, which will mostly consist of end-diastolic volume.

The superiority of 3DE for LV volume quantification as compared with 2D methods, as a result of the absence of geometric assumptions, has been demonstrated [Buck 1997]. However, the results were mostly obtained with large numbers of cross-sectional images [Nosir 2000]. Only a few studies have focused on the number of cross-sectional images needed for accurate LV volume quantification. Table 6.2 shows a complete overview of these studies. Two patient studies, listed in table 6.2, also used MRI as the reference method. Nosir *et al.* [2000] performed worse than this study using twice the number of long-axis images. Danias *et al.* [1998] showed comparable results

with slightly more short- and long-axis images. In the other patient studies echocardiography was used as the reference method. Kuhl *et al.* [2000] performed slightly better than this study but used transesophageal echocardiography and twice the number of long-axis images. Nguyen *et al.* [1999] found comparable results using the same number of short- and long-axis images. However, these results were obtained with additional information about the apex, mitral valve, and aortic valve from a set of 17 images. Yao *et al.* [1999] showed worse results with 3 times the number of long-axis images. The results from these patient studies, therefore, support our conclusion that LV volumes can be accurately determined using 4 equiangular long-axis images in combination with prior information about their orientation. In addition, 4 of the 6 nonpatient studies presented in table 6.2 claim accurate volume measurement with 3 or 4 images [Teupe 2001, Tanabe 1998, Siu 1996, Weiss 1983]. The volume range of these studies was 3 times smaller than in our study, which explains the slightly better results. In the two in vitro studies for which this was not the case static balloons and latex models were used [Nixdorff 2005, Aakhus 1994]. Unfortunately, the study of Krebs *et al.* [1996] can not be discussed because no comparable data were presented.

This study shows an improvement of the LV volume measurement when 4 equiangular long-axis images are selected in respect to the most eccentric point on the endocardial border. Eccentricity of the endocardial border in the images used for analysis can occur as a result of inherent asymmetry of the LV after myocardial infarct or as a result of a misalignment between the imaging axis and the LV axis [Takemoto 2003]. The latter suggests that it is best to align the imaging axis with the LV axis to reduce the eccentricity of the endocardial border in the images to analyze. Unfortunately, with most patients the position that offers the best alignment of both axes is not the position that provides the best acoustic window. This can be remedied by reslicing the recorded data set along the ventricular axis. However, for this alternative approach the ventricular axis has to be determined before the data set can be resliced, which requires additional analysis efforts.

6.5 Conclusions

This study demonstrates that accurate LV volume quantification is possible with 8 randomly selected equiangular long-axis images. Based on prior information about the orientation of the recorded images in respect to the endocardial border, a selection of 4 long-axis images can also be used. The combination of short acquisition times, advanced quantification software, and

the general advantages of echocardiography make 3D echocardiography suitable for rapid determination of the LV function in the daily clinical practice.

Part III

Advanced Applications

Chapter 7

Three Dimensional Echocardiographic Analysis of Left Ventricular Function during Hemodialysis

Villamanin, León, Spain, July 29th, 2007: *Although this chapter describes a quite laborious clinical study, this is not the figurative mountain. This is El Cueto Fontún (1953 m), around (and on top of) which I have enjoyed my summer vacations the last 10 years.*

The effects of hemodialysis (HD) on left ventricular (LV) function have been studied by various echocardiographic techniques (M-mode, 2D echocardiography). These studies are hampered by a low accuracy of measurements because of geometric assumptions regarding LV shape. Three dimensional echocardiography (3DE) overcomes this limitation.

We tested the feasibility of 3DE assessment of LV function during HD. Conventional biplane Simpson rule (BSR) and single plane area length method (SPM) for LV function analysis were used as a reference.

12 HD patients were studied and in 10 (83 %) a total of 80 3D datasets were acquired. In 3 patients, one dataset (4 %) was of insufficient quality and excluded from analysis. Correlation between SPM, BSR and 3DE for calculation of end-diastolic (EDV, r=0.89 and r=0.92, respectively), end-systolic volume (ESV, r=0.92 and r=0.93, respectively) and for ejection fraction (EF, r=0.90 and r=0.88, respectively) was moderate. Limits-of-agreement results for EDV and ESV were poor with confidence intervals larger than 30 ml. Both 2DE methods underestimated end-diastolic and end-systolic volume, while overestimating ejection fraction.

3DE is feasible for image acquisition during HD, which opens the possibility for accurate and reproducible measurement of LV function during HD. This may improve the assessment of the acute effect of HD on LV performance, and guide therapeutic strategies aimed at preventing intradialytic hypotension.

Based on:

© 2007 Karger. Reprinted, with permission, from: **Krenning, B.J.**, M.M. Voormolen, M.L. Geleijnse, A.F.W. van der Steen, F.J. ten Cate, E.H.Y. Ie and J.R.T.C. Roelandt. Three-Dimensional Echocardiographic Analysis of Left Ventricular Function during Hemodialysis. *Nephron Clinical Practice*, 107(2):c43–c49, 2007.

7.1 Introduction

Intradialytic hypotension is an important complication of hemodialysis (HD). Although its pathogenesis is not completely understood, it is clear that the decrease in blood volume due to ultrafiltration is the most important initiating factor. Hypotension results from a decreased product of stroke volume (SV), heart rate (HR) and systemic vascular resistance. The continuing volume withdrawal during HD is a hemodynamic challenge which may lead to an inability to generate sufficient cardiac output (CO). However, there is a large inter- and intraindividual variability regarding the incidence of intradialytic hypotension. Therefore, to better understand the interplay between progressive volume withdrawal and changes in LV performance during HD, studies have been conducted using various echocardiographic techniques, including M-mode echocardiography [Chaignon 1982, Cohen 1979], two dimensional echocardiography (2DE) [Bornstein 1983, Zoccali 2004] and Doppler imaging [Gupta 1993, Galetta 2006, Ie 2003]. Nevertheless, the acute effect of HD on cardiac function remains poorly understood, due to conflicting results. A number of factors influence cardiac function measurements, such as loading conditions [Ie 2003, Tomson 1990]. Earlier LV performance studies may have been hampered by a low accuracy of measurements. M-mode and 2D echocardiography are limited by geometric assumptions as to volume and function calculation. Three dimensional echocardiography (3DE) overcomes this limitation, and has recently become a feasible method for rapid and accurate measurement of LV function in a clinical rather than research setting [Monaghan 2006]. In this study, we therefore evaluate the feasibility of 3DE assessment of LV function during HD. Also, we compared our 3D results with conventional 2D methods for LV function analysis.

7.2 Methods

7.2.1 Patients

Twelve patients on chronic intermittent HD entered the study. Two patients were excluded because of insufficient 3D echocardiographic image quality. The remaining 10 patients had a mean age of 56 ± 15 years. All patients were in sinus rhythm and were dialyzed three times a week according to a standard dialysis program, which had been unchanged for three months or longer. No medication was discontinued for this study. Four patients had a history of cardiac disease (2 coronary interventions, 1 myocardial infarction,

1 angina pectoris). The mean heart rate (± standard deviation, SD) during echocardiographic examination was 68 ± 10 bpm. All patients gave informed verbal consent.

7.2.2 Hemodialysis

All dialysis treatments used Fresenius 4008 machines (Fresenius Medical Care, Bad Homburg, Germany), biocompatible membranes (Hemophane or Polysulphone) and bicarbonate-buffered dialysate (Fresenius Medical Care SK-F213). The duration of the dialysis procedure was 4 h in all patients. During the first 30 min patients were connected to the dialysis machine with only blood flow (recirculation) but no HD or ultrafiltration (UF) taking place. The mean amount of fluid withdrawn was 2617 ± 1088 ml.

7.2.3 Three Dimensional Echocardiography

We used a new prototype transthoracic, fast-rotating 64-element array transducer with a center frequency of 3 MHz. Technical aspects have been described elsewhere [Voormolen 2006]. In short, this transducer features the capability of second harmonic imaging and continuously rotates around its central axis with a maximum rotation speed of 480 rotations per minute. The transducer is connected to a commercially available ultrasound system (Vivid 5, GE VingMed Ultrasound, Horton, Norway). A validation study using cardiac magnetic resonance imaging as a reference showed a strong correlation and good inter- and intra-observer agreement [Krenning 2006].

7.2.4 Image Acquisition

3DE was performed before HD, 5 minutes after patient connection to the HD system, during recirculation without UF (after 30 minutes), every hour during HD with UF, and 15 minutes after HD. In total, 8 acquisitions were performed in each patient. Patients were studied in a partial left lateral decubitus position during HD. The transducer was placed in the apical position with the image plane rotating around the LV long axis. The depth settings were adjusted to visualize the entire LV and part of the left atrium. Gain and power settings were optimized for endocardial border visualization. The image acquisition was made, in second harmonic imaging mode (transmit frequency: 2 MHz) during a single end-expiratory breath hold of approximately 10 seconds and the ECG was simultaneously recorded for the 3D reconstruction process.

7.2.5 Three Dimensional Image Processing and Analysis

Imaging processing and analysis was performed as previously described [Krenning 2006]. Image data were transferred via a network connection to a dedicated PC for processing and analysis. With custom designed software, based on MatLab (The MathWorks, Natick, Massachusetts, USA), the original 2D images are post-processed into 3D datasets. Subsequently, TomTec 4D LV Analysis software (TomTec Imaging Systems, Unterschleißheim, Germany) was used for further analysis. Eight equidistant cross-sectional image planes were used for analysis. The orientation of these images in 3D space was determined by manually marking the mitral valve, aortic root and apex. Contrast and gain settings were adjusted for optimal endocardial border visualization. Subsequently, the software automatically performed endocardial border detection in all images. One investigator verified the results from the automated border detection and corrected if necessary.

The analysis program displays a reconstruction of the LV as a dynamic surface rendered image, in which LV wall motion is shown in three dimensions (figure 7.1). From an automatically plotted volume-time curve, LV end-diastolic (EDV) and end-systolic volume (ESV) was determined by the maximal and minimal volume and ejection fraction (EF) was calculated.

7.2.6 Two Dimensional Image Processing and Analysis

From the 3D dataset, two perpendicular images were extracted representing the apical 2D four- and two-chamber views. Manual endocardial border delineation was performed with MatLab using custom designed software. Two common algorithms for 2DE ventricular volume calculation were used, as recommended by the American Society of Echocardiography [Schiller 1989]:

1. The disc summation method or biplane Simpson rule (BSR), based on orthogonal planes from apical two- and four-chamber views. Volumes were computed using the formulation:

$$V = \frac{\pi}{4} \sum_{i=1}^{20} a_i b_i \frac{L}{20} \tag{7.1}$$

   Where V is the LV volume, a and b represent the diameters of the discs and L is the cavity length (see figure 7.2).

2. The single plane area length method by calculation of LV end-diastolic and end-systolic volumes and ejection fractions from the four-chamber view.

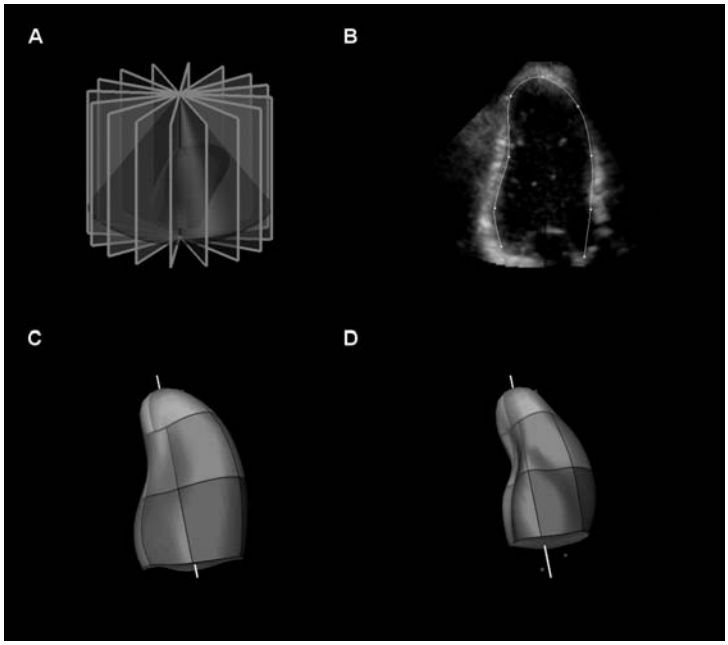

Figure 7.1: ***A.*** *The LV is divided into 8 equidistant cross-sectional images which are used for contour analysis.* ***B.*** *An original image of an apical long axis view during fast rotation. Reconstruction of the LV in end diastole (C), and end systole (D).*

Volumes were computed using the formulation (figure 7.2):

$$V = 0.85\frac{A^2}{L} \tag{7.2}$$

Where V is the LV volume, A is the cavity area and L is the cavity length (see figure 7.2).

7.2.7 Inter- and Intra-Observer Variability

To assess inter-observer variability for 2DE, the first two acquisitions of each patient were independently analyzed by another observer blinded to previous results. For assessment of intra-observer variability, the first observer repeated analysis in a random order. Both were blinded to 3DE results. Data on

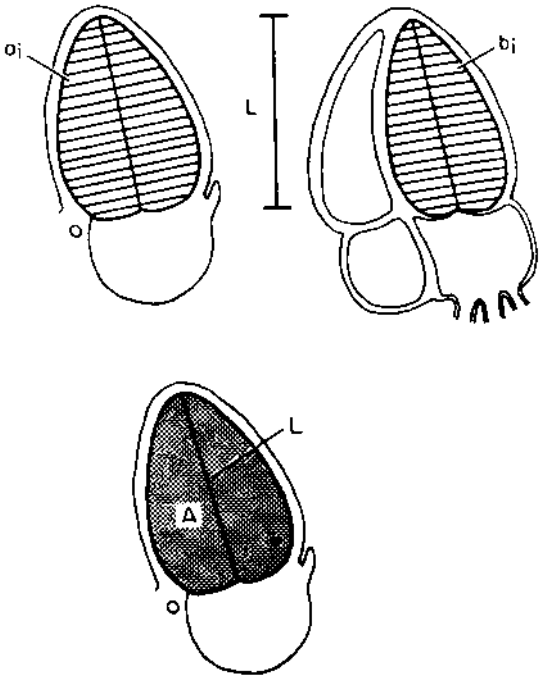

Figure 7.2: *Top, Biplane Simpson rule for calculating LV volume, based on orthogonal planes from apical 2- and 4-chamber view. Bottom, Single plane area length method, based on a single apical view. © 1989 American Society of Echocardiography. Reprinted, with permission, from Schiller et al. [1989].*

inter- and intra-observer variability for 3DE were available from a previous validation study [Krenning 2006].

7.2.8 Statistical Analysis

Results for EDV, ESV and EF are represented as mean and SD. Data was tested for normality with the Shapiro-Wilk test. A repeated- measures ANOVA was used for analysis of differences within the variations. Post-hoc testing was performed with the paired *t*-test. Regression and limits of agreement analysis was performed for 3DE and 2DE measurements according to the method of Bland *et al.* [1986]. Results for inter- and intra-observer variations are

Table 7.1: *Results of regression analysis and Bland-Altman analysis comparing LV volume and function with 3DE and 2DE methods (see text for details).*

single plane method	***r***	***y***	**SEE**	**LoA**	**paired *t*-test**
EDV (ml)	0.89	$0.88x - 0.86$	23.12	-16.2 ± 22.7	<0.05
ESV (ml)	0.92	$0.80x + 1.33$	15.43	-15.3 ± 16.7	<0.02
EF (%)	0.90	$0.93x + 5.55$	4.87	3.1 ± 4.6	NS
biplane Simpson	***r***	***y***	**SEE**	**LoA**	**paired *t*-test**
EDV (ml)	0.92	$0.85x - 3.04$	18.91	-21.9 ± 19.4	<0.01
ESV (ml)	0.93	$0.82x - 1.57$	14.20	-16.8 ± 15.4	<0.01
EF (%)	0.88	$0.92x + 4.60$	5.27	1.7 ± 5.0	NS

LoA: limits of agreement expressed as mean difference ± 2SD; SEE: standard error of the estimate (or residual SD); NS: not significant.

represented as mean ± SD for the difference between the two measurements. $p<0.05$ was considered to be significant.

7.3 Results

Successful image acquisition was achieved in 10 out of 12 patients (83 %). A total of 80 3D datasets were acquired in these 10 patients. In 3 patients, one dataset (4 %) was of insufficient quality and excluded from analysis. One patient suffered from symptomatic hypotension during HD, although no intervention was required. The time for data analysis averaged 15 ± 5 minutes per 3D dataset.

The test for normality was not significant, indicating that the data did not significantly deviate from the normal distribution. Repeated measures ANOVA showed a significant difference between the measurement methods ($F=10.5$; $p<0.02$) but no significant difference between the moment of measurement ($F=0.57$, $p<0.78$). Because a significant effect in time was not found, the data was averaged for further analysis.

Correlation between the 2DE methods and 3DE for EDV ($r=0.92$), ESV ($r=0.93$) and EF ($r=0.90$) was moderate (figure 7.3). However, the limits-of-agreement between methods for EDV and ESV were poor with confidence intervals all larger than 30 ml (table 7.1). ANOVA analysis for EDV, ESV and

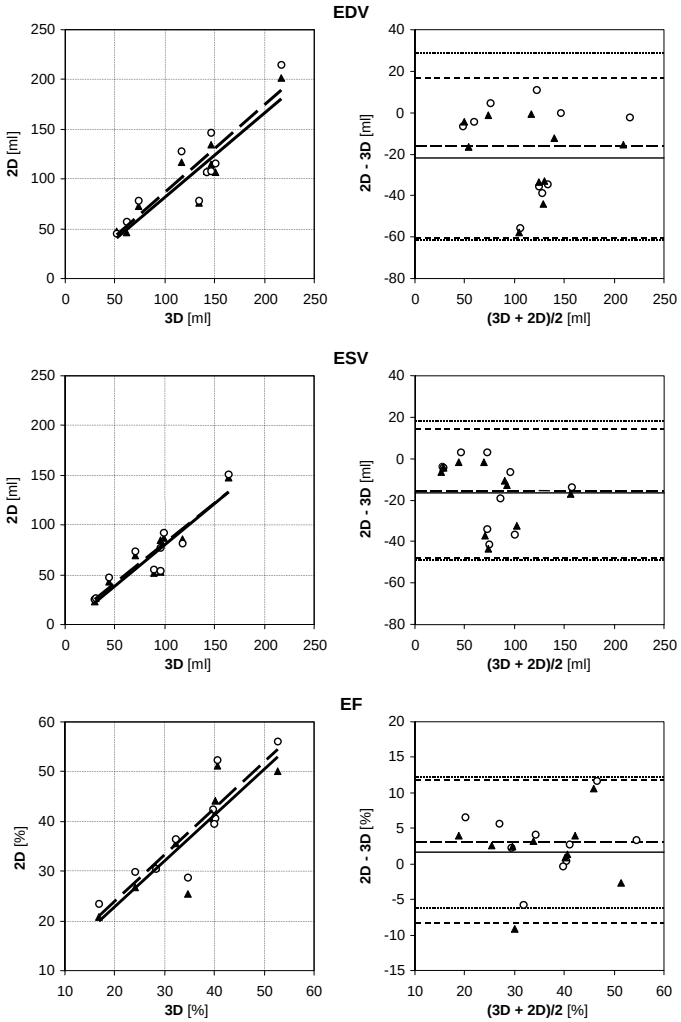

Figure 7.3: *Relation between 3DE and 2DE measurements of EDV, ESV, and EF. The left panels show the regression analysis between the two methods. Dashed lines delimit 95 % confidence interval. ▲, solid line: biplane Simpson method; ○, dashed line: single plane area length method. The right panels show plots of the difference between 3DE and 2DE, as a function of the average calculated volumes. Solid and dashed lines represent mean ± 2SD of the difference, respectively. EDV: left ventricular end-diastolic volume; EF: left ventricular ejection fraction; ESV: left ventricular end-systolic volume.*

EF showed significant differences between the different measurement methods (F=8.4, p<0.005). Post-hoc testing showed that both 2DE methods significantly underestimated EDV and ESV compared to 3DE. Limits-of-agreement analysis for EF showed an overestimation for both 2DE methods. However, these differences were not significant compared to 3DE.

7.3.1 Inter- and Intra-Observer Variability

The limits of agreement analysis of 3DE data from measurements performed by the first observer showed a mean difference of −1.4 ± 6.6 ml for EDV, −0.1 ± 4.4 ml for ESV and −0.3 ± 2.4 % for EF. For 2DE using SPM, the results were −1.2 ± 11.4 ml, −3.2 ± 16.0 ml and 1.6 ± 10.6 %, respectively. For 2DE using BSR, the results were 3.9 ± 13.9 ml, 1.7 ± 15.2 ml and 0 ± 10.5 %, respectively.

The limits of agreement analysis demonstrated a mean difference of −0.1 ± 11.7 ml for LVEDV, 1.3 ± 8.7 ml for LVESV and −0.7 ± 4.8 % for LVEF, for 3DE data by two independent observers. For 2DE using SPM, the results were 0.3 ± 8.1 ml, −10.6 ± 22.3 ml and 7.1 ± 14 %, respectively. For 2DE using BSR, the results were −3.4 ± 14.7 ml, −2.5 ± 16.4 ml and 1.0 ± 10.3 %, respectively.

7.4 Discussion

This study demonstrates that image acquisition using 3DE is feasible for accurate evaluation of LV function in patients during HD. Previous studies showed that 3DE calculates LV volume with a precision comparable to cardiac magnetic resonance imaging [Krenning 2006, Gutierrez-Chico 2005, Corsi 2005]. While both techniques are superior to 2DE, magnetic resonance imaging is not feasible during HD. Tissue Doppler imaging (TDI), a newer Doppler technique advocated as less load-dependent [Sharma 2006, Barberato 2004], can be used during HD [Ie 2006]. TDI primarily yields information on myocardial contraction and relaxation, but is less used for assessment of overall LV performance, which is usually expressed using the well-known parameters SV and ejection fraction.

The large interval between the limits of agreement and the underestimation of LV volume by 2DE are in line with previous reports [Krenning 2006, Jenkins 2004]. 2DE calculations of LV function using the disc-summation method is based on the assumption that a ventricle can be represented by a series of stacked elliptic discs of varying diameters. In patients with regional wall motion abnormalities and deformed ventricles, this assumption

may be unjustified and result in an inaccurate and poor reproducibility of 2DE measurements. Using 3DE, however, no assumption is made about the shape of the LV, and LV volume is calculated from a much greater set of data. Therefore, 2DE should be used with caution for LV function analysis when relatively small differences in LV volume are expected, as during HD. When more image planes are used for LV volume calculation, as in 3DE, an increase in accuracy is observed. Previous studies suggested that at least four to eight image planes are necessary to accurately represent the ventricular volume [Tanabe 1998, Siu 1996]. Nosir *et al.* [2000] showed that a 1 % change in LV volume can be observed with a 90 % likelihood when 8 image planes are used.

To our knowledge, this is the first study to use 3DE during HD. Only one study used 3DE in HD patients for LV function determination [Fathi 2003]. However, this study was not performed in the HD department. Accurately assessing the changes in LV volumes during HD can result in a better insight into the development of dialysis hypotension. Especially the role of the so-called *Bezold-Jarisch reflex*, which leads to bradycardiac hypotension believed to be triggered by a severely underfilled LV, is not well understood. Monitoring changes in LV filling may help predicting the onset of hypotension, and may guide therapeutic strategies such as ultrafiltration profiling. Additionally, more reproducible assessment of LV volumes, function and mass helps cardiovascular risk stratification, which is important not only for managing the dialysis population but also for the work-up of renal transplant candidates among dialysis patients.

Our study is limited by the small number of patients. However, this study was not designed to determine the effect of a single HD session on LV performance. During image acquisition, a partial left lateral decubitus position and 10 seconds breath-hold were required. This was well-tolerated by the HD patients in our study. 3DE relies on achieving good endocardial border definition which depends on various factors. As patients in the HD department cannot be positioned in the most optimal way as they are in the echocardiography department (because of interference with blood lines, absence of examination table), this could hamper optimal image quality. Although effort was required by patient and ultrasonographist, we could acquire sufficient image quality in 80 % of patients. In only 3 patients was a single acquisition of insufficient quality. Previous studies have shown an improvement in image quality [Kasprzak 1999] and, subsequently, smaller limits of agreement in inter- and intra-observer variability when intravenous ultrasound contrast agents are used [Yu 2000, Malm 2004]. Further studies are necessary to evaluate the feasibility thereof in this patient population.

7.5 Conclusion

We conclude that successful image acquisition for 3DE is feasible for accurate and reproducible measurement of LV function during HD. This may improve the assessment of the acute effect of HD on cardiac function, and guide therapeutic strategies aimed at preventing intra-dialytic hypotension.

Acknowledgement

We would like to thank Jerome Borsboom for his assistance in the statistical analysis.

Chapter 8

3D Contrast Harmonic Echocardiography

Rotterdam, January 26th–27th, 2006: *Of all the symposia that I have attended in the last six years, the annual European Symposium on Ultrasound Contrast Imaging have certainly been the most enjoyable ones. I have met a considerable amount of like-minded people, from which some became real friends. As a consequence the late hours of this symposium are spend drinking Oude Jenever with the usual suspects.*

Fast acquisition and reconstruction is required for 3D-echocardiography to be applicable and accepted as a clinical tool. We developed a fast rotating phased array transducer for 3D-imaging of the heart with harmonic capabilities making it highly suitable for contrast imaging. In this study the feasibility of 3D harmonic contrast imaging was evaluated in-vitro and in-vivo. This goal is pursued because improved endocardial border delineation with the application of contrast agents should allow for less complex and faster quantification algorithms.

A commercially available tissue mimicking flow phantom was used in combination with Optison microbubbles. Backscatter power spectra from a tissue and contrast regions of interest were calculated from recorded radio frequency data. The spectra and the extracted contrast to tissue ratio from these spectra were used to optimize the excitation frequency, the pulse length and the receive filter settings for the transducer. Frequencies ranging from 1.6 to 2.5 MHz and pulse lengths of 1.5 and 2.5 cycles were explored.

An increase of 8 dB in the contrast to tissue ratio was found at the second harmonic compared to the fundamental frequency. This was found for an optimal transmit frequency of 1.74 MHz and an optimal pulse length of 2.5 cycles. For these optimal transmit settings the receive filter was configured with a center frequency of 3.6 MHz and a bandwidth of 1.3 MHz giving the maximum harmonic amplitude. Using the optimized settings, clinical harmonic contrast recordings were made.

The results presented in this chapter show the feasibility of 3D contrast imaging and improved endocardial border delineation when used in combination with harmonic imaging.

Based on:

© 2003 Elsevier. Reprinted, with permission, from: **Voormolen, M.M.**, A. Bouakaz, B.J. Krenning, C.T. Lancée, F.J. ten Cate and N. de Jong, Feasibility of Harmonic Contrast Imaging. *Ultrasonics*, 42(1–9):739–743, 2004.

© 2004 IEEE. Reprinted, with permission, from: **Voormolen, M.M.**, A. Bouakaz, B.J. Krenning, C.T. Lancée, A.E. van den Bosch, F.J. ten Cate and N. de Jong. 3D Contrast Harmonic Echocardiography. *Proceedings of the IEEE Ultrasonics Symposium*, 1:114–117, 2004.

8.1 Introduction

Ultrasound contrast agents (UCA), consisting of microbubbles, are used to enhance the echoes from a blood pool to which they are added [Goldberg 2001]. In fundamental (B-mode) imaging, UCA increase the backscattering of blood to a level close to that of tissue. Discrimination between blood and tissue is therefore compromised which can be quantified with the so-called *contrast to tissue ratio* (CTR). Microbubbles, however, reveal a non-linear oscillation when insonified with a sufficiently high acoustic pressure wave [De Jong 1994a,b]. As a result the backscatter signal of UCA contain the transmitted frequency and also its multiples or harmonics. Since tissue does not comprises a non-linear scattering behaviour of the same magnitude this offers an opportunity to distinguish between the backscatter signal from UCA and tissue. Unfortunately, harmonic frequencies are also generated by propagation of the ultrasonic wave through tissue and blood [Hamilton 1998, Aronson 2000]. The backscatter of these generated harmonics from tissue will hamper the distinction of harmonics radiated by the microbubbles and reduce the CTR. However, it has been shown that CTR levels for second harmonic imaging are much higher than those of fundamental imaging [Bouakaz 2002].

Since it provides information not only from a single cross-section, as with 2D-imaging, but from the complete volume under investigation the advantages of 3D echo are numerous. A few of these advantages are: accurate quantification of cardiac properties, extraction of 2D any plane images and dynamic 3D views of cardiac structures [Salustri 1995, Krenning 2003]. 3D contrast imaging can add to these advantages since tissue often exhibits non-homogeneous scattering resulting in drop out. This is especially problematic when border tracing algorithms are used for quantification of the recorded echo data. When used at an appropriate concentration, UCA give a homogeneous and complete opacification. This characteristic could be beneficial for the development of less complex and faster tracing algorithms through improved endocardial border delineation with UCA.

Most array transducers used for medical imaging exhibit a wide bandwidth that covers the fundamental transmit frequency as well as its second harmonic. We developed a fast rotating phased array transducer for 3D-imaging of the heart with harmonic capabilities making it highly suitable for contrast imaging. In this study the feasibility of 3D contrast harmonic imaging (CHI) was evaluated in-vitro and in-vivo.

In-vitro measurements were used to optimize the transmit and receive settings for 3D-CHI. Determination of the optimal transmit settings was based on the highest CTR calculated from radio frequency (RF-)data. Transmission

frequencies ranging from 1.6 to 2.5 MHz and pulse lengths of 1.5 and 2.5 cycles were explored. The receive settings were optimized in terms of center frequency and bandwidth of the receive filter. As contrast agent Optison was used. Ultimately 3D-CHI was used for clinical evaluation with patients recordings.

8.2 Methods

8.2.1 Fast Rotating Ultrasound Transducer

The fast rotating ultrasound (FRU-)transducer consists of three major parts: a DC motor that drives the array, a slip-ring device with 82 contacts, establishing signal transfer to and from the rotating array, and a linear phased array (see chapter 3).

The DC motor drives the array at a rotation speed ranging from 240 to 480 rpm and is connected to an external control system with a manual setting for the rotation speed. A 4Ddataset (three spatial dimensions and time) can be acquired in a short time (e.g. 1 second), resulting in a sparse sampling of the time-volume space. Longer acquisitions yield a much denser sampling. The typical acquisition time is approximately 10 seconds, which has proven to be convenient for clinical application.

The array of the transducer, custom made by Delft Instruments (Delft, The Netherlands), contains 64 elements with a pitch of 0.21 mm and is tapered into an octagonal shape, approximating a circle with a radius of 7 mm. It has a fractional bandwidth of 86 % with a center frequency of 3.2 MHz. The fixed focus of the acoustic lens in the elevation direction was set at 60 mm.

The transducer is connected to a GE VingMed Ultrasound (Horten, Norway) Vivid 5 system. For this study the third prototype of the transducer is used which is shown in figure 8.1. Improvements of this third prototype can be found in the wider bandwidth, allowing improved harmonic imaging, and the more ergonomic design of the transducer.

8.2.2 Hydrophone Measurements

To calibrate the pressure output of the FRU-transducer hydrophone measurements were performed. Recordings were taken at the focal point of the transducer (at approximately 5 cm) for all transmit frequency and pulse length variations used in the in-vitro experiments. From these recordings the peak negative pressure as function of the excitation voltage was extracted.

Figure 8.1: *Third prototype of the fast rotating ultrasound transducer.*

In addition, long pulses (10 cycles) were used to access the transmit sensitivity of the transducer. Again hydrophone measurements were taken at the focal point of the transducer. Frequencies ranging from 1.5 to 5 MHz and an excitation voltage of 5 V were used. The stationary amplitude of the propagated signal was extracted from the recordings and used for a sensitivity plot.

8.2.3 Contrast to Tissue Ratio Measurements

The contrast to tissue ratio (CTR) was defined as the ratio of the scattered power by the contrast to that of the tissue. A commercially available tissue mimicking flow phantom (ATS Laboratories Inc., Model 524, Bridgeport, Connecticut, USA) was used to measure the CTR at different frequencies ranging from 1.6 to 2.5 MHz. This was facilitated by the availability of the RF-data from the scanner.

The voltage-pressure curves obtained from the hydrophone measurements were derated with the attenuation of the phantom (0.5 dB/cm/MHz). Using the derated voltage-pressure curves the derated peak negative pressure was controlled throughout the experiments.

The transmitted pulse contained 2.5 cycles and RF-data was recorded at a frame rate of half a frame per second. Optison (Amersham Health, Princeton,

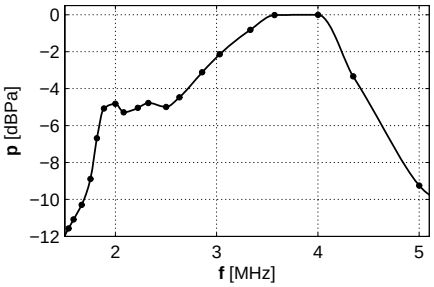

Figure 8.2: *Transmit sensitivity plot of the FRU-transducer.*

New Jersey, USA) was used at a dilution of 1 over 2000 in Isoton II (Beckman Coulter, Fullerton, California, USA) and was flowing at a constant rate of 90 ml/minute. through the phantom from which the 8 mm channel was used. Two-way frequency spectra were calculated from two regions of interest (ROI), one in the tissue and the other in the flow area, at equal depth (approximately 5 cm). The transmit frequency resulting in the highest CTR was selected as the optimal transmit frequency.

A similar procedure was used to determine the optimal pulse length at the optimal transmit frequency. Pulse lengths of 1.5 and 2.5 cycles were investigated. For reasons of resolution preservation larger pulse lengths than 2.5 cycles were not used.

Ultimately the receive filter of the echo system was set according to the obtained CTR results.

8.2.4 Clinical Evaluation

3D contrast harmonic and tissue harmonic recordings were obtained from several patients with various cardiac pathologies. 3D-acquisition was performed during a 10 second breath-hold, at a frame rate of 100 frames per second and a rotational speed of 6 Hz.

After reconstruction of the recorded echo data, quantification was performed with 4D LV Analysis software from TomTec Imaging Systems (Unterschleißheim, Germany) featuring a semi-automated border detection algorithm [2].

8.3 Results and Discussion

Figure 8.2 shows the transmit sensitivity of the FRU-transducer obtained with the hydrophone measurements. The sensitivity plot yielded a fractional bandwidth of 86 % (−6 dB) with a center frequency of 3.2 MHz. With the help of figure 2 transmit frequencies ranging from 1.6 to 2.5 MHz were selected for the in-vitro experiments.

From figure 8.2 it can be seen that gaining sensitivity by increasing the transmit frequency will result in a decrease of receive sensitivity for the harmonic backscatter signal and visa versa. This is one of the effects in play when optimizing the transmit frequency.

To calculate the CTR for different frequencies the RF-data from the contrast and tissue ROI were selected as shown in figure 8.3A. The backscattered frequency spectra from the two ROI were calculated of which an example is shown in figure 8.3B. Subtraction of the two spectra yielded the CTR as function of frequency (see figure 8.3C, solid line). The highest CTR was found close to the second harmonic of the transmitted frequency. To reduce influence of noise a 1 MHz moving window average of the CTR curve was calculated before maximum CTR levels were extracted (see figure 8.3C, dashed line).

From figure 8.3C it can be seen that the CTR of the second harmonic is 8 dB higher than at the fundamental frequency. An excitation frequency of 1.74 MHz was found to give the highest harmonic CTR (see figure 8.3A and D[1]).

Pulse length variations at the optimal excitation frequency of 1.74 MHz were evaluated from 50 to 400 kPa derated peak negative pressure. From figure 8.4 it can be seen that at low pressures there is no significant difference between the CTR levels of 1.5 and 2.5 cycles pulse lengths. At moderate and high pressures, however, there is an intrinsic CTR increase of approximately 2 dB for a pulse length of 2.5 cycles.

For the optimal transmit settings the receive filter was configured with a center frequency of 3.6 MHz and a bandwidth of 1.3 MHz giving the maximum harmonic amplitude (see figure 3B and C).

Figure 8.5[1] shows the lifetime of contrast at room temperature and 36 °C. It is clearly demonstrated that the life time is effected at body temperature. A limited lifetime does not add to a constant contrast concentration which is required for an optimal 3D recording.

Figure 8.6 shows an example of left ventricular harmonic B-mode images with and without contrast. In the image without contrast especially the api-

[1]Not included in the original publications.

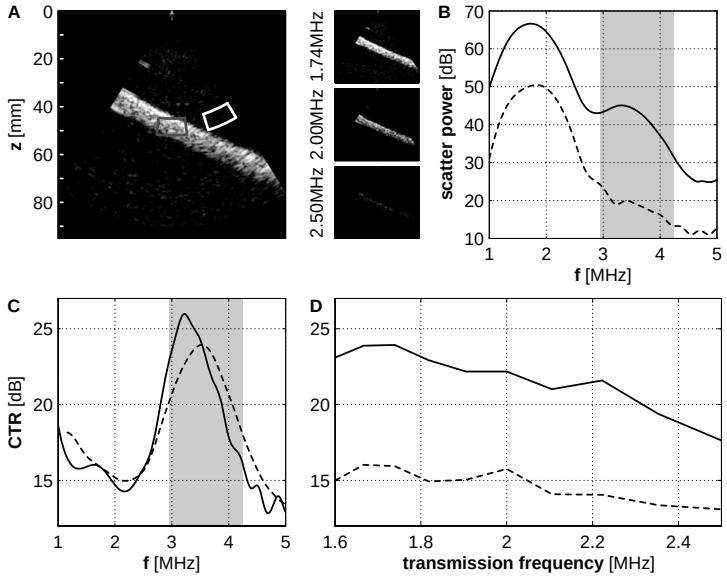

Figure 8.3: ***A.*** *B-mode image from the tissue-mimicking phantom with contrast in the flow area showing the regions of interest used for the power spectra calculations. Contrast harmonic B-mode images at different transmit frequencies are shown, revealing the optimal excitation frequency at 1.74 MHz.* ***B.*** *Power spectra from the tissue (dashed line) and contrast (solid line) region.* ***C.*** *The difference of both power spectra defined as the CTR. A 1 MHz window average of the CTR curve (dashed line) was used before maximum CTR levels were extracted. The receive filter settings for the optimal excitation frequency is indicated with a shaded area in panel B and C.* ***D.*** *Transmission frequency vs. CTR, fundamental (dashed line) and harmonic (solid line).*

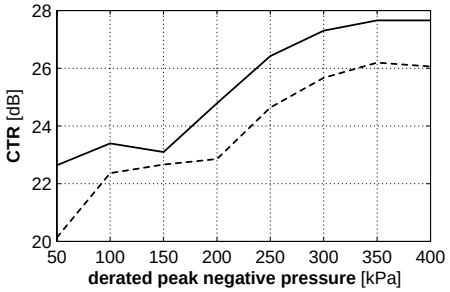

Figure 8.4: *Harmonic CTR levels as function of the derated peak negative pressure for pulse lengths of 1.5 cycles (dashed line) and 2.5 cycles (solid line).*

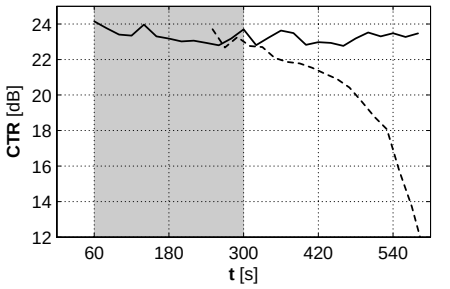

Figure 8.5: *Optison lifetime at room temperature and 36 °C. The shaded area indicates the approximate time window of a 3D recording.*

cal segment shows a vague delineation of the endocardial border while this segment is clearly visualized in the image with contrast. The same apical delineation improvement was observed by Kasprzak *et al.* [1999]. Other studies involving 3D harmonic contrast imaging report promising reconstructions of kidney and liver vascularities [Forsberg 2002, Moriyasu 2002].

Successful contrast harmonic patient recordings were obtained. Figure 8.7 shows an example from a 75 years old postoperative patient. LV-reconstructions from the end diastolic and end systolic volume (figure 8.7A and B) are shown along with the LV volume-time curves of the tissue harmonic and contrast harmonic recording of this particular patient. Although the time-volume curves only show small differences the tracing effort for the contrast harmonic recording was remarkably lower due to an improved delineation of the endocardial border.

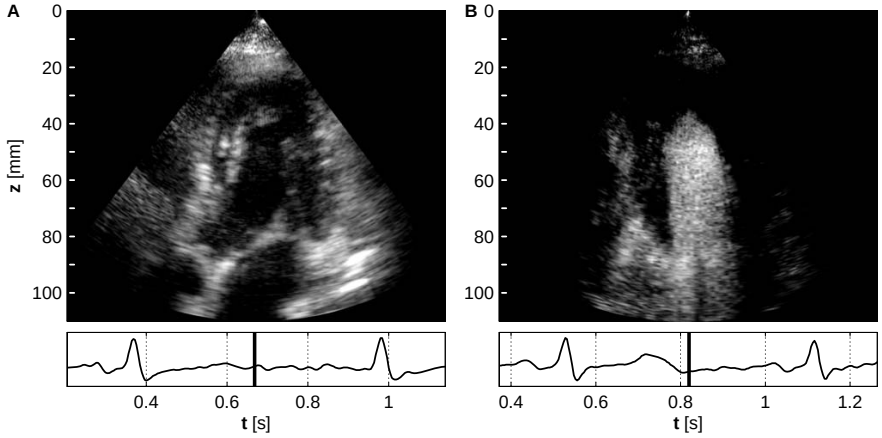

Figure 8.6: *Harmonic B-mode images from the FRU-transducer without (left) and with contrast (right). In the recording with contrast the delineation of the apical segments is clearly improved.*

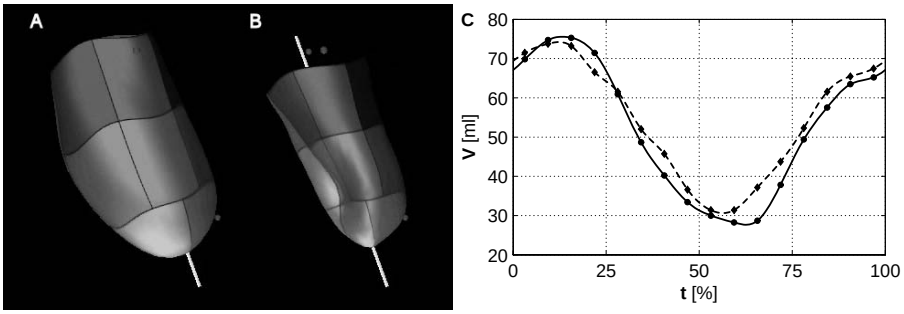

Figure 8.7: ***A** and **B.** End diastolic (panel A) and end systolic (panel B) LV-reconstructions from a contrast harmonic patient recording. **C.** The time-volume curves obtained from the tissue harmonic recording (dashed line and diamonds) and the contrast harmonic recording (solid line and circles) of the same patient.*

In the preceding section accurate clinical volume measurements from harmonic contrast recordings of the FRU-transducer have been proven feasible. Currently, the only commercial 3D echo system for cardiac imaging with harmonic capabilities is the Sonos 7500 with its x4 xMATRIX transducer from Philips. However, no record has been found in the literature on its harmonic contrast imaging performance yet.

8.4 Conclusion and Future

Many advantages of 3D echo have been reported throughout the last decade. The introduction of 3D echo in the daily clinical practice has however only recently started. To make 3D echo a mature and widely spread technique more modalities other than fundamental and harmonic B-mode imaging have to be added. The results presented in this chapter show the feasibility of 3D harmonic contrast imaging and improved border delineation when used in combination with harmonic imaging. As reported by Bouakaz et al. further improvements on 3D contrast imaging can be expected when harmonics higher than the second harmonic will be made available for imaging [Bouakaz 2004]. Further investigations are required in a larger patient population to determine the improvement with 3D-CHI compared to other techniques like MRI. By then it can be investigated whether the improved delineation of the endocardial border from harmonic contrast recordings is beneficial for (semi)-automated border tracing algorithms.

Acknowledgements

The authors would like to thank W.J. van Alphen, L. Bekkering and F.C. van Egmond for their significant contribution in the construction of the fast rotating ultrasound transducer.

Chapter 9

Guiding and Optimization of Resynchronization Therapy with Segmental Volume-Time Curves: a Feasibility Study

IJsselmeer (somewhere between Volendam and Muiden), April 26th, 2006: *A worthy photograph to conclude this dissertation, off to new horizons. I myself, at the helm during one of the rememberable ICIN outings.*

Resynchronization therapy for heart failure provides the greatest hemodynamic benefit when applied to the most delayed left ventricular (LV) site. Currently, the ideal LV pacing site is selected according to acute invasive hemodynamic assessment and / or tissue Doppler imaging. The objective of this study is to assess a new approach for guiding and hemodynamic optimization of resynchronization therapy, using three dimensional (3D) transthoracic echocardiography.

A total of 16 patients with advanced heart failure and an implanted biventricular pacemaker were included in this study. Transthoracic apical LV images at equidistant intervals were obtained using a prototype, fast-rotating second harmonic transducer to reconstruct 3D LV datasets during sinus rhythm (SR), right ventricular (RV) apical and biventricular pacing mode. A semi-automated contour analysis system (4D LV Analysis, TomTec Imaging Systems, Unterschleißheim, Germany) was used for segmental wall motion analysis and identification of the most delayed contracting segment and calculation of global LV function.

Data acquisition duration was 10 seconds and analyzable 3D images were obtained in 12 patients. Of these patients, data during SR were available in 9 and during biventricular pacing in 11. The greatest contraction delay during SR was found in the anterior and antero-septal segments in five of nine patients. Biventricular pacing resulted in reduction of the contraction delay in seven of eight patients. The global LV function did not change significantly.

3D echocardiography with appropriate analytic software allows detection of the most delayed LV contracting segment and can be used to select the optimal pacing site during resynchronization therapy.

Based on:

© 2004 Elsevier. Reprinted, with permission, from: **Krenning, B.J.**, T. Szili-Torok, M.M. Voormolen, D.A.M.J. Theuns, L.J. Jordaens, C.T. Lancée, N. de Jong, A.F.W. van der Steen, F.J. ten Cate and J.R.T.C. Roelandt. Guiding and Optimization of Resynchronization Therapy with Dynamic Three-Dimensional Echocardiography and Segmental Volume-Time Curves: a Feasibility Study. *The European Journal of Heart Failure*, 6(5):619–625, 2004.

9.1 Introduction

Delayed intraventricular depolarization leads to dyssynchrony of ventricular contraction and worsens left ventricle (LV) dysfunction [Grines 1989, Kerwin 2000, Shamim 1999, Xiao 1991]. Resynchronization by simultaneous electrical stimulation of both ventricles significantly improves hemodynamics, resulting in increased exercise tolerance and hence quality of life [Mascioli 2002, Abraham 2002b, Cazeau 2001, Daubert 1998, Gras 1998, Leclercq 1998, 2000, Kuhlkamp 2002]. Reduction in morbidity and mortality awaits confirmation from ongoing large-scale studies [Mascioli 2002, Abraham 2002a]. Recent data indicate that biventricular pacing provides the greatest hemodynamic benefit when applied to the LV segment with the most delayed contraction [Ansalone 2002]. Tissue Doppler imaging (TDI) is currently used to identify the most delayed contraction site before the implantation of a resynchronization device [Ansalone 2002, Sogaard 2002, Bax 2003]. This method cannot be used online and the assessment of the hemodynamic effects requires additional studies. It has been demonstrated in previous studies that volume-time curves (VTCs) provide quantitative information on LV performance [Zeidan 2003, Soldo 1994]. The aim of the present study was to test the feasibility of 3D echocardiographic VTCs for determining the optimal pacing site. This allows simultaneous hemodynamic evaluation by measuring global LV function.

9.2 Methods

9.2.1 Study Patient

We studied 16 patients with severe heart failure and a permanent biventricular pacemaker. All patients gave informed consent. Patient characteristics are listed in table 9.1. The diagnosis of dilated cardiomyopathy was established according to the classification of cardiomyopathy published previously [Kuhn 1996]. Criteria for biventricular pacing were severe heart failure (NYHA II-IV) and dilated cardiomyopathy associated with complete left bundle branch block and a QRS duration of >125 ms. The LV pacing lead was positioned in the coronary sinus and the right atrial and right ventricular (RV) leads in standard locations.

Three acquisitions for 3D reconstruction were performed as follows: The first acquisition was performed in the biventricular pacing mode and the second after the pacemaker was reprogrammed for RV pacing. In patients with intact atrio-ventricular conduction and sinus rhythm (SR), the pacemaker

Figure 9.1: *Latest prototype of the continuous fast-rotating transducer.*

was reprogrammed in order to perform acquisitions during SR. In every patient, the pacemaker was finally reset to the original settings. Acquisitions were performed 5 minutes after the pacing mode was switched. Data analysis was performed off-line for this feasibility study.

9.2.2 Image Acquisition

We used a prototype transthoracic, fast-rotating ultrasound transducer for 3D echocardiographic image acquisition [Djoa 2000] (figure 9.1), which is connected to a commercially available ultrasound system (Vivid FiVe, GE Vingmed Ultrasound, Horton, Norway). The 64-element transducer array has a center frequency of 3 MHz and second harmonic capabilities [Voormolen 2006]. It continuously rotates inside the transducer assembly at a maximum speed of 8 rps. The frame rate of the ultrasound system is 100 frames per second. The typical acquisition time is 10 seconds during a single end-expiratory breath hold. Patients were studied in the left lateral decubitus position with the transducer in the apical position and the image plane rotating around the LV long axis. The depth setting was adjusted to visualize the entire LVand part of the left atrium. Gain and power settings were optimised for endocardial border visualization. The ECG signal was simultaneously recorded for 3D reconstruction.

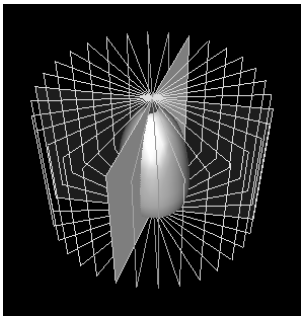

Figure 9.2: *From each dynamic 3D dataset, up to 20 cross-sectional images can be selected. The orientation of each cross-section is shown.*

9.2.3 Image Processing

Data are transferred via a network connection to a dedicated workstation for processing and analysis. With self-developed software, using MatLab (The MathWorks, Natick, Massachusetts, USA), the original 2D images are post-processed by placing them in their correct spatial and temporal (ECG reference) position using multi beat data fusion [Lancée 2000]. The cardiac cycle is divided in 12 equal intervals, which allows to create 12 3D datasets. Due to the continuous rotation of the transducer array, the original 2D images have a curved shape. However, these are not suited for automated contour analysis with currently available software. Therefore, 20 equidistant plane cross-sectional images (9° interval) are re-sampled from these 12 datasets and used for further analysis.

9.2.4 Image Analysis

All the 20 cross-sectional images re-sampled from each of the 12 datasets are subsequently imported into the TomTec 4D LV Analysis software (TomTec Imaging Systems, Unterschleißheim, Germany) and displayed (figure 9.2). Their orientation in 3D space is determined by marking the mitral valve, aortic root and apex as landmarks. An elliptical model is placed over one of the images of each cross-sectional position. After this, the software automatically performs endocardial border detection in all images of each cross-sectional position in the 12 datasets. A spatio-temporal spline model is used to generate smooth contours for both the temporal and spatial domain. The long axis of the ventricle is calculated from the center of the mitral annulus to the most distant point in the ventricle, which is the apex.

Two experienced investigators verified and corrected the results from the automated border detection where necessary. This was done blinded, without

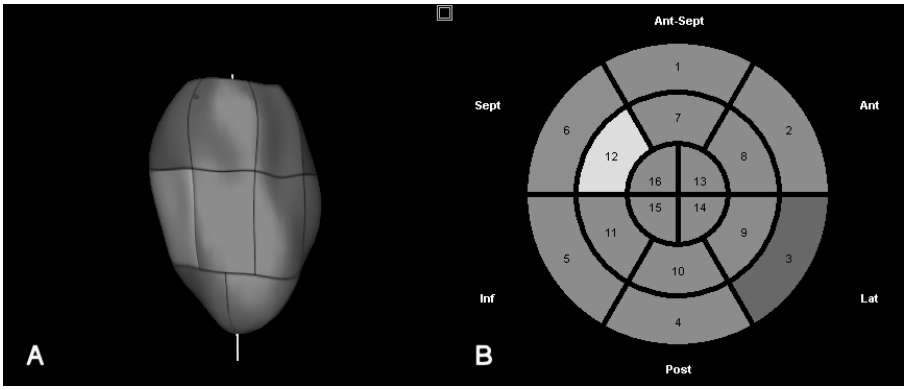

Figure 9.3: ***A.*** *Three dimensional reconstruction of the LV.* ***B.*** *Bulls-eye view according to which the endocardial surface is subdivided in 16 colour-coded segments.*

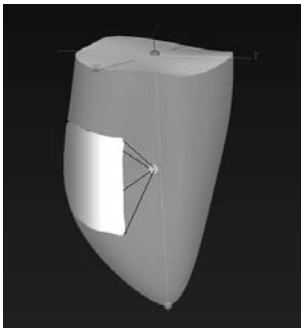

Figure 9.4: *A segmental volume represents the pyramidal volume of a segment to the center of gravity. The long axis of the ventricle is calculated from the center of the mitral annulus to the apex.*

knowledge of the pacing mode for each analysis. The papillary muscles within the LV cavity are not taken into account for the definition of the contour. After completion of the endocardial border tracing, the program performs a dynamic surface rendered endocardial reconstruction of the LV (figure 9.3A). For each pacing mode, a VTC is plotted from which global LV end-diastolic volume (LVEDV), end-systolic volume (LVESV) and ejection fraction (EF) are calculated applying Gaussian quadrature formulas.

The LV endocardial surface is subdivided in 16 segments, which are colour coded for orientation (figure 9.3B). A segmental volume represents the pyramidal volume of a segment to the center of gravity (figure 9.4). The volume change of a segment over the cardiac cycle is plotted in a VTC (figure 9.5), in which time is defined as percentage of the total cardiac cycle. The end-systolic

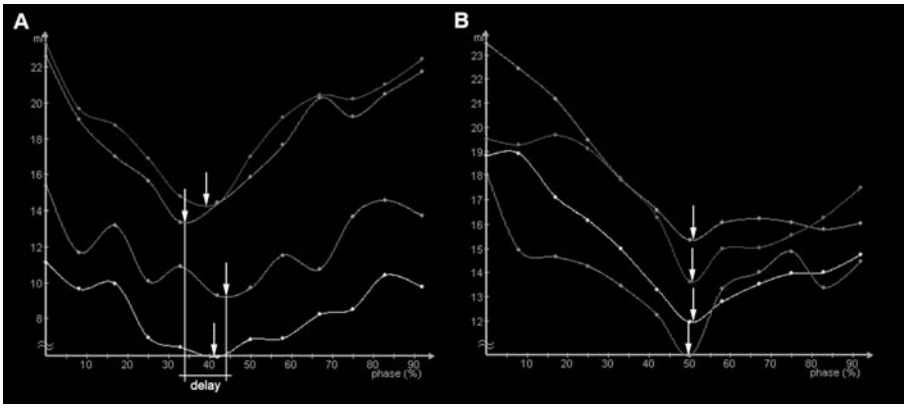

Figure 9.5: *Example of volume-time curves of four different segments. During sinus rhythm, each segment completes myocardial contraction at a different moment (indicated with an arrow for every segment), causing LV dyssynchrony.* ***A.*** *From the various delays, the largest delay is annotated.* ***B.*** *During biventricular pacing, synchrony in segmental contraction is present.*

moment, at which a segment has completed maximal myocardial contraction, is represented by the nadir of the segmental volume curve. This moment was extracted from the VTC for every segment in every pacing mode. The difference in time to maximal myocardial contraction between segments was used to assess regional mechanical delay and a measure of segmental dyssynergy. From the VTC that represents segmental volume changes in SR, the first contracting segment and the most delayed segment were identified. The delay in contraction was calculated as the difference in time to maximal contraction between these segments and is expressed as percentage of the total cardiac cycle. Using the RR-interval, this was re-calculated in milliseconds. When a segment is hypo- or akinetic, which we defined as a segmental volume change during any part of the cardiac cycle of less then 20 %, the segment is not included. In both biventricular and RV pacing mode, the most delayed segment is determined and the delay between this segment and the first contracting segment calculated.

9.2.5 Statistical Analysis

Data are presented as mean ± SD. 3D measurements of LV volume were calculated by the analysis software after completion of the endocardial border tracing. To assess accuracy, analysis of VTCs was performed by two ob-

servers and analyzed by linear regression and a limits-of-agreement analysis, expressed as the mean difference and 2SD of the difference between the measurements of the two observers. To determine whether the difference in the values between the two observers and between pacing modes was statistically significant, a paired t-test was performed. A probability level of $p<0.05$ was considered significant.

9.3 Results

Of the 16 patients, four were excluded from analysis because of inadequate echocardiographic image quality for faithful automated analysis. In 3 of the remaining 12 patients, no spontaneous sinus rhythm was present and therefore only acquisitions in biventricular and RV pacing mode were performed. In one patient, we did not perform an acquisition in biventricular pacing mode because of LV lead displacement.

9.3.1 Global LV Function

The mean ejection fraction of all patients before implantation, by equilibrium radionuclide angiography, was 24 ± 7 %. During sinus rhythm, the mean LVEDV, LVESV and LVEF derived from the VTC were 294 ± 85 ml, 230 ± 94 ml and 24 ± 12 %, respectively. During RV pacing, these values were 291 ± 97 ml, 225 ± 81 ml and 23 ± 6 % and during biventricular pacing, 282 ± 94 ml, 226 ± 86 ml and 21 ± 6 %, respectively. No significant difference was present between these values.

9.3.2 Dyssynchrony

The mean heart rate during SR was 69 ± 7 bpm, during biventricular pacing 73 ± 9 bpm and during RV pacing 74 ± 9 bpm. No significant difference was present between these values. In six of eight patients, heart rate was less during SR compared to biventricular pacing. Table 9.1 shows the most delayed segment for every pacing mode and the delay between the first contracting and most delayed segment. The mean delay was 147 ± 80 ms during SR, 103 ± 34 ms during biventricular pacing ($p<0.01$; SR vs. biventricular pacing) and 158 ± 78 ms during RV pacing ($p<0.01$; RV vs. biventricular pacing). In five of nine patients, the anterior or antero-septal segment was most delayed during SR. Biventricular pacing resulted in reduction of the contraction delay

Table 9.1: *Patient characteristics and results for contraction delay measurements.*

patient	age	NYHA class	type of CM	pacing site	FCS	SR		BiV		RV	
						MDS	delay (ms)	MDS	delay (ms)	MDS	delay (ms)
1	76	III	2	ant	16	9	64	1	69	9	61
2	56	III	2	pcv	7	10	20	NA	NA	3	50
3	56	II	1	plcv	16	2	177	8	80	2	167
4	71	II	2	lcv	11	7	200	4	143	8	137
5	64	III	1	plcv	8[1]	NA	NA	11	130	8	230
6	68	III	2	plcv	3[1]	NA	NA	6	261	6	198
7	67	II	2	plcv	10[1]	NA	NA	3	53	9	45
8	62	III	1	plcv	6	2	68	6	66	3	205
9	63	III	1	plcv	12	7	256	3	128	14	240
10	59	III	1	pcv	9	11	221	11	113	11	90
11	61	III	1	plcv	6	9	140	5	88	8	248
12	53	II	1	ant	12	1	182	11	108	2	228

NYHA: New York Heart Association; CM: cardiomyopathy (1=dilated cardiomyopathy, 2=ischemic cardiomyopathy); FCS: first contracting segment; SR: sinus rhythm; BiV: biventricular pacing; RV: right ventricular pacing; MDS: most delayed segment; ant: anterior; lcv: lateral cardiac vein; pcv: posterior cardiac vein; plcv: postero-lateral cardiac vein; [1]: during biventricular pacing; NA: not applicable.

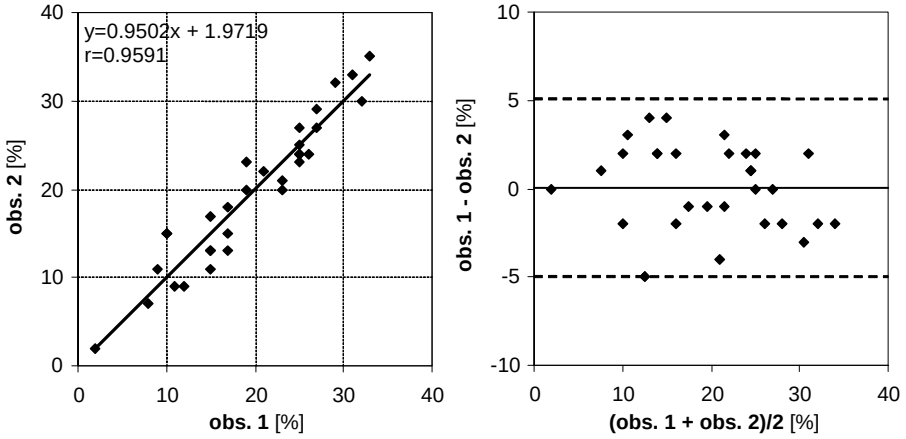

Figure 9.6: *Left, regression analysis for measurement of delay between the two most delayed segments by two observers. Right*[1]*, Bland-Altman plot of the difference in delay between the observers.*

in seven patients, compared to SR. Also, in six patients, the contraction delay was less during biventricular pacing compared to RV pacing.

9.3.3 Interobserver Agreement

Linear regression analysis indicated a good correlation (r=0.96) between measurements of delay in contraction between the first contracting segment and the most delayed site by two observers (figure 9.6). The standard error of estimate was 2.42 %. The limits-of-agreement analysis demonstrated a small mean difference (0.03 ± 2.50 %) between measurements. A paired t-test indicated no significant mean difference between the two observers.

9.4 Discussion

This study shows that transthoracic dynamic 3D echocardiography performed with a fast-rotating transducer and combined with semi-automated contour analysis allows to identify LV segments with dyssynchrony together with

[1]Not included in the original publication.

hemodynamic evaluation. Our data indicate that this method is feasible for the selection of the optimal pacing site during resynchronization therapy.

9.4.1 Rationale for Measuring Mechanical Delay in Patients Undergoing Resynchronization Device Implantation

A delay in intraventricular conduction leads to dyssynchrony of ventricular contraction which can be corrected by biventricular pacing and subsequently improve hemodynamics. and consequently exercise tolerance and quality of life in patients with severe heart failure. Large-scale trials are ongoing to study long-term effects including morbidity and mortality [Mascioli 2002, Abraham 2002a, Lozano 2000]. However, a substantial proportion of the patients does not show improvement. This may be partly related to methodological reasons. Indeed, a prolonged QRS complex cannot quantify the degree of dyssynchrony. Clearly, biventricular pacing provides the most benefit when applied to the segment of the LV that is most delayed in contraction. Therefore pacing should be applied to this site but it should be noted that this site will not always be approachable during implantation. While long-term studies showed improvement of LVEF with biventricular pacing, this could not be observed in this study. Possibly, other regulating factors counterbalance the hemodynamic effect of changing pacemaker programming.

9.4.2 The Role of Improved Imaging Techniques to Guide and Evaluate Biventricular Pacing

Echocardiography has an important role in the evaluation of patients with mechanical dyssynchrony before biventricular pacemaker implantation [Abraham 2000, Pitzalis 2002]. Sogaard *et al.* [2001] previously used 3D echocardiography for hemodynamic assessment in patients before and after biventricular pacemaker implantation. Currently, TDI is most often used as a guiding tool for the implantation [Sogaard 2002, Bax 2003] and is useful for identifying LV myocardial contraction dyssynchrony at discrete points in patients after ventricular resynchronization [Ansalone 2002]. It is suggested that TDI analysis could serve in the future both as a tool for pre-implantation assessment and as a guide to select the most optimal pacing site. However, this approach requires a lengthy echo study and analysis before the implantation, while only the longitudinal function in the basal and mid-segments are studied. Also other diagnostic modalities, such as MRI [Soldo 1994] and gated-SPECT [Germano 1997], can be used to create volume-time curves and assess regional

wall motion. However, MRI cannot be used after device implantation because of its magnetic properties. 3D echocardiography with appropriate software for segmental wall motion analysis allows to determine dyssynchrony between all segments. Obviously, expressing the delay is an issue and requires standardization in the near future. Currently, several parameters are used for describing intra- and interventricular delays during the heart cycle. Using our method, the delay is expressed in relative units (as percentage of the total heart cycle). Actually, this method allows demonstration of shortening of the diastolic period when the heart rate increases. This may play a role in an adverse outcome of this patient population. This phenomenon is clearly demonstrated in figure 9.5. In this particular example, the heart rate in sinus rhythm was lower than in a paced rhythm. This results in relatively longer diastolic period. As the heart rate increases, the systolic period shortens relatively less than the diastolic period, meaning that the systolic periods are almost identical in absolute units (ms), but the diastolic periods become different. Additionally, the position of the RV lead has a significant impact on the LV conduction pattern. Therefore, the optimal technique should provide the information during the implantation procedure and additional hemodynamic data. This is possible with a fast-rotating ultrasound transducer and appropriate software for analysis.

9.4.3 Limitations of the Study

We used prototype equipment for this proof-of-principle study requiring further refinements. The post-processing time to obtain a 3D dataset must be shortened to make this technique a practical guiding tool during the intervention. The semi-automated border detection algorithms are user-friendly, but manual interaction remains often a necessity. Real-time 3D echocardiography using a matrix transducer is also appropriate for acquisition of 3D datasets and optimisation of resynchronization therapy, using the same border detection and analytic software. Most experience is with a system developed at Duke University (Durham, North Carolina, USA) [Sheikh 1991], which makes use of a sparse matrix phased array transducer to scan a $60° \times 60°$ pyramidal volume using parallel processing technology. More recently, Philips Medical Systems has introduced a matrix phased-array transducer with 3000 transmit / receive elements. Development of new border detection algorithms along with technological improvements of 3D echocardiography should be able to improve the accuracy of semi-automated border tracing and eventually provide automatic, even on-line, data analysis in the future. This was not a prospective study and the patients studied had already their resynchronization device

in place. Therefore, we could only study the feasibility of the method and whether dyssynchrony in segmental contraction could be measured. During image acquisition, a 10 seconds breath hold was required. We did not find this inconvenient in our patient population with advanced heart failure.

9.5 Conclusion

3D echocardiography is a feasible approach for determination of the most delayed LV site with the additional option to assess hemodynamic information, such as LVEDV, LVESV and EF. This preliminary data suggests that 3D echocardiography can be used for selection of the most optimal pacing site before and during resynchronization device implantation. Further studies with prospective study design are required to validate this data against other techniques, e.g. TDI.

General Discussion

In the preceding chapters the considerations, implementation, validation and clinical application of a unique concept for harmonic 3D echocardiography is described. In the following paragraphs the general findings of each chapter will be summarized and my (future) perspective on related issues will be discussed.

Simulated harmonic acoustic beams Starting with chapter 1 it has been shown that the harmonic profiles of steered nonlinear acoustic beams from apertures with arbitrary geometry can be accurately predicted with the presented two-stage 3D-KZK method. The validity of the method was verified with a theoretical benchmark in chapter 1 and phased array experiments in chapter 2. In chapter 2 it was also demonstrated that grating lobes are effectively suppressed by harmonic imaging. For phased array and matrix transducers the existence of grating lobes and their harmonic levels can be an important design consideration. With its relatively short computation time the two-stage 3D-KZK method provides a useful tool for an efficient design of harmonic medical transducers. It is also possible to extend the two-stage 3D-KZK method with a scattering model to obtain simulated harmonic images from phased array and matrix transducers. Another field that can now be efficiently explored is that of complex excitation sequences that assign signals of different frequency, amplitude and length to the individual elements.

3D harmonic echocardiography The second harmonic amplitude is related to the square of the fundamental amplitude. A higher fundamental amplitude will result in a quadratic increase of the second harmonic amplitude. For harmonic imaging it is therefore advantageous to maintain a high amplitude in the transmitted fundamental field. Especially for matrix transducers, for which a broad transmission beam is combined with multiple receive beams, this requirement proves to be counterproductive. To avoid violation of the safety guidelines the amplitude close to the transducer's surface, where the transmission beam is at its narrowest, is limited. This results in a suboptimal fundamental amplitude for harmonic imaging in the remainder of the transmitted beam. The lower level of harmonics in the received signals will put a heavy burden on the required sensitivity and signal-to-noise ratio while the small element size is already a challenge regarding these properties. Suboptimal image quality has been reported for second generation matrix transducers when it comes to harmonic imaging (see chapter 3). The fast rotating ultrasound (FRU)-transducer, presented in chapter 3, combines the state-of-the-art harmonic properties of a standard phased array transducer with the acquisi-

Figure d.1: *The first prototype of the fast rotating transoesophageal transducer. Courtesy of Kyriakos Nathanail.*

tion time of a matrix transducer. In addition it provides a cost effective alternative and it is easily integrated into existing 2D based echo systems. These advantages have not only resulted in the FRU-transducer for transthoracic echocardiography (TTE) but also a transoesophageal (TEE) version, which is currently under investigation (see figure d.1).

Left ventricular volume quantification Good agreement was found in chapter 4 for left ventricular (LV) volumes derived from FRU-transducer recordings in comparison with magnetic resonance imaging (MRI) results. The commercial software that was used for this study, the now widely used TomTec 4D LV Analysis, required plane images as an input to its quantification algorithm. As a consequence, images had to be resliced from the 3D datasets of the recorded, high resolution 2D harmonic images. In the reslicing procedure part of this resolution is lost which would have been beneficial for the

incorporated semiautomatic tracing algorithm. To overcome this problem an alternative quantification tool was developed, described in chapter 5, which is capable of reading the recorded 2D images from the FRU-transducer. In addition, this method requires minimal user interaction which is an important condition for clinical acceptation of 3D echocardiographic LV volume measurement. As both software tools presented in chapter 4 and 5 require a number of cross-sectional images for the quantification of the LV volume, it is not more than logical to investigate the exact number of images required for accurate LV volume quantification. Chapter 6 shows that 8 random equiangular long-axis images are required for this purpose. More surprisingly, it is also demonstrated that as few as 4 long-axis images can be sufficient when the orientation of the images in respect to the eccentricity of the endocardial border is taken into account. When only 8 images are needed the possibility of LV volume measurement with data from a single cardiac cycle is feasible with the FRU-transducer. I regret that this unique application of the FRU-transducer could not be demonstrated within the scope of this dissertation.

The number of publications on the seemingly simple problem of LV volume measurement is out of proportion. On one hand this is due to the fact that most studies use a falls 'golden standard' as reference. The lack of a good reference technique for the measurement of the time-volume curve of a beating heart leaves room for an endless discussion about who is wrong and who is right. A bigger problem is the weak definition of the endocardial border due to the trabeculae. An additional complicating factor is the different manifestation of these trabeculae in the end diastolic and end systolic phase of the cardiac cycle (see chapter 6 and figure d.2). When comparing imaging techniques that are sensitive for different properties of biological tissue the situation becomes even more complicated (see chapter 6). What is needed to determine the real accuracies of the different imaging techniques is a good dynamic model of the left ventricle, including the trabeculae. Most likely this will be in the form of an excised human heart in a well controlled setup which is both complex and expensive. If my next position will not provide the opportunities to do this myself, I expect that at least one of my direct co-workers will shed some light on this issue.

Chapter 7 gives a good example of the flexibility of echocardiography. Where this is much more complex for alternative imaging techniques, such as CT and MRI, echography can be performed at the bedside, during treatment or even during intervention. In general diagnostic ultrasound imaging is performed under very comfortable circumstances for the patient. For haemodialisys the application of 3D-echocardiography opens the way for the guidance of treatment strategies that aim for hypotension prevention.

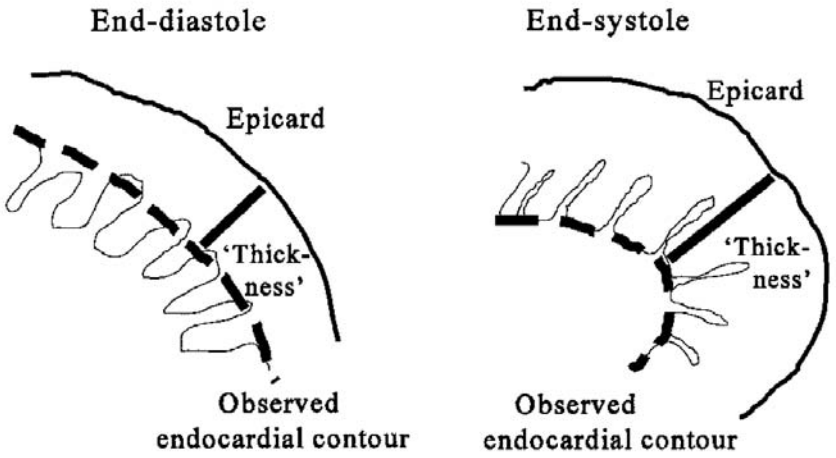

Figure d.2: *"At end-diastole many individual trabeculae are difficult to trace due to their small size, and the trabecular zone is thus largely excluded by an observer who traces the endocardial border. Also automated routines often tend to ignore the trabeculae due to the poor contrast between trabecular zone and blood pool. During systole however, the individual trabeculae will join to form a more compact compartment, clearly different from the blood pool. Thus at end-systole, the observed contour will now include the trabeculae, and the apparent 'thickness' is enlarged in part by these joined trabeculae."* © *2000 Taylor & Francis. Reprinted, with permission, from Marcus* et al. *[2000].*

Contrast imaging The use of ultrasonic contrast agents adds a new range of applications to medical ultrasound. In combination with diagnostic imaging it can provide insight in the perfusion of organs and has the potential to improve the endocardial border delineation, which might be beneficial for (full) automatic quantification. Chapter 8 demonstrates the advantages of harmonic contrast imaging in general and for 3D echocardiography with the FRU-transducer in specific. Machine settings for the FRU-transducer are optimized for this application and initial experience with 3D harmonic contrast echocardiography is obtained. Although the use of contrast agents looks very promising, successful application requires a skilled operator. The required concentration varies from patient to patient and a too high concentration leads to increased attenuation of the ultrasound. For LV opacification an increased attenuation results in limited penetration and suboptimal visualization of the

mitral valve and the lateral wall. In addition, the relatively long acquisition of a 3D recording, compared to 2D imaging, requires a constant concentration over the acquisition time. The development of application specific contrast agents could therefore contribute to the ease of use. More sensitive contrast imaging techniques, like super harmonic imaging (see chapter 8), could also improve the application of contrast agents for LV volume quantification.

Parametric imaging Ultimately, chapter 9 gives an early example of what has become a very popular way of presenting advanced quantification of 3D echocardiographic recordings, also known as *parametric imaging*. The feasibility of regional wall motion assessment is demonstrated for the guidance of resynchronization therapy. Current implementations of the same principle display the LV contraction with higher resolution and in a so called *color coded bulls-eye plot*. The lack of a good spatial reference can however result in severe artefacts. Motion of facing regions can interfere with each others result. The intuitive presentation tends to hide this shortcoming of the algorithm and the available literature fails to mention this limitation with sufficient detail. In general, echocardiographic quantification tools are sometimes introduced without a thorough validation and the understanding of the underlying algorithms among its users is often limited. The manufacturers of these software tools leave the responsibility of its diagnostic use to the cardiologists. As the algorithms for echocardiographic quantification become more and more complex this problem could intensify and lead to undesirable situations. 3D echocardiographic recordings contain a vast amount of information and it is clear that we are just facing the beginning of its clinical use. Many quantification tools that will facilitate our access to a variate of parameters are yet to come, hopefully *with* a keen understanding of their limitations.

3D stress echocardiography Another advanced application, not included in this dissertation, that can already count on the interest of several research groups around the world, is 3D stress echocardiography. Big challenge for this application is the time resolution of the currently available 3D echo systems. Extending the acquisition over several cardiac cycles can not be stretched unlimited due to a reduced stability of the cardiac rhythm and function under peak stress conditions. The solution to this problem is not only expected from technological improvement of echo systems and transducers but also from more advanced image processing algorithms. The vast majority of the currently developed algorithms fuse the results of individually analyzed time samples. Big improvements can be expected with algorithms that can address

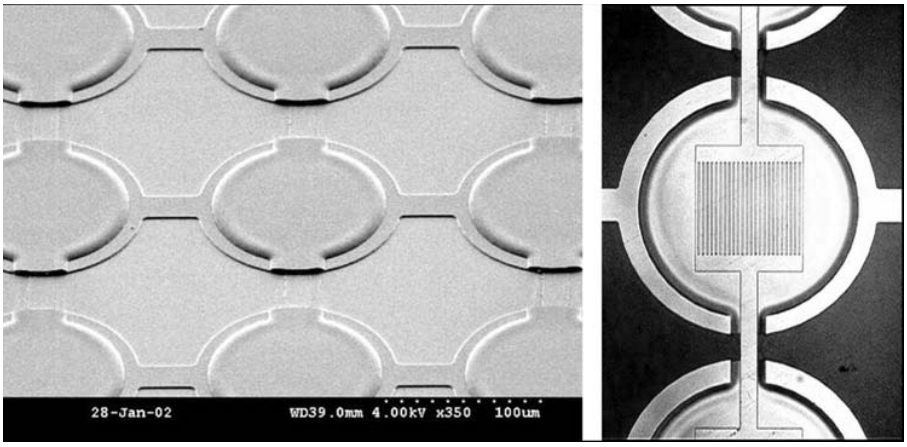

Figure d.3: *"The picture on the left shows the scanning electron microscope image of part of a CMUT with aluminum membranes fabricated on quartz substrate for integrated optical detection. The membranes are 100 micrometer in diameter and are suspended 2.5 micrometer above the substrate. The picture on the right is taken from the backside, through the transparent quartz wafer and shows the back electrode of one of the CMUT membranes. The aluminum electrode is shaped in the form of a diffraction grating with 4 micrometer period. The reflected diffraction orders enable optical interferometric detection of the membrane displacement."* © *2003 IEEE. Reprinted, with permission, from Hall et al. [2003].*

all image lines in a recording, with their 4D (three spatial dimensions and time) position, as a whole.

Transducer design With the recent introduction of single crystal materials for phased array and matrix transducer the domination of PZT for this purpose is finally broken, after decades. A real revolution in transducer design is more likely to come from *capacitive micromachined ultrasound transducers* CMUT (see figure d.3). If the sensitivity problems, that currently prevent a wide application of this technique, can be solved, it will open the door to a whole new approach in transducer design. The flexibility in transducer and element geometry (through grouping of several CMUT) and the use of multiple frequencies (not only by exploitation of the large bandwidth) will open many new possibilities for multiple frequency imaging methods and formerly unrealistic transducer shapes.

3D visualization Conventional (2D) computer displays lack the depth perception for optimal visualization of 3D echocardiographic recordings. Although fast rendering techniques have improved the 3D perception of the so called *dynamic surgical view*, quantification is still assisted by 2D images. With the increased availability of virtual reality facilities and affordable 3D displays, new tracing interfaces should be developed that allow for quantification in 3D or even 4D space.

Appendix A

Rotation Speed Optimization

The sampling of the rotation angle in a fused cardiac cycle, when using multi-beat fusion is determined by four parameters: the rotation speed $f_{Rotation}$, the heart rate, the frame rate f_{Frame}, and the segmentation of the cardiac cycle. To determine an optimized rotation speed, we first look for a rotation speed from which the frames of corresponding and consecutive segments fill up the rotation angle as taken from a continuous sequence of frames. For a given heart rate, frame rate, and number of segments, we can calculate the average number of frames within each cardiac cycle $N_{F/C}$ and the average number of frames within each segment $N_{F/S}$. With n being the number of complete rotations covered within the time between two corresponding and consecutive cardiac segments, we can calculate candidate rotation speeds $f_{Candidate}$ for our solution with the following formula:

$$f_{Candidate} = \frac{n\ f_{Frame}}{[N_{F/C}] - [N_{F/S}]}, \quad 4 \leq f_{Candidate} \leq 8Hz, \quad n \in \{1, 2, 3, \cdots\} \tag{A.1}$$

From the range of possible rotation speeds and the typical frame rate of approximately 100 fps, it appears that an adequate sampling of the rotation angle can be reached when a number of rotations are merged (see also figure 3.5). When, for instance, three rotations are merged, the first frame of the second rotation should start at exactly one-third or two-thirds of the angle between the first and the second frame of the set. If this is the case, the sequence will repeat itself after three full rotations, and the frames of the fourth rotation will be at the same angular position as those of the first rotation. The candidate rotation speeds usually will not meet the above requirement but can be corrected to approximate it. With a given number of merged rotations

$N_{Rotation}$, which is limited by the duration of the recording, we can calculate the number of frames per rotation of the preferred rotation speed $N'_{F/R}$ from the number of frames per rotation of the candidate rotation speed $N_{F/R}$ as follows:

$$N'_{F/R} = [N_{F/R}] \pm \frac{m}{N_{Rotation}}, \quad N_{F/R} = \frac{f_{Frame}}{f_{Candidate}}, \quad m \in \{1, 2, 3, \cdots\}, \quad m < N_{Rotation} \tag{A.2}$$

To avoid that the frame sequence will repeat itself before the number of rotations to merge m has to agree to the following additional requirement when $N_{Rotation}$ is larger than 1:

$$i\, m = j\, N_{Rotation}, \quad i, j \in \{1, 2, 3, \cdots\}, \quad i < N_{Rotation} \tag{A.3}$$

By selecting the preferred number of frames per rotation that deviates the least from the number of frames per rotation of the candidate rotation speed, we then can calculate the rotation speed:

$$f_{Rotation} = f_{Candidate} \left(1 - \frac{\left(N'_{F/R} - N_{F/R}\right) N_{Rotation}}{\left(\left(\left\lceil \frac{N_{F/R} N_{Rotation}}{N_{F/S}} \right\rceil - 1 \right) n + N_{Rotation} \right) N_{F/R}} \right) \tag{A.4}$$

With this solution, it is assured that the frames of the first and the last segments used will assume their ideal angular position. By using the rotation speed resulting from the candidate needing the smallest correction, the frames from intermediate segments only will deviate minimally from their ideal position (see table 3.1).

Bibliography

Aakhus, S., J. Maehle and K. Bjoernstad. A new method for echocardiographic computerized three-dimensional reconstruction of left ventricular endocardial surface: in vitro accuracy and clinical repeatability of volumes. *J Am Soc Echocardiogr*, 7(6):571–81, 1994. 110

Aanonsen, S. I., T. Barkve, J. N. Tjotta and S. Tjotta. Distortion and harmonic generation in the nearfield of a finite amplitude sound beam. *J Acoust Soc Am*, 75(3):749–768, 1984. 13

Abraham, W. T. Cardiac resynchronization therapy for heart failure: biventricular pacing and beyond. *Curr Opin Cardiol*, 17(4):346–52, 2002a. 141, 149

Abraham, W. T. Rationale and design of a randomized clinical trial to assess the safety and efficacy of cardiac resynchronization therapy in patients with advanced heart failure: the multicenter insync randomized clinical evaluation (miracle). *J Card Fail*, 6(4):369–80, 2000. 149

Abraham, W. T., W. G. Fisher, A. L. Smith, D. B. Delurgio, A. R. Leon, E. Loh, D. Z. Kocovic, M. Packer, A. L. Clavell, D. L. Hayes, M. Ellestad, R. J. Trupp, J. Underwood, F. Pickering, C. Truex, P. McAtee and J. Messenger. Cardiac resynchronization in chronic heart failure. *N Engl J Med*, 346(24):1845–53, 2002b. 141

Altmann, K., Z. Shen, L. M. Boxt, D. L. King, W. M. Gersony, L. D. Allan and H. D. Apfel. Comparison of three-dimensional echocardiographic assessment of volume, mass, and function in children with functionally single left ventricles with two-dimensional echocardiography and magnetic resonance imaging. *Am J Cardiol*, 80(8):1060–5, 1997. 92

Ames, W. F. *Numerical methods for partial differential equations*. Computer science and scientific computing. Academic Press, Boston, 3rd edition, 1992. 17

Angelini, E. D., A. F. Laine, S. Takuma, J. W. Holmes and S. Homma. Lv

volume quantification via spatiotemporal analysis of real-time 3-d echocardiography. *IEEE Trans Med Imaging*, 20(6):457–69, 2001. 83

Ansalone, G., P. Giannantoni, R. Ricci, P. Trambaiolo, F. Fedele and M. Santini. Doppler myocardial imaging to evaluate the effectiveness of pacing sites in patients receiving biventricular pacing. *J Am Coll Cardiol*, 39(3):489–99, 2002. 141, 149

Arai, K., T. Hozumi, Y. Matsumura, K. Sugioka, Y. Takemoto, H. Yamagishi, M. Yoshiyama, H. Kasanuki and J. Yoshikawa. Accuracy of measurement of left ventricular volume and ejection fraction by new real-time three-dimensional echocardiography in patients with wall motion abnormalities secondary to myocardial infarction. *Am J Cardiol*, 94(5):552–8, 2004. 65

Aronson, S. Measurement of myocardial perfusion by contrast echocardiography: application in the operating room. *Coron Artery Dis*, 11(3):227–34, 2000. 129

Averkiou, M. A. and M. F. Hamilton. Measurements of harmonic generation in a focused finite-amplitude sound beam. *J Acoust Soc Am*, 98(6):3439–42, 1995. 13

Averkiou, M. A. and M. F. Hamilton. Nonlinear distortion of short pulses radiated by plane and focused circular pistons. *J Acoust Soc Am*, 102(5 Pt 1): 2539–48, 1997. 13

Baker, A. C., A. M. Berg, A. Sahin and J. N. Tjotta. The nonlinear pressure field of plane, rectangular apertures - experimental and theoretical results. *J Acoust Soc Am*, 97(6):3510–3517, 1995. 13, 24, 29, 42

Baker, A. C., K. Anastasiadis and V. F. Humphrey. The nonlinear pressure field of a plane circular piston: Theory and experiment. *J Acoust Soc Am*, 84 (4):1483–1487, 1988. 13

Barberato, S. H., D. E. Mantilla, M. A. Misocami, S. M. Goncalves, A. T. Bignelli, M. C. Riella and R. Pecoits-Filho. Effect of preload reduction by hemodialysis on left atrial volume and echocardiographic doppler parameters in patients with end-stage renal disease. *Am J Cardiol*, 94(9):1208–10, 2004. 124

Barnett, S. B., G. R. Ter Haar, M. C. Ziskin, H. D. Rott, F. A. Duck and K. Maeda. International recommendations and guidelines for the safe use of diagnostic ultrasound in medicine. *Ultrasound Med Biol*, 26(3):355–366, 2000. 3

Bax, J. J., S. G. Molhoek, L. van Erven, P. J. Voogd, S. Somer, E. Boersma, P. Steendijk, M. J. Schalij and E. E. van der Wall. Usefulness of myocardial tissue doppler echocardiography to evaluate left ventricular dyssynchrony before and after biventricular pacing in patients with idiopathic dilated car-

diomyopathy. *Am J Cardiol*, 91(1):94–7, 2003. 141, 149

Belohlavek, M., D. A. Foley, T. C. Gerber, T. M. Kinter, J. F. Greenleaf and J. B. Seward. Three- and four-dimensional cardiovascular ultrasound imaging: a new era for echocardiography. *Mayo Clin Proc*, 68(3):221–40, 1993. 99

Belohlavek, M., K. Tanabe, D. Jakrapanichakul, J. F. Breen and J. B. Seward. Rapid three-dimensional echocardiography : clinically feasible alternative for precise and accurate measurement of left ventricular volumes. *Circulation*, 103 (24):2882–4, 2001. 7, 71, 72

Berntsen, J., J. N. Tjotta and S. Tjotta. Nearfield of a large acoustic transducer. part iv: Second harmonic and sum frequency radiation. *J Acoust Soc Am*, 75 (5):1383–1391, 1984. 13

Bland, J. M. and D. G. Altman. Statistical methods for assessing agreement between two methods of clinical measurement. *Lancet*, 1(8476):307–10, 1986. 75, 92, 104, 121

Bornstein, A., W. H. Gaasch and J. Harrington. Assessment of the cardiac effects of hemodialysis with systolic time intervals and echocardiography. *Am J Cardiol*, 51(2):332–5, 1983. 117

Bosch, J. G., G. van Burken, F. Nijland and J. H. C. Reiber. Overview of automated quantitation techniques in 2d echocardiography. In **Reiber, J. H. C.** and E. van der Wall, editors, *What's new in cardiovascular imaging?*, Developments in cardiovascular medicine, pages 363–376, 1998. 87

Bosch, J. G., S. C. Mitchell, B. P. Lelieveldt, F. Nijland, O. Kamp, M. Sonka and J. H. Reiber. Automatic segmentation of echocardiographic sequences by active appearance motion models. *IEEE Trans Med Imaging*, 21(11):1374–83, 2002. 99

Bouakaz, A., S. Frigstad, F. J. Ten Cate and N. de Jong. Super harmonic imaging: a new imaging technique for improved contrast detection. *Ultrasound Med Biol*, 28(1):59–68, 2002. 129

Bouakaz, A., B. J. Krenning, W. B. Vletter, F. J. ten Cate and N. de Jong. Contrast superharmonic imaging: a feasibility study. *Ultrasound Med Biol*, 29 (4):547–53, 2003a. 65, 80

Bouakaz, A., C. T. Lancée and N. de Jong. Harmonic ultrasonic field of medical phased arrays: simulations and measurements. *IEEE Trans Ultrason Ferroelectr Freq Control*, 50(6):730–5, 2003b. 13, 47

Bouakaz, A., F. Cate and N. de Jong. A new ultrasonic transducer for improved contrast nonlinear imaging. *Phys Med Biol*, 49(16):3515–25, 2004. 137

Buck, T., P. Hunold, K. U. Wentz, W. Tkalec, H. J. Nesser and R. Erbel. Tomo-

graphic three-dimensional echocardiographic determination of chamber size and systolic function in patients with left ventricular aneurysm: comparison to magnetic resonance imaging, cineventriculography, and two-dimensional echocardiography. *Circulation*, 96(12):4286–97, 1997. 92, 109

Cahill, M. D. and A. C. Baker. Numerical simulation of the acoustic field of a phased-array medical ultrasound scanner. *J Acoust Soc Am*, 104(3):1274–1283, 1998. 13, 46

Canals, R., G. Lamarque and P. Chatain. Volumetric ultrasound system for left ventricle motion imaging. *IEEE Trans Ultrason Ferroelectr Freq Control*, 46 (6):1527–1538, 1999. 7, 63

Carnahan, B., H. A. Luther and J. O. Wilkes. *Applied numerical methods*. Wiley, New York, 1969. 18, 19

Cazeau, S., C. Leclercq, T. Lavergne, S. Walker, C. Varma, C. Linde, S. Garrigue, L. Kappenberger, G. A. Haywood, M. Santini, C. Bailleul and J. C. Daubert. Effects of multisite biventricular pacing in patients with heart failure and intraventricular conduction delay. *N Engl J Med*, 344(12):873–80, 2001. 141

Chaignon, M., W. T. Chen, R. C. Tarazi, S. Nakamoto and E. Salcedo. Acute effects of hemodialysis on echographic-determined cardiac performance: improved contractility resulting from serum increased calcium with reduced potassium despite hypovolemic-reduced cardiac output. *Am Heart J*, 103(3): 374–8, 1982. 117

Chan, K. L., X. Liu, K. J. Ascah, L. M. Beauchesne and I. G. Burwash. Comparison of real-time 3-dimensional echocardiography with conventional 2-dimensional echocardiography in the assessment of structural heart disease. *J Am Soc Echocardiogr*, 17(9):976–80, 2004. 65

Christopher, P. T. and K. J. Parker. New approaches to nonlinear diffractive field propagation. *J Acoust Soc Am*, 90(1):488–499, 1991. 13, 14

Christopher, T. Algorithm for the nonlinear propagation of acoustic beams from phased arrays and nonplanar sources. *IEEE Trans Ultrason Ferroelectr Freq Control*, 53(11):2188–2192, 2006. 14, 47

Cohen, M. V., P. Diaz and J. Scheuer. Echocardiographic assessment of left ventricular function in patients with chronic uremia. *Clin Nephrol*, 12(4):156–62, 1979. 117

Corsi, C., G. Saracino, A. Sarti and C. Lamberti. Left ventricular volume estimation for real-time three-dimensional echocardiography. *IEEE Trans Med Imaging*, 21(9):1202–8, 2002. 83

Corsi, C., R. M. Lang, F. Veronesi, L. Weinert, E. G. Caiani, P. MacEneaney,

C. Lamberti and V. Mor-Avi. Volumetric quantification of global and regional left ventricular function from real-time three-dimensional echocardiographic images. *Circulation*, 112(8):1161–70, 2005. 124

Danias, P. G., M. L. Chuang, R. A. Parker, R. A. Beaudin, M. G. Mooney, W. J. Manning, P. S. Douglas and M. G. Hibberd. Relation between the number of image planes and the accuracy of three-dimensional echocardiography for measuring left ventricular volumes and ejection fraction. *Am J Cardiol*, 82(11): 1431–4, A9, 1998. 109

Daubert, J. C., P. Ritter, H. Le Breton, D. Gras, C. Leclercq, A. Lazarus, J. Mugica, P. Mabo and S. Cazeau. Permanent left ventricular pacing with transvenous leads inserted into the coronary veins. *Pacing Clin Electrophysiol*, 21(1 Pt 2):239–45, 1998. 141

De Jong, N., R. Cornet and C. T. Lancée. Higher harmonics of vibrating gas-filled microspheres. part one: simulations. *Ultrasonics*, 32(6):447–453, 1994a. 129

De Jong, N., R. Cornet and C. T. Lancée. Higher harmonics of vibrating gas-filled microspheres. part two: measurements. *Ultrasonics*, 32(6):455–459, 1994b. 129

Delabays, A., N. G. Pandian, Q. L. Cao, L. Sugeng, G. Marx, A. Ludomirski and S. L. Schwartz. Transthoracic real-time three-dimensional echocardiography using a fan-like scanning approach for data acquisition: methods, strengths, problems, and initial clinical experience. *Echocardiography*, 12(1): 49–59, 1995. 6, 51

Djoa, K. K., N. de Jong, F. C. van Egmond, J. D. Kasprzak, W. B. Vletter, C. T. Lancée, A. F. van der Steen, N. Bom and J. R. Roelandt. A fast rotating scanning unit for real-time three-dimensional echo data acquisition. *Ultrasound Med Biol*, 26(5):863–9, 2000. 52, 72, 84, 99, 142

Duck, F. A. Nonlinear acoustics in diagnostic ultrasound. *Ultrasound Med Biol*, 28(1):1–18, 2002. 4, 14, 42

Duck, F. A. *Physical properties of tissue : a comprehensive reference book*. Academic Press, London, San Diego, 1990. 22, 37

Engelse, W. and C. Zeelenberg. A single scan algoritm for qrs-detection and feature extraction. *Comput Cardiol*, 6:37–42, 1979. 85

Fathi, R., N. Isbel, B. Haluska, C. Case, D. W. Johnson and T. H. Marwick. Correlates of subclinical left ventricular dysfunction in esrd. *Am J Kidney Dis*, 41(5):1016–25, 2003. 125

Forsberg, F., N. M. Rawool, D. A. Merton, J. B. Liu and B. B. Goldberg. Contrast

enhanced vascular three-dimensional ultrasound imaging. *Ultrasonics*, 40(1-8):117–22, 2002. 135

Frinking, P. J., A. Bouakaz, J. Kirkhorn, F. J. Ten Cate and N. de Jong. Ultrasound contrast imaging: current and new potential methods. *Ultrasound Med Biol*, 26(6):965–75, 2000. 14

Froysa, K. E. and F. Coulouvrat. A renormalization method for nonlinear pulsed sound beams. *J Acoust Soc Am*, 99(6):3319–3328, 1996. 13

Froysa, K. E., J. N. Tjotta and S. Tjotta. Linear propagation of a pulsed sound beam from a plane or focusing source. *J Acoust Soc Am*, 93(1):80–92, 1993. 28

Galetta, F., A. Cupisti, F. Franzoni, A. Carpi, G. Barsotti and G. Santoro. Acute effects of hemodialysis on left ventricular function evaluated by tissue doppler imaging. *Biomed Pharmacother*, 60(2):66–70, 2006. 117

Garrett, G. S., J. N. Tjotta and S. Tjotta. Nearfield of a large acoustic transducer, part i. linear radiation. *J Acoust Soc Am*, 72(3):1056–1061, 1982. 28, 29

Germano, G., J. Erel, H. Lewin, P. B. Kavanagh and D. S. Berman. Automatic quantitation of regional myocardial wall motion and thickening from gated technetium-99m sestamibi myocardial perfusion single-photon emission computed tomography. *J Am Coll Cardiol*, 30(5):1360–7, 1997. 149

Goldberg, B. B., J. S. Raichlen and F. Forsberg. *Ultrasound contrast agents : basic principles and clinical applications*. Martin Dunitz, London, 2nd edition, 2001. 129

Gopal, A. S., D. L. King, J. Katz, L. M. Boxt, J. King, D. L. and M. Y. Shao. Three-dimensional echocardiographic volume computation by polyhedral surface reconstruction: in vitro validation and comparison to magnetic resonance imaging. *J Am Soc Echocardiogr*, 5(2):115–24, 1992. 5, 104

Gras, D., P. Mabo, T. Tang, O. Luttikuis, R. Chatoor, A. K. Pedersen, H. H. Tscheliessnigg, J. C. Deharo, A. Puglisi, J. Silvestre, S. Kimber, H. Ross, A. Ravazzi, V. Paul and D. Skehan. Multisite pacing as a supplemental treatment of congestive heart failure: preliminary results of the medtronic inc. insync study. *Pacing Clin Electrophysiol*, 21(11 Pt 2):2249–55, 1998. 141

Grines, C. L., T. M. Bashore, H. Boudoulas, S. Olson, P. Shafer and C. F. Wooley. Functional abnormalities in isolated left bundle branch block. the effect of interventricular asynchrony. *Circulation*, 79(4):845–53, 1989. 141

Gupta, S., V. Dev, M. V. Kumar and S. C. Dash. Left ventricular diastolic function in end-stage renal disease and the impact of hemodialysis. *Am J Cardiol*, 71(16):1427–30, 1993. 117

Gutierrez-Chico, J. L., J. L. Zamorano, L. Perez de Isla, M. Orejas, C. Alme-

ria, J. L. Rodrigo, J. Ferreiros, V. Serra and C. Macaya. Comparison of left ventricular volumes and ejection fractions measured by three-dimensional echocardiography versus by two-dimensional echocardiography and cardiac magnetic resonance in patients with various cardiomyopathies. *Am J Cardiol*, 95(6):809–13, 2005. 124

Hall, N. A., W. Lee and L. Degertekin. Capacitive micromachined ultrasonic trransducers with diffraction-based integrated optical displacement detection. *IEEE Trans Ultrason Ferroelectr Freq Control*, 50(11):1570–1580, 2003. 160

Hall, S. A., C. G. Cigarroa, L. Marcoux, R. C. Risser, P. A. Grayburn and E. J. Eichhorn. Time course of improvement in left ventricular function, mass and geometry in patients with congestive heart failure treated with beta-adrenergic blockade. *J Am Coll Cardiol*, 25(5):1154–61, 1995. 71, 99

Hamilton, M. F., V. A. Khokhlova and O. V. Rudenko. Analytical method for describing the paraxial region of finite amplitude sound beams. *J Acoust Soc Am*, 101(3):1298–1308, 1997. 13

Hamilton, M. F. and D. T. Blackstock. *Nonlinear acoustics*. Academic Press, San Diego, 1998. 29, 129

Hamilton, M. F., J. N. Tjotta and S. Tjotta. Nonlinear effects in the farfield of a directive sound source. *J Acoust Soc Am*, 78(1):202–216, 1985. 13

Handschumacher, M. D., J. P. Lethor, S. C. Siu, D. Mele, J. M. Rivera, M. H. Picard, A. E. Weyman and R. A. Levine. A new integrated system for three-dimensional echocardiographic reconstruction: development and validation for ventricular volume with application in human subjects. *J Am Coll Cardiol*, 21(3):743–53, 1993. 5

Howry, D. H., G. Posakony, C. R. Cushman and J. H. Holmes. Three-dimensional and stereoscopic observation of body structures by ultrasound. *J Appl Physiol*, 9(2):304–306, 1956. 5

Humphrey, V. F. Nonlinear propagation in ultrasonic fields: measurements, modelling and harmonic imaging. *Ultrasonics*, 38(1-8):267–272, 2000. 4, 35

Ie, E. H. and R. Zietse. Evaluation of cardiac function in the dialysis patient–a primer for the non-expert. *Nephrol Dial Transplant*, 21(6):1474–81, 2006. 124

Ie, E. H., W. B. Vletter, F. J. ten Cate, R. W. Nette, W. Weimar, J. R. Roelandt and R. Zietse. Preload dependence of new doppler techniques limits their utility for left ventricular diastolic function assessment in hemodialysis patients. *J Am Soc Nephrol*, 14(7):1858–62, 2003. 117

Iwase, M., T. Kondo, K. Hasegawa, M. Kimura, H. Matsuyama, Y. Watanabe and H. Hishida. Three-dimensional echocardiography by semi-automatic

border detection in assessment of left ventricular volume and ejection fraction: comparison with magnetic resonance imaging. *J Cardiol*, 30(2):97–105, 1997. 92, 106

Jenkins, C., K. Bricknell, L. Hanekom and T. H. Marwick. Reproducibility and accuracy of echocardiographic measurements of left ventricular parameters using real-time three-dimensional echocardiography. *J Am Coll Cardiol*, 44(4): 878–86, 2004. 95, 124

Jensen, J. A. and N. B. Svendsen. Calculation of pressure fields from arbitrarily shaped, apodized, and excited ultrasound transducers. *IEEE Trans Ultrason Ferroelectr Freq Control*, 39(2):262–267, 1992. 21, 22, 36

Kamakura, T., M. Tani, Y. Kumamoto and K. Ueda. Harmonic-generation in finite-amplitude sound beams from a rectangular aperture source. *J Acoust Soc Am*, 91(6):3144–3151, 1992. 29, 39

Kasprzak, J. D., B. Paelinck, F. J. Ten Cate, W. B. Vletter, N. de Jong, D. Poldermans, A. Elhendy, A. Bouakaz and J. R. Roelandt. Comparison of native and contrast-enhanced harmonic echocardiography for visualization of left ventricular endocardial border. *Am J Cardiol*, 83(2):211–7, 1999. 125, 135

Kerwin, W. F., E. H. Botvinick, J. W. O'Connell, S. H. Merrick, T. DeMarco, K. Chatterjee, K. Scheibly and L. A. Saxon. Ventricular contraction abnormalities in dilated cardiomyopathy: effect of biventricular pacing to correct interventricular dyssynchrony. *J Am Coll Cardiol*, 35(5):1221–7, 2000. 141

Khokhlova, V. A., A. E. Ponomarev, M. A. Averkiou and L. A. Crum. Nonlinear pulsed ultrasound beams radiated by rectangular focused diagnostic transducers. *Acoustical Physics*, 52(4):481–489, 2006. 30, 47

Kochanek, D. and R. H. Bartels. Interpolating splines with local tension, continuity, and bias control. *Computer Graphics (ACM)*, 18(3):33–41, 1984. 88

Krebs, W., H. G. Klues, S. Steinert, M. Sivarajan, F. P. Job, F. A. Flachskampf, A. Franke, T. Reineke and P. Hanrath. Left ventricular volume calculations using a multiplanar transoesophageal echoprobe; in vitro validation and comparison with biplane angiography. *Eur Heart J*, 17(8):1279–88, 1996. 110

Krenning, B. J., M. M. Voormolen and J. R. Roelandt. Assessment of left ventricular function by three-dimensional echocardiography. *Cardiovasc Ultrasound*, 1:12, 2003. 51, 79, 129

Krenning, B. J., M. M. Voormolen, R. J. van Geuns, W. B. Vletter, C. T. Lancée, N. de Jong, F. J. ten Cate, A. F. W. van der Steen and J. R. T. C. Roelandt. Rapid and accurate measurement of left ventricular function with a new second-harmonic fast-rotating transducer and semi-automated border detec-

tion. *Echocardiography*, accepted, 2006. 118, 119, 121, 124

Kuhl, H. P., A. Franke, M. Merx, R. Hoffmann, D. Puschmann and P. Hanrath. Rapid quantification of left ventricular function and mass using transoesophageal three-dimensional echocardiography: validation of a method that uses long-axis cutplanes. *Eur J Echocardiogr*, 1(3):213–21, 2000. 110

Kuhl, H. P., M. Schreckenberg, D. Rulands, M. Katoh, W. Schafer, G. Schummers, A. Bucker, P. Hanrath and A. Franke. High-resolution transthoracic real-time three-dimensional echocardiography: quantitation of cardiac volumes and function using semi-automatic border detection and comparison with cardiac magnetic resonance imaging. *J Am Coll Cardiol*, 43(11):2083–90, 2004. 71, 80, 106

Kuhlkamp, V. Initial experience with an implantable cardioverter-defibrillator incorporating cardiac resynchronization therapy. *J Am Coll Cardiol*, 39(5):790–7, 2002. 141

Kuhn, H., G. Beer and F. Gietzen. Definition and classification of cardiomyopathies. *Circulation*, 94(11):2991–2, 1996. 141

Kupferwasser, I., S. Mohr-Kahaly, P. Stahr, H. J. Rupprecht, U. Nixdorff, M. Fenster, T. Voigtlander, R. Erbel and J. Meyer. Transthoracic three-dimensional echocardiographic volumetry of distorted left ventricles using rotational scanning. *J Am Soc Echocardiogr*, 10(8):840–52, 1997. 72

Kuznetsov, V. Equations of nonlinear acoustics. *Sov Phys Acoust*, 16(4):467–70, 1971. 13

Lancée, C. T., F. C. van Egmond, N. de Jong, F. Mastik, A. F. W. van der Steen, J. R. T. C. Roelandt and N. Bom. Data processing for a fast rotating phased array real-time 3d acquisition unit. In *Proceedings - IEEE Ultrasonics Symposium*, volume 2, pages 1597–1600, 2000. 73, 143

Leclercq, C., S. Cazeau, H. Le Breton, P. Ritter, P. Mabo, D. Gras, D. Pavin, A. Lazarus and J. C. Daubert. Acute hemodynamic effects of biventricular ddd pacing in patients with end-stage heart failure. *J Am Coll Cardiol*, 32(7): 1825–31, 1998. 141

Leclercq, C., S. Cazeau, P. Ritter, C. Alonso, D. Gras, P. Mabo, A. Lazarus and J. C. Daubert. A pilot experience with permanent biventricular pacing to treat advanced heart failure. *Am Heart J*, 140(6):862–70, 2000. 141

Lee, D., A. R. Fuisz, P. H. Fan, T. L. Hsu, C. P. Liu and H. T. Chiang. Real-time 3-dimensional echocardiographic evaluation of left ventricular volume: correlation with magnetic resonance imaging–a validation study. *J Am Soc Echocardiogr*, 14(10):1001–9, 2001. 80

Lee, Y. S. *Numerical solution of the KZK equation for pulsed finite amplitude sound beams in thermoviscous fluids*. Ph.d. thesis, The University of Texas, 1993. 18

Lee, Y. S. and M. F. Hamilton. Time-domain modeling of pulsed finite-amplitude sound beams. *J Acoust Soc Am*, 97(2):906–917, 1995. 13, 14, 15, 17, 22

Li, Y. D. and J. A. Zagzebski. Computer model for harmonic ultrasound imaging. *IEEE Trans Ultrason Ferroelectr Freq Control*, 47(4):1000–1013, 2000. 14

Lozano, I., M. Bocchiardo, M. Achtelik, F. Gaita, H. J. Trappe, E. Daoud, J. Hummel, C. Duby and P. Yong. Impact of biventricular pacing on mortality in a randomized crossover study of patients with heart failure and ventricular arrhythmias. *Pacing Clin Electrophysiol*, 23(11 Pt 2):1711–2, 2000. 149

Lucas, B. G., J. N. Tjotta and T. G. Muir. Field of a parametric focusing source. *J Acoust Soc Am*, 73(6):1966–1971, 1983. 13

Malm, S., S. Frigstad, E. Sagberg, H. Larsson and T. Skjaerpe. Accurate and reproducible measurement of left ventricular volume and ejection fraction by contrast echocardiography: a comparison with magnetic resonance imaging. *J Am Coll Cardiol*, 44(5):1030–5, 2004. 125

Mannaerts, H. F., J. A. van der Heide, O. Kamp, T. Papavassiliu, J. T. Marcus, A. Beek, A. C. van Rossum, J. Twisk and C. A. Visser. Quantification of left ventricular volumes and ejection fraction using freehand transthoracic three-dimensional echocardiography: comparison with magnetic resonance imaging. *J Am Soc Echocardiogr*, 16(2):101–9, 2003. 79, 96, 106, 108

Marcus, J. T., J. P. A. Kuijer, R. M. Gotte, R. M. Heethaar and A. C. van Rossum. Left ventricular mass measured by magnetic resonance imaging: Effect of endocardial trabeculae on the observed wall thickness. *J Cardiovasc Magn Reson*, 2(1):301–302, 2000. 158

Mascioli, G., A. Curnis, L. Bontempi and L. Dei Cas. Biventricular pacing for patients with severe congestive heart failure: a single center experience. *Ital Heart J*, 3(10):598–602, 2002. 141, 149

McGowan, J. H. and J. G. Cleland. Reliability of reporting left ventricular systolic function by echocardiography: a systematic review of 3 methods. *Am Heart J*, 146(3):388–97, 2003. 80

Monaghan, M. J. Role of real time 3d echocardiography in evaluating the left ventricle. *Heart*, 92(1):131–6, 2006. 117

Montagnat, J. and H. Delingette. Space and time shape constrained deformable surfaces for 4d medical image segmentation. In *Proceedings Medical Image Computing and Computer Assisted Intervention (MICCAI)*, volume 1935 of

Lecture Notes in Computer Science, pages 196–205, 2000. 83

Moriyasu, F., R. Migihashi, T. Matsumura, Y. Toda and T. Chiba. Harmonic gray scale 3d contrast imaging of the liver. *Acad Radiol*, 9 Suppl 1:S228–30, 2002. 135

Nachef, S., D. Cathignol, J. N. Tjotta, A. M. Berg and S. Tjotta. Investigation of a high-intensity sound beam from a plane transducer - experimental and theoretical results. *J Acoust Soc Am*, 98(4):2303–2323, 1995. 46

Nguyen, L. D. and C. Leger. Four-dimensional reconstruction of the left ventricle using a fast rotating classical phased array scan head: preliminary results. *J Am Soc Echocardiogr*, 15(6):593–600, 2002. 63, 72

Nguyen, L. D., C. Leger, D. Debrun, F. Therain, J. Visser and E. Busemann Sokole. Validation of a volumic reconstruction in 4-d echocardiography and gated spect using a dynamic cardiac phantom. *Ultrasound Med Biol*, 29 (8):1151–60, 2003. 63

Nguyen, T. V., E. L. Bolson, M. Zeppa, R. W. Martin and F. H. Sheehan. Influence of echocardiographic scan plane location and number on the accuracy of three-dimensional left ventricular volume and shape determination. *Am J Cardiol*, 84(2):208–13, 1999. 110

Nixdorff, U., I. Feddersen, J. U. Voigt and F. A. Flachskampf. Three-dimensional echocardiography: rational mode of component images for left ventricular volume quantitation. *Cardiology*, 104(2):76–82, 2005. 110

Nosir, Y. F., P. M. Fioretti, W. B. Vletter, E. Boersma, A. Salustri, J. T. Postma, A. E. Reijs, F. J. Ten Cate and J. R. Roelandt. Accurate measurement of left ventricular ejection fraction by three-dimensional echocardiography. a comparison with radionuclide angiography. *Circulation*, 94(3):460–6, 1996. 71, 72

Nosir, Y. F., J. Stoker, J. D. Kasprzak, M. H. Lequin, A. Dall'Agata, F. J. Ten Cate and J. R. Roelandt. Paraplane analysis from precordial three-dimensional echocardiographic data sets for rapid and accurate quantification of left ventricular volume and function: a comparison with magnetic resonance imaging. *Am Heart J*, 137(1):134–43, 1999. 95

Nosir, Y. F., W. B. Vletter, J. D. Kasprzak, E. Boersma, M. H. Lequin, A. A. Elhendy, J. Yao, J. Stoker, F. J. Ten Cate and J. R. Roelandt. Optimal rotational interval for 3-dimensional echocardiography data acquisition for rapid and accurate measurement of left ventricular function. *J Am Soc Echocardiogr*, 13 (8):715–22, 2000. 79, 109, 125

Ota, T., J. Kisslo, O. T. von Ramm and J. Yoshikawa. Real-time, volumetric

echocardiography: usefulness of volumetric scanning for the assessment of cardiac volume and function. *J Cardiol*, 37 Suppl 1:93–101, 2001. 80

Pandian, N. G., J. Roelandt, N. C. Nanda, L. Sugeng, Q. L. Cao, J. Azevedo, S. L. Schwartz, M. A. Vannan, A. Ludomirski, G. Marx and et al. Dynamic three-dimensional echocardiography: methods and clinical potential. *Echocardiography*, 11(3):237–59, 1994. 6, 51, 99

Papavassiliou, D., N. R. Doelling, M. K. Bowman, H. Yeung, J. Rock, B. Klas, K. Chung and D. A. Fyfe. Initial experience with an internally rotating transthoracic three-dimensional echocardiographic probe and image acquisition on a conventional echocardiogram machine. *Echocardiography*, 15(4): 369–376, 1998. 51

Perez, J. E., A. D. Waggoner, B. Barzilai, J. Melton, H. E., J. G. Miller and B. E. Sobel. On-line assessment of ventricular function by automatic boundary detection and ultrasonic backscatter imaging. *J Am Coll Cardiol*, 19(2):313–20, 1992. 80

Pitzalis, M. V., M. Iacoviello, R. Romito, F. Massari, B. Rizzon, G. Luzzi, P. Guida, A. Andriani, F. Mastropasqua and P. Rizzon. Cardiac resynchronization therapy tailored by echocardiographic evaluation of ventricular asynchrony. *J Am Coll Cardiol*, 40(9):1615–22, 2002. 149

Qin, J. X., M. Jones, T. Shiota, N. L. Greenberg, H. Tsujino, M. S. Firstenberg, P. C. Gupta, A. D. Zetts, Y. Xu, J. Ping Sun, L. A. Cardon, J. A. Odabashian, S. D. Flamm, R. D. White, J. A. Panza and J. D. Thomas. Validation of real-time three-dimensional echocardiography for quantifying left ventricular volumes in the presence of a left ventricular aneurysm: in vitro and in vivo studies. *J Am Coll Cardiol*, 36(3):900–7, 2000. 80

Roelandt, J., A. Salustri, B. Mumm and W. Vletter. Precordial three-dimensional echocardiography with a rotational imaging probe: methods and initial clinical experience. *Echocardiography*, 12(3):243–52, 1995. 51

Roelandt, J. R. T. C. Three-dimensional echocardiography: the future today! *Comput Graph*, 24(5):715–729, 2000. 51, 99

Rusk, R. A., Y. Mori, C. H. Davies, T. Irvine, A. Kenny and D. J. Sahn. Comparison of ventricular volume and mass measurements from b- and c-scan images with the use of real-time 3-dimensional echocardiography: studies in an in vitro model. *J Am Soc Echocardiogr*, 13(10):910–7, 2000. 99

Saito, S., B. C. Kim and T. G. Muir. Second harmonic component of a nonlinearly distorted wave in a focused sound field. *J Acoust Soc Am*, 82(2):621–628, 1987. 13

Salustri, A. and J. R. Roelandt. Ultrasonic three-dimensional reconstruction of the heart. *Ultrasound Med Biol*, 21(3):281–93, 1995. 99, 129

Sanchez-Ortiz, G. I., J. Declerck, M. Mulet-Parada and J. A. Noble. Automating 3d echocardiographic image analysis. In *Proceedings Medical Image Computing and Computer Assisted Intervention (MICCAI)*, volume 1935 of *Lecture Notes in Computer Science*, pages 687–696, 2000. 83

Sanchez-Ortiz, G. I., G. J. Wright, N. Clarke, J. Declerck, A. P. Banning and J. A. Noble. Automated 3-d echocardiography analysis compared with manual delineations and spect muga. *IEEE Trans Med Imaging*, 21(9):1069–76, 2002. 99

Schiller, N. B., P. M. Shah, M. Crawford, A. DeMaria, R. Devereux, H. Feigenbaum, H. Gutgesell, N. Reichek, D. Sahn, I. Schnittger and et al. Recommendations for quantitation of the left ventricle by two-dimensional echocardiography. american society of echocardiography committee on standards, subcommittee on quantitation of two-dimensional echocardiograms. *J Am Soc Echocardiogr*, 2(5):358–67, 1989. 101, 119, 121

Schmidt, M. A., C. J. Ohazama, K. O. Agyeman, R. Z. Freidlin, M. Jones, J. M. Laurienzo, C. L. Brenneman, A. E. Arai, O. T. von Ramm and J. A. Panza. Real-time three-dimensional echocardiography for measurement of left ventricular volumes. *Am J Cardiol*, 84(12):1434–9, 1999. 80

Schnabel, R., A. V. Khaw, R. S. von Bardeleben, C. Strasser, T. Kramm, J. Meyer and S. Mohr-Kahaly. Assessment of the tricuspid valve morphology by transthoracic real-time-3d-echocardiography. *Echocardiography*, 22(1): 15–23, 2005. 65

Schreckenberg, M., G. von Dziembowski, O. Ziermann and D. Meyer-Ebrecht. Automatische objekterkennung in 3d echokardiographiesequenzen auf basis aktiver oberflachenmodellen und modellgekoppelter merkmalsextraktion. In **Lehmann, T.**, V. Metzler, K. Spitzer and T. Tolxdorff, editors, *Proceedings - Bildverarbeitung fur die Medizin*, Informatik aktuell, page V087, 1998. 83

Shamim, W., D. P. Francis, M. Yousufuddin, S. Varney, M. F. Pieopli, S. D. Anker and A. J. Coats. Intraventricular conduction delay: a prognostic marker in chronic heart failure. *Int J Cardiol*, 70(2):171–8, 1999. 141

Sharma, R., D. Pellerin, D. C. Gaze, R. L. Mehta, H. Gregson, C. P. Streather, P. O. Collinson and S. J. Brecker. Mitral peak doppler e-wave to peak mitral annulus velocity ratio is an accurate estimate of left ventricular filling pressure and predicts mortality in end-stage renal disease. *J Am Soc Echocardiogr*, 19(3): 266–73, 2006. 124

Sheikh, K., S. W. Smith, O. von Ramm and J. Kisslo. Real-time, three-dimensional echocardiography: feasibility and initial use. *Echocardiography*, 8 (1):119–25, 1991. 7, 51, 150

Shiota, T., P. M. McCarthy, R. D. White, J. X. Qin, N. L. Greenberg, S. D. Flamm, J. Wong and J. D. Thomas. Initial clinical experience of real-time three-dimensional echocardiography in patients with ischemic and idiopathic dilated cardiomyopathy. *Am J Cardiol*, 84(9):1068–73, 1999. 71

Siu, S. C., J. M. Rivera, J. L. Guerrero, M. D. Handschumacher, J. P. Lethor, A. E. Weyman, R. A. Levine and M. H. Picard. Three-dimensional echocardiography. in vivo validation for left ventricular volume and function. *Circulation*, 88(4 Pt 1):1715–23, 1993. 71

Siu, S. C., J. M. Rivera, M. D. Handschumacher, A. E. Weyman, R. A. Levine and M. H. Picard. Three-dimensional echocardiography: the influence of number of component images on accuracy of left ventricular volume quantitation. *J Am Soc Echocardiogr*, 9(2):147–55, 1996. 79, 110, 125

Sogaard, P., W. Y. Kim, H. K. Jensen, P. Mortensen, A. K. Pedersen, B. O. Kristensen and H. Egeblad. Impact of acute biventricular pacing on left ventricular performance and volumes in patients with severe heart failure. a tissue doppler and three-dimensional echocardiographic study. *Cardiology*, 95 (4):173–82, 2001. 149

Sogaard, P., H. Egeblad, W. Y. Kim, H. K. Jensen, A. K. Pedersen, B. O. Kristensen and P. T. Mortensen. Tissue doppler imaging predicts improved systolic performance and reversed left ventricular remodeling during long-term cardiac resynchronization therapy. *J Am Coll Cardiol*, 40(4):723–30, 2002. 141, 149

Soldo, S. J., S. L. Norris, J. R. Gober, L. J. Haywood, P. M. Colletti and M. Terk. Mri-derived ventricular volume curves for the assessment of left ventricular function. *Magn Reson Imaging*, 12(5):711–7, 1994. 141, 149

Sonka, M., V. Hlavac and R. Boyle. *Image processing, analysis, and machine vision*. PWS Pub., Pacific Grove, 2nd edition, 1999. 61, 90

Spencer, K. T., J. Bednarz, P. G. Rafter, C. Korcarz and R. M. Lang. Use of harmonic imaging without echocardiographic contrast to improve two-dimensional image quality. *Am J Cardiol*, 82(6):794–9, 1998. 4, 14, 35

Spicer, D. and T. H. Marwick. Three-dimensional echocardiography: research toy or clinical tool? *Heart Lung Circ*, 9(3):98–107, 2000. 99

Stepanishen, P. R. Transient radiation from pistons in an infinite planar baffle. *J Acoust Soc Am*, 49(5B):1629–1638, 1971. 22

Szabo, T. L. *Diagnostic ultrasound imaging : inside out*. Series in biomedical engineering. Elsevier Academic Press, Burlington, 2004. 42

Takemoto, Y., K. Tanabe, K. Chandrasekaran, K. V. Ballman, J. B. Seward and M. Belohlavek. Single-plane and biplane echocardiography: use of targeted scan planes improves the estimates of left ventricular volume and shape for analysis of postinfarction remodeling. *J Am Soc Echocardiogr*, 16(5):448–56, 2003. 101, 110

Tanabe, K., M. Belohlavek, D. Jakrapanichakul, R. Y. Bae, J. F. Greenleaf and J. B. Seward. Three-dimensional echocardiography: Precision and accuracy of left ventricular volume measurement using rotational geometry with variable numbers of slice resolution. *Echocardiography*, 15(6):575–580, 1998. 71, 79, 110, 125

Tavakkoli, J., D. Cathignol, R. Souchon and O. A. Sapozhnikov. Modeling of pulsed finite-amplitude focused sound beams in time domain. *J Acoust Soc Am*, 104(4):2061–2072, 1998. 30

Teupe, C., M. Takeuchi, S. P. Ram and N. G. Pandian. Three-dimensional echocardiography: in-vitro validation of a new, voxel-based method for rapid quantification of ventricular volume in normal and aneurysmal left ventricles. *Int J Cardiovasc Imaging*, 17(2):99–105, 2001. 110

Tjotta, J. N., J. A. Tencate and S. Tjotta. Effects of boundary-conditions on the nonlinear-interaction of sound beams. *J Acoust Soc Am*, 89(3):1037–1049, 1991. 28

Tjotta, J. N. and S. Tjotta. An analytical model for the nearfield of a baffled piston transducer. *J Acoust Soc Am*, 68(1):334–339, 1980. 27, 29

Tomson, C. R. Echocardiographic assessment of systolic function in dialysis patients. *Nephrol Dial Transplant*, 5(5):325–31, 1990. 117

Tranquart, F., N. Grenier, V. Eder and L. Pourcelot. Clinical use of ultrasound tissue harmonic imaging. *Ultrasound Med Biol*, 25(6):889–94, 1999. 4, 14, 35

Van Stralen, M., J. G. Bosch, M. M. Voormolen, G. van Burken, B. J. Krenning, C. T. Lancée, N. de Jong and J. H. C. Reiber. A semi-automatic endocardial border detection method for 4d ultrasound data. In *Proceedings Medical Image Computing and Computer Assisted Intervention (MICCAI)*, volume 3216 of *Lecture Notes in Computer Science*, pages 43–50, 2004. 86

Van Stralen, M., J. G. Bosch, M. M. Voormolen, G. van Burken, B. J. Krenning, R. J. van Geuns, C. T. Lancée, N. de Jong and J. H. Reiber. Left ventricular volume estimation in cardiac three-dimensional ultrasound: a semiautomatic border detection approach. *Acad Radiol*, 12(10):1241–9, 2005. 99

Von Bardeleben, R. S., H. P. Kuhl, S. Mohr-Kahaly and A. Franke. Second-generation real-time three-dimensional echocardiography. finally on its way into clinical cardiology? *Z Kardiol*, 93 Suppl 4:IV56–64, 2004. 51, 65, 99

Voormolen, M. M., A. Bouakaz, B. J. Krenning, C. T. Lancée, F. J. ten Cate and N. de Jong. Feasibility of 3d harmonic contrast imaging. *Ultrasonics*, 42(1-9): 739–43, 2004. 62

Voormolen, M. M., B. J. Krenning, C. T. Lancée, F. J. ten Cate, J. R. Roelandt, A. F. van der Steen and N. de Jong. Harmonic 3-d echocardiography with a fast-rotating ultrasound transducer. *IEEE Trans Ultrason Ferroelectr Freq Control*, 53(10):1739–48, 2006. 72, 73, 84, 99, 101, 118, 142

Ward, B., A. C. Baker and V. F. Humphrey. Nonlinear propagation applied to the improvement of resolution in diagnostic medical ultrasound. *J Acoust Soc Am*, 101(1):143–154, 1997. 4, 35

Weiss, J. L., L. W. Eaton, C. H. Kallman and W. L. Maughan. Accuracy of volume determination by two-dimensional echocardiography: defining requirements under controlled conditions in the ejecting canine left ventricle. *Circulation*, 67(4):889–95, 1983. 110

White, H. D., R. M. Norris, M. A. Brown, P. W. Brandt, R. M. Whitlock and C. J. Wild. Left ventricular end-systolic volume as the major determinant of survival after recovery from myocardial infarction. *Circulation*, 76(1):44–51, 1987. 71, 99

Xiao, H. B., C. H. Lee and D. G. Gibson. Effect of left bundle branch block on diastolic function in dilated cardiomyopathy. *Br Heart J*, 66(6):443–7, 1991. 141

Yang, X. M. and R. O. Clevelahd. Time domain simulation of nonlinear acoustic beams generated by rectangular pistons with application to harmonic imaging. *J Acoust Soc Am*, 117(1):113–123, 2005. 13, 30, 47

Yao, J., J. D. Kasprzak, Y. F. Nosir, R. Frowijn, W. B. Vletter and J. R. Roelandt. Appropriate 3-dimensional echocardiography data acquisition interval for left ventricular volume quantification: implications for clinical application. *J Am Soc Echocardiogr*, 12(12):1053–7, 1999. 110

Yu, E. H., C. E. Sloggett, R. M. Iwanochko, H. Rakowski and S. C. Siu. Feasibility and accuracy of left ventricular volumes and ejection fraction determination by fundamental, tissue harmonic, and intravenous contrast imaging in difficult-to-image patients. *J Am Soc Echocardiogr*, 13(3):216–24, 2000. 125

Yvorchuk, K. J., R. A. Davies and K. L. Chan. Measurement of left ventricular ejection fraction by acoustic quantification and comparison with radionuclide

angiography. *Am J Cardiol*, 74(10):1052–6, 1994. 80

Zabolotskaya, E. and R. Khokhlov. Quasi-plane waves in the nonlinear acoustics of confined beams. *Sov Phys Acoust*, 15(1):35–40, 1969. 13

Zagrodsky, V., V. Walimbe, C. R. Castro-Pareja, J. X. Qin, J. M. Song and R. Shekhar. Registration-assisted segmentation of real-time 3-d echocardiographic data using deformable models. *IEEE Trans Med Imaging*, 24(9):1089–99, 2005. 99

Zeidan, Z., R. Erbel, J. Barkhausen, P. Hunold, T. Bartel and T. Buck. Analysis of global systolic and diastolic left ventricular performance using volume-time curves by real-time three-dimensional echocardiography. *J Am Soc Echocardiogr*, 16(1):29–37, 2003. 141

Zemp, R. J., J. Tavakkoli and R. S. C. Cobbold. Modeling of nonlinear ultrasound propagation in tissue from array transducers. *J Acoust Soc Am*, 113(1): 139–152, 2003. 14, 22, 30, 47

Zoccali, C., F. A. Benedetto, F. Mallamaci, G. Tripepi, G. Giacone, A. Cataliotti, G. Seminara, B. Stancanelli and L. S. Malatino. Prognostic value of echocardiographic indicators of left ventricular systolic function in asymptomatic dialysis patients. *J Am Soc Nephrol*, 15(4):1029–37, 2004. 117

Samenvatting

Drie dimensionale (3D) echocardiografie heeft zich recentelijk, van experimentele techniek in de jaren '90, ontwikkeld tot een beeldvormingsmodaliteit voor de dagelijkse klinische praktijk. Het toepassen van nieuwe technieken die korte acquisitietijden (minder dan 10 seconden) mogelijk maken is daarbij cruciaal gebleken. Veruit de meeste commerciële 3D echosystemen voor de cardiologie maken gebruik van een zogenaamde *matrix transducer*. Bij dit type transducer wordt het uitgezonden ultrageluid volledig elektronische gestuurd. Voor twee dimensionale (2D) echocardiografie wordt gebruik gemaakt van zogenaamde *array transducers*. Bij dit type transducer wordt het uitgezonden ultrageluid slechts in één richting gestuurd. Binnen de 2D echocardiografie wordt vrijwel uitsluitend gebruik gemaakt van zogenaamde *harmonische beeldvorming*. Het getoonde beeld wordt bij deze techniek opgebouwd uit de eerste boventoon van de ontvangen echo's. Ten opzichte van conventionele (fundamentele) echografie heeft deze techniek een aantal unieke eigenschappen welke tot een hogere beeldresolutie en de onderdrukking van artefacten leiden. Dit proefschrift beschrijft de ontwikkeling, vervaardiging en klinische toepassing van een alternatieve 3D transducer: de *snel roterende ultrageluidstransducer*. Het concept combineert op een kosteneffectieve wijze de optimale harmonische eigenschappen van bestaande array transducers met de vereiste korte 3D acquisitietijd.

Het proefschrift bestaat uit drie delen. Allereerst wordt in hoofdstuk 1 een simulatiemethode beschreven waarmee de harmonische eigenschappen van medische transducers bestudeerd kunnen worden. Uniek voor de methode is de mogelijkheid om gestuurde ultrageluidsbundels te simuleren. De methode laat goede resultaten zien in een vergelijking met andere simulatiemethoden voor niet gestuurde ultrageluidsbundels. De experimentele validatie van de simulatiemethode volgt in hoofdstuk 2. Voor zowel gestuurde als niet gestuurde ultrageluidsbundels laat dit hoofdstuk goede resultaten in verge-

lijking met de metingen zien. Tevens toont hoofdstuk 2 de onderdrukking van zogenaamde *grating lobes* in harmonische beelden aan. Grating lobes resulteren in moeilijk te identificeren fantoom artefacten in echobeelden. Deel I wordt afgesloten met de beschrijving van de snel roterende ultrageluidstransducer in hoofdstuk 3.

Het kwantificeren van het linkerventrikel (LV) volume is één van de meest uitgevoerde metingen in het echolab en levert een belangrijke parameter voor klinische beslissingen. Deel II van het proefschrift beschrijft daarom het gebruik van de snel roterende transducer voor deze belangrijke toepassing. In hoofdstuk 4 wordt eerst aangetoond dat de transducer geschikt is voor het nauwkeurig meten van LV volumes. Hierbij wordt gebruik gemaakt van commerciële kwantificatiesoftware. Deze software is echter niet optimaal ingericht voor de opnamen van de snel roterende transducer. Daarom wordt in hoofdstuk 5 een zelf ontwikkelde en efficiëntere kwantificatie-applicatie gepresenteerd. Beide hoofdstukken laten een goede overeenkomst met LV volumes verkregen uit *magnetic resonance imaging* (MRI) opnamen zien.

Voor het kwantificeren van het LV wordt een beperkt aantal 2D beelden uit de 3D opname gebruikt. Het gebruiken van onnodig veel 2D beelden levert een inefficiënte kwantificatie op. Uit hoofdstuk 6 blijkt dat 8 zogenaamde *equiangulaire lange-as* beelden van het LV voldoende zijn voor een nauwkeurige meting van het volume. Wordt rekening gehouden met de radiale positie van deze lange-as beelden, dan kan zelfs volstaan worden met 4 beelden.

Meer geavanceerde klinische toepassingen van de snel roterende transducer worden beschreven in deel III. In hoofdstuk 7 wordt de flexibiliteit waarmee 3D echocardiografie kan worden toegepast gedemonstreerd. Aan het bed van de patiënt werden, voor deze studie, 3D opnamen gemaakt tijdens de dialysebehandeling. Uit dit hoofdstuk blijkt de verhoogde nauwkeurigheid waarmee het LV volume gemeten kan worden met 3D echocardiografie, in vergelijking met 2D technieken. 3D echocardioigrafie kan daarom gebruikt worden voor de optimalisatie van de dialysebehandeling en het onderzoek naar het effect van de dialysebehandeling op de functie van het hart.

De harmonische kwaliteiten van de snel roterende transducer maken hem uitermate geschikt voor 3D contrast echocardiografie. Bij deze techniek worden kleine gasbelletjes (±3 μm in diameter) in de bloedbaan gebracht. Deze *microbellen* lichten op in de echobeelden. In tegenstelling tot conventionele echobeelden, waarin weefsel wordt gevisualiseerd, wordt bij contrast beelden het bloed afgebeeld. Hoofdstuk 8 belicht de voordelen van harmonische 3D contrast echocardiografie ten opzichte van fundamentele 3D contrast echocardiografie. Tevens laat dit hoofdstuk de eerste klinische resultaten van de snel

roterende transducer voor deze echomodaliteit zien.

Dit proefschrift wordt afgesloten met een haalbaarheidsstudie naar het meten van LV wandbewegingen in hoofdstuk 9. Asynchrone contractie van het LV kan behandeld worden met het plaatsen van een pacemaker. Voor de mate waarin de pacemaker het LV weet te resynchroniseren is de juiste plaatsing van de electroden van groot belang. Hoofdstuk 9 toont aan dat 3D echocardiography, in combinatie met de juiste kwantificatiesoftware, van dienst kan zijn bij het optimaliseren van de plaatsing en de instelling van pacemakers.

Epiloog

Het warme welkom dat mij in Rotterdam ten deel viel was een verademing na het wantrouwen dat een recent afgestudeerd ingenieur vaak ten deel valt bij het bemachtigen en de aanvang van een nieuwe positie. Ik wil mijn beide promotoren, Ton van der Steen en Nico de Jong, hiervoor graag bedanken.

De niet geringe lijst van coauteurs en de diverse *acknowledgements* laten er geen misverstand over bestaan dat ik het werk gepresenteerd in dit proefschrift niet alleen heb kunnen verrichten. Ik hoop dan ook dat ik mijn directe collega's van de 23st, de 19de en de afdeling klinische echocardiografie, die mij vaak met raad en daad hebben bijgestaan, op dezelfde manier heb gediend.

Een aantal personen zijn mij echter op een opmerkelijk onbaatzuchtige wijze van dienst geweest in de afgelopen zes jaar. Allereerst wil ik in dit verband mijn mentor Charles Lancée noemen. De manier waarop jij mij de afgelopen jaren van wijze raad hebt voorzien kent geen andere typering.

Mijn *partner in crime* Boudewijn Krenning; het was een waar genoegen om met je samen te werken, je weet op onnavolgbare wijze satire en enthousiasme te combineren. Het hebben van een lotgenoot is buitengewoon waardevol gebleken, bedankt voor je vriendschap. Vooruitlopend wil ik hier ook alvast mijn andere paranimf Vassilis Sboros bedanken. We hebben het samen vrijwel nooit over werk, laten we dat zo houden.

Onmisbare praktisch ondersteuning heb ik in de afgelopen jaren uit een meer onverwachte hoek mogen ontvangen. Vanuit Noorwegen is Johan Kirkhorn vrijwel onafgebroken als vraagbaak beschikbaar geweest. Johan, de accuratesse en snelheid waarmee jij mijn soms oneindige stroom aan vragen hebt weten te beantwoorden is echt ongekend, bedankt daarvoor.

Hoewel de relatief lange tijd die mijn promotie in beslag heeft genomen een bewuste keuze is geweest, heeft dit geresulteerd in een onverwacht hoge prijs. Afgelopen jaar heb ik mijn vader, groots voorbeeld en drijfveer, moeten laten gaan. Het mag duidelijk zijn dat zijn afwezigheid tijdens de verdediging van

dit proefschrift geen makkelijk aanvaardbaar feit is. Dit proefschrift is hoe dan ook het sluitstuk van mijn opleiding, welke zich soms langs ongebruikelijke wegen heeft voortbewogen. De vrijheid waarin ik dit heb mogen doen is enkel en alleen te danken aan de onvoorwaardelijke steun van mijn beide ouders.

María Azucena, Victor en Isabel; ik ben in prachtig gezelschap waarmee ik, in meerdere opzichten, op weg kan gaan naar nieuwe bestemmingen.

Marco Marien Voormolen
Amsterdam, 26 september 2007

List of Publications

Peer-reviewed articles

M. M. Voormolen, N. de Jong and A. Bouakaz. Simulation of steered harmonic acoustic beams from medical transducers - Part I: Method and benchmark. *J Acoust Soc Am*, submitted, 2007.

M. M. Voormolen, G. M. Matte, N. de Jong and A. Bouakaz. Simulation of steered harmonic acoustic beams from medical transducers - Part II: Experimental validation. *J Acoust Soc Am*, submitted, 2007.

M. van Stralen, K. Y. E. Leung, **M. M. Voormolen**, N. de Jong, A. F. W. van der Steen, J. H. Reiber and J. G. Bosch. Time continuous detection of the left ventricular long axis and the mitral valve plane in three-dimensional echocardiography. *Ultrasound Med Biol*, in press, 2007.

B. J. Krenning, **M. M. Voormolen**, M. L. Geleijnse, A. F. van der Steen, F. J. ten Cate, E. H. Ie and J. R. Roelandt. Three-dimensional echocardiographic analysis of left ventricular function during hemodialysis. *Nephron Clin Pract*, 107(2):c43–c49, 2007.

M. M. Voormolen, B. J. Krenning, R. J. van Geuns, J. Borsboom, C. T. Lancée, F. J. ten Cate, J. R. T. C. Roelandt, A. F. W. van der Steen and N. de Jong. Efficient quantification of the left ventricular volume using 3-dimensional echocardiography: The minimal number of equiangular long-axis images for accurate quantification of the left ventricular volume. *J Am Soc Echocardiogr*, 20(4):373–380, 2007.

S. M. van der Meer, B. Dollet, **M. M. Voormolen**, C. T. Chin, A. Bouakaz, N. de Jong, M. Versluis and D. Lohse. Microbubble spectroscopy of ultrasound contrast agents. *J Acoust Soc Am*, 121(1):648–656, 2007.

K. Y. E. Leung, M. van Stralen, G. van Burken, **M. M. Voormolen**, A. Nemes, F. J. ten Cate, N. de Jong, A. F. W. van der Steen, J. H. C. Reiber and J. G. Bosch.

Sparse appearance model based registration of 3d ultrasound images. In *Proceedings Medical Image Computing and Computer Assisted Intervention (MICCAI)*, volume 4091 of *Lecture Notes in Computer Science*, pages 236–243, 2006.

A. E. van den Bosch, D. Robbers-Visser, B. J. Krenning, **M. M. Voormolen**, J. S. McGhie, W. A. Helbing, J. W. Roos-Hesselink, M. L. Simoons and F. J. Meijboom. Real-time transthoracic three-dimensional echocardiographic assessment of left ventricular volume and ejection fraction in congenital heart disease. *J Am Soc Echocardiogr*, 19(1):1–6, 2006.

B. J. Krenning, **M. M. Voormolen**, R. J. van Geuns, W. B. Vletter, C. T. Lancée, N. de Jong, F. J. ten Cate, A. F. W. van der Steen and J. R. T. C. Roelandt. Rapid and accurate measurement of left ventricular function with a new second-harmonic fast-rotating transducer and semi-automated border detection. *Echocardiography*, 23(6):447–454, 2006.

M. M. Voormolen, B. J. Krenning, C. T. Lancée, F. J. ten Cate, J. R. T. C. Roelandt, A. F. W. van der Steen and N. de Jong. Harmonie 3-d echocardiography with a fast-rotating ultrasound transducer. *IEEE Trans Ultrason Ferroelectr Freq Control*, 53(10):1739–1747, 2006.

M. van Stralen, J. G. Bosch, **M. M. Voormolen**, G. van Burken, B. J. Krenning, R. J. M. van Geuns, C. T. Lancée, N. de Jong and J. H. C. Reiber. Left ventricular volume estimation in cardiac three-dimensional ultrasound: A semiautomatic border detection approach. *Acad Radiol*, 12(10):1241–1249, 2005.

M. van Stralen, J. G. Bosch, **M. M. Voormolen**, G. van Burken, B. J. Krenning, C. T. Lancée, N. de Jong and J. H. C. Reiber. A semi-automatic endocardial border detection method for 4d ultrasound data. In *Proceedings Medical Image Computing and Computer Assisted Intervention (MICCAI)*, volume 3216 of *Lecture Notes in Computer Science*, pages 43–50, 2004.

B. J. Krenning, T. Szili-Torok, **M. M. Voormolen**, D. A. M. J. Theuns, L. J. Jordaens, C. T. Lancée, N. de Jong, A. F. W. van der Steen, F. J. ten Cate and J. R. T. C. Roelandt. Guiding and optimization of resynchronization therapy with dynamic three-dimensional echocardiography and segmental volumetime curves: A feasibility study. *Eur J Heart Fail*, 6(5):619–625, 2004.

M. M. Voormolen, A. Bouakaz, B. J. Krenning, C. T. Lancée, F. J. ten Cate and N. de Jong. Feasibility of 3d harmonic contrast imaging. *Ultrasonics*, 42(1-9):739–743, 2004.

B. J. Krenning, **M. M. Voormolen** and J. R. T. C. Roelandt. Assessment of left ventricular function by three-dimensional echocardiography. *Cardiovasc Ultrasound*, 1:12, 2003.

T. Szili-Torok, B. J. Krenning, **M. M. Voormolen** and J. R. T. C. Roelandt. Dynamic three-dimensional echocardiography combined with semi-automated border detection offers advantages for assessment of resynchronization therapy. *Cardiovasc Ultrasound*, 1:14, 2003.

M. M. Voormolen, M. Ladouceur, P. H. Veltink and T. Sinkjaer. Soleus stretch reflex inhibition in the early swing phase of gait using deep peroneal nerve stimulation in spastic stroke participants. *Neuromodulation*, 3(2):107–117, 2000.

Conference proceedings

J. G. Bosch, M. van Stralen, **M. M. Voormolen**, B. J. Krenning, C. T. Lancée, J. H. C. Reiber, A. F. W. van der Steen and N. de Jong. Novel spatiotemporal voxel interpolation with multibeat fusion for 3d echocardiography with irregular data distribution. In *Medical Imaging 2006: Ultrasonic Imaging and Signal Processing - Proceedings of SPIE*, volume 6147, pages 61470Q-11, 2006.

K. Y. E. Leung, M. van Stralen, **M. M. Voormolen**, G. van Burken, A. Nemes, F. J. ten Cate, M. L. Geleijnse, N. de Jong, A. F. W. van der Steen, J. H. C. Reiber and J. G. Bosch. Registration of 2d cardiac images to real-time 3d ultrasound volumes for 3d stress echocardiography. In *Medical Imaging 2006: Image Processing - Proceedings of SPIE*, volume 6144, pages 614418-12, 2006.

M. van Stralen, J. G. Bosch, **M. M. Voormolen**, G. van Burken, B. J. Krenning, R. J. M. van Geuns, E. Angelie, R. J. van der Geest, C. T. Lancée, N. de Jong and J. H. C. Reiber. Semi-automatic border detection method for left ventricular volume estimation in 4d ultrasound data. In *Medical Imaging 2005: Image Processing - Proceedings of SPIE*, volume 5747, pages 1457–1467, 2005.

J. G. Bosch, M. van Stralen, **M. M. Voormolen**, B. J. Krenning, C. T. Lancée, J. H. C. Reiber, A. F. W. van der Steen and N. de Jong. Improved spatiotemporal voxel space interpolation for 3d echocardiography with irregular sampling and multibeat fusion. In *Proceedings - IEEE Ultrasonics Symposium*, volume 2, pages 1232–1235, 2005.

M. van Stralen, **M. M. Voormolen**, G. van Burken, B. J. Krenning, R. J. M. van Geuns, E. Angelie, R. J. van der Geest, C. T. Lancée, N. de Jong, A. F. W. van der Steen, J. H. C. Reiber and J. G. Bosch. A novel dynamic programming based semi-automatic endocardial border detection method for 4d cardiac ultrasound. In *Proceedings - IEEE Ultrasonics Symposium*, volume 2, pages 1224–1227, 2005.

M. van Stralen, J. G. Bosch, **M. M. Voormolen**, G. van Burken, B. J. Krenning,

C. T. Lancée, N. de Jong and J. H. C. Reiber. A semi-automatic endocardial border detection method for the left ventricle in 4d ultrasound data sets. In *International Congress Series*, volume 1268, pages 1078–1083, 2004.

M. M. Voormolen, A. Bouakaz, B. J. Krenning, C. T. Lancée, A. E. van den Bosch,W. B. Vletter, F. J. ten Cate, A. F. W. van der Steen and N. de Jong. 3d contrast harmonic echocardiography. In *Proceedings - IEEE Ultrasonics Symposium*, volume 1, pages 114–117, 2004.

M. M. Voormolen, B. J. Krenning, C. T. Lancée, F. J. ten Cate, J. R. T. C. Roelandt, A. F. W. van der Steen and N. de Jong. Quantitative harmonic 3d echocardiography with a fast rotating ultrasound transducer. In *Proceedings - IEEE Ultrasonics Symposium*, volume 1, pages 122–125, 2003.

M. M. Voormolen, A. Bouakaz, B. J. Krenning, C. T. Lancée, F. J. ten Cate, J. R. T. C. Roelandt, A. F. W. van der Steen, and N. de Jong. A new transducer for 3d harmonic imaging. In *Proceedings - IEEE Ultrasonics Symposium*, volume 2, pages 1261–1264, 2002.

Abstracts (selection of)

M. M. Voormolen, B. J. Krenning, R. J. van Geuns, C. T. Lancée, F. J. ten Cate, J. R. T. C. Roelandt, A. F. W. van der Steen and N. de Jong. Efficient quantification of the left ventricular volume using 3d-echocardiography. *Eur J Echocardiogr*, 7-SI:134–134, 2006.

M. van Stralen, **M. M. Voormolen**, E. Angelie, B. J. Krenning, R. J. M. van Geuns, N. de Jong, J. H. C. Reiber, and J. G. Bosch. Evaluation of automated full cycle left ventricular volume estimation for real-time 3d echo against mri. *Eur J Echocardiogr*, 6-SI:131–131, 2005.

M. van Stralen, J. G. Bosch, **M. M. Voormolen**, G. van Burken, B. J. Krenning, R. J. M. van Geuns, C. T. Lancée, N. de Jong, and J. H. C. Reiber. Semi-automatic left ventricular endocardial border detection method for 4d ultrasound data. *Eur J Echocardiogr*, 5-SI:57–57, 2004.

B. J. Krenning, **M. M. Voormolen**, R. J. van Geuns, W. B. Vletter, N. de Jong, C. T. Lancée, and F. J. ten Cate. Rapid and accurate measurement of left-ventricular function with a new second-harmonic fast-rotating transducer and semi-automated border detection. *Eur Heart J* 24-S:375–375, 2003.

T. Szili-Torok, B. J. Krenning, **M. M. Voormolen**, D. Theuns, L. J. Jordaens, F. ten Cate, and J. Roelandt. Assessment of resynchronisation therapy based on

dynamic three-dimensional echocardiography and semi-automated border detection. *Eur Heart J*, 24-S:395–395, 2003.

T. Szili-Torok, B. J. Krenning, **M. M. Voormolen**, C. T. Lancée, W. B. Vletter, M. F. Scholten, N. de Jong, A. F. W. van der Steen, L. J. Jordaens, and F. J. ten Cate. A novel method to assess and to guide cardiac resynchronization therapy: Four-dimensional echocardiography based on semi-automated contour detection. *Circulation* 106-SII:431–431, 2002.

About the Author

Marco M. Voormolen was born February 10th, 1972 in Utrecht, the Netherlands. He started his technical education in 1984 at the Chr. LTS in Gorinchem. In 1988 he continued his education in Utrecht. First at the Chr. MTS Scutos and in 1992 at the Hogeschool Utrecht. In 1994 he decided to interrupt his studies at the Hogeschool Utrecht to pursue his M.Sc. degree at the University of Twente in Enschede.

He earned his M.Sc. degree in Measurement & Control Engineering and Biomedical Engineering in 1998. The work for his thesis was carried out at the Center for Sensory-Motor Interaction, Aalborg University, Denmark. The project involved the restoration of the normal Soleus stretch reflex during gait in hemiplegic patients using conditioning transcutaneous electrical nerve stimulation.

From 1999 he worked as a consultant on Safety & Control Systems for the railway industry. From 2001 he was detached by the Interuniversity Cardiology Institute of The Netherlands (institute of the Royal Netherlands Academy of Arts and Sciences) at the Erasmus MC in Rotterdam, where he joined the Department of Biomedical Engineering of the Thoraxcenter to pursue his Ph.D. degree. His research concentrates on non-linear acoustic theory, 3D echocardiographic imaging techniques and image processing.

Marco M. Voormolen lives in Amsterdam with his wife María Azucena Gutiérrez González, his son Victor Voormolen Gutiérrez and daughter Isabel Voormolen Gutiérrez.

ISBN 978-90-8559-163-4